

General Disclaimer

One or more of the Following Statements may affect this Document

- This document has been reproduced from the best copy furnished by the organizational source. It is being released in the interest of making available as much information as possible.
- This document may contain data, which exceeds the sheet parameters. It was furnished in this condition by the organizational source and is the best copy available.
- This document may contain tone-on-tone or color graphs, charts and/or pictures, which have been reproduced in black and white.
- This document is paginated as submitted by the original source.
- Portions of this document are not fully legible due to the historical nature of some of the material. However, it is the best reproduction available from the original submission.

SOT
NASA CR-167926
BAT Report #D2536-941009

NASTRAN FLUTTER ANALYSIS

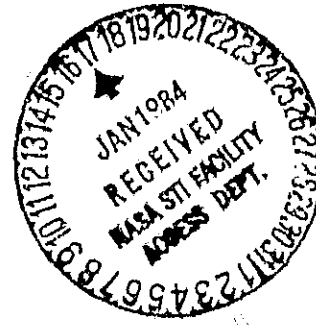
OF

ADVANCED TURBOPROPPELLERS

by

V. Elchuri
G. C. C. Smith

BELL AEROSPACE TEXTRON
P. O. Box One
Buffalo, New York 14240



(NASA-CR-167926) NASTRAN FLUTTER ANALYSIS
OF ADVANCED TURBOPROPPELLERS Final Report
(Textron Bell Aerospace Co., Buffalo, N.Y.)
121 p HC A06/MF A01

CSCL 02A

884-14148

Unclassified
G3/07 42638

National Aeronautics and Space Administration
Contract NAS3-22533

NASA Lewis Research Center
Cleveland, Ohio 44135

April 1982



1. Report No. NASA CR-167926	2. Government Accession No.	3. Recipient's Catalog No.	
4. Title and Subtitle NASTRAN FLUTTER ANALYSIS OF ADVANCED TURBOPROPPELLERS (U)		5. Report Date April 1982	
		6. Performing Organization Code	
7. Author(s) V. Elchuri and G. C. C. Smith		8. Performing Organization Report No. 02536-941009	
		10. Work Unit No.	
9. Performing Organization Name and Address Bell Aerospace Textron P. O. Box One Buffalo, New York 14240		11. Contract or Grant No. NAS 3-22533	
		13. Type of Report and Period Covered Contractor Report	
12. Sponsoring Agency Name and Address National Aeronautics and Space Administration Washington, D. C. 20546		14. Sponsoring Agency Code	
15. Supplementary Notes NASA Program Manager - Richard E. Morris, Final Report			
16. Abstract <p>An existing capability developed by the authors to conduct modal flutter analysis of tuned bladed-shrouded discs in NASTRAN has been modified and applied to investigate the subsonic unstalled flutter characteristics of advanced turbopropellers.</p> <p>The modifications pertain to the inclusion of oscillatory modal aerodynamic loads of blades with large (backward and forward) variable sweep. The two-dimensional subsonic cascade unsteady aerodynamic theory of W. P. Jones and B. M. Rao has been applied in a strip theory manner with appropriate modifications for the sweep effects. Each strip is associated with a chord selected normal to any spanwise reference curve such as the blade leading edge.</p> <p>The stability of three operating conditions of a 10-bladed propeller is analyzed. Each of these operating conditions is iterated once to determine the flutter boundary. A 5-bladed propeller is also analyzed at one operating condition to investigate stability. Analytical results obtained are in very good agreement with those from wind tunnel tests.</p> <p>The work was conducted under Contract NAS 3-2253C from NASA Lewis Research Center, Cleveland, Ohio, with Mr. Richard E. Morris as the Technical Monitor.</p>			
17. Key Words (Suggested by Author(s)) Advanced Turbopropellers, NASTRAN, Flutter Analysis, Finite Elements		18. Distribution Statement Unlimited - Unclassified Subject Categories: 07,61	
19. Security Classif. (of this report) Unclassified - Unlimited	20. Security Classif. (of this page) Unclassified - Unlimited	21. No. of Pages 112	22. Price*

* For sale by the National Technical Information Service, Springfield, Virginia 22161

NASA CR-167926
BAT Report #D2536-941009

NASTRAN FLUTTER ANALYSIS
OF
ADVANCED TURBOPROPPELLERS

by

V. Elchuri
G. C. C. Smith

BELL AEROSPACE TEXTRON
P. O. Box One
Buffalo, New York 14240

National Aeronautics and Space Administration
Contract NAS3-22533

NASA Lewis Research Center
Cleveland, Ohio 44135

April 1982

ABSTRACT

An existing capability developed by the authors to conduct modal flutter analysis of tuned bladed-shrouded discs in NASTRAN has been modified and applied to investigate the subsonic unstalled flutter characteristics of advanced turbopropellers.

The modifications pertain to the inclusion of oscillatory modal aerodynamic loads of multi-bladed propellers with large (backward and forward) variable sweep. Kaza and Kielb of NASA Lewis have demonstrated the aerodynamic significance of cascade and sweep effects on simplified structural models. In the current work, the two-dimensional subsonic cascade unsteady aerodynamic theory of W. P. Jones and B. M. Rao has been applied in a strip theory manner with appropriate modifications for the sweep effects. Each strip is associated with a chord selected normal to any spanwise reference curve such as the blade leading edge.

The stability of three operating conditions of a 10-bladed propeller is analyzed. Each of these operating conditions is iterated once to determine the flutter boundary. A 5-bladed propeller is also analyzed at one operating condition to investigate stability. Analytical results obtained are in very good agreement with those from wind tunnel tests.

The work was conducted under Contract NAS3-22533 from NASA Lewis Research Center, Cleveland, Ohio, with Mr. Richard E. Morris as the Technical Monitor.

SUMMARY

Generalized aerodynamic forces for varying sweep turbopropeller blades have been developed based on subsonic two-dimensional cascade theory. A bladed-disc dynamics/flutter program has been modified to enable the study of advanced turbopropeller flutter. Specific analyses show excellent agreement with wind tunnel results.

ACKNOWLEDGEMENT

The authors take this opportunity to express their deep appreciation of the programming efforts of Messrs. A. Michael Gallo and Steven C. Skalski, and Ms. Beverly J. Dale in implementing this theoretical development in NASTRAN. Technical discussions with Mr. R. E. Morris, Drs. K. R. V. Kaza and R. E. Kielb of NASA Lewis Research Center, and Dr. J. Padlog are also gratefully acknowledged.

This report was typed by Mrs. Deanna L. Kutis.

TABLE OF CONTENTS

<u>Section</u>	<u>Title</u>	<u>Page</u>
	Abstract	ii
	Summary	iii
	Acknowledgement	iv
	List of Tables	vi
	List of Illustrations	vii
1.0	Introduction	1
2.0	Theory	2
3.0	Application	13
4.0	Results and Discussion	20
5.0	Conclusions	92
6.0	Recommendations	93
	Appendix A	94
	Appendix B	105
	Symbols	109
	References	112

LIST OF TABLES

<u>Table</u>	<u>Title</u>	<u>Page</u>
1	SR-5 Operating Conditions	14
2	Unsteady Aerodynamics Data for Case 1	15
3	Unsteady Aerodynamics Data for Case 2	16
4	Unsteady Aerodynamics Data for Case 3	17
5	Unsteady Aerodynamics Data for Case 4	18
6	Contour Values for Modal Plots (Figures 10-21)	38
7	Root Locus Results for First Bending Mode, Case 1	75
8	Root Locus Results for First Bending Mode, Case 2	76
9	Root Locus Results for First Bending Mode, Case 3	77
10	Root Locus Results for First Bending Mode, Case 4	78
11	Implied Operating Conditions at g=0	84
12	SR-5 Operating Conditions for 1st Iteration (10-Bladed Propeller)	86
13	Root Locus Results for First Bending Mode, Case 2, 1st Iteration	87
14	Root Locus Results for First Bending Mode, Case 3, 1st Iteration	88
15	Root Locus Results for First Bending Mode, Case 4, 1st Iteration	89

LIST OF ILLUSTRATIONS

<u>Figure</u>	<u>Title</u>	<u>Page</u>
1	An Advanced Turbopropeller	3
2	NASTRAN Structural and Aerodynamic Models of the Advanced Turbopropeller for Flutter Analysis	4
3	Overall Flowchart of Advanced Turbopropeller Modal Flutter Analysis	7, 8
4	Typical V-g, V-f Curves	10
5	Typical Root Locus Plot	11
6	SR-5 Streamwise Blade Tip Deflections Due to Centrifugal Loads	21
7	SR-5 Steady State Deflections Without Differential Stiffness (Case 3)	22
8	SR-5 Steady State Deflections With Differential Stiffness (Case 3)	23
9	SR-5 Modal Analysis Summary	24
10-15	SR-5 Mode Shapes, 0 rpm, Modes 1-6	26-31
16-21	SR-5 Mode Shapes, 6800 rpm, Modes 1-6 (Case 3)	32-37
22-26	V-g, V-f Curves, Case 1	39-43
27-36	V-g, V-f Curves, Case 2	44-53
37-46	V-g, V-f Curves, Case 3	54-63
47-56	V-g, V-f Curves, Case 4	64-73
57	Root Locus of First Bending Mode (Case 1)	79
58	Root Locus of First Bending Mode (Case 2 and Iteration) . . .	80
59	Root Locus of First Bending Mode (Case 3 and Iteration) . . .	81
60	Root Locus of First Bending Mode (Cases 4 and Iteration) . . .	82
61	Similar Inlet Velocity Triangles	85
62	SR-5 Flutter Analysis Summary	90
63	SR-5 Classical Flutter Summary	91
64	Some Definitions for Swept Blade Aerodynamics	95
65	Chordwise Aerodynamic Modes	96

1.0 INTRODUCTION

As part of the government/industry effort in evolving aircraft of high efficiency, NASA Lewis has been involved in the study of advanced turbopropellers. These devices have many thin blades of a complex shape as compared with conventional propellers. As is historically frequent with advanced aeronautical lifting surfaces, the advanced turbopropeller has shown evidence of flutter problems in wind tunnel tests. In order to compliment and support wind tunnel evidence and other analytical studies, Bell Aerospace Textron has, under NASA sponsorship, modified a computer program previously developed for Bladed Disc Dynamics and applied it to studies of Advanced Turbopropeller Flutter.

This report describes the theoretical background for those modifications and the specific applications and results obtained. The details of the modifications necessary for generalized aerodynamics of varying sweep blades are given in Appendices.

The necessary coding modifications to the aerodynamic modules of the existing program have been documented and the program and documentation have been delivered to NASA Lewis. The program is operational in the NASTRAN General Purpose Computer Program at Level 17.7 on IBM and UNIVAC systems.

2.0 THEORY

Multi-bladed advanced turbopropellers are geometrically cyclic structures with low aspect ratio thin blades of varying sweep. The blades are mounted on a relatively rigid hub (Figure 1) and, therefore, can be considered to be structurally independent. This permits modal analysis of only one root-fixed blade without recourse to special harmonic analysis techniques applicable to cyclic structures. From a flutter aerodynamics viewpoint, the estimation of the generalized oscillatory aerodynamic loads on the propeller blades depends on the aerodynamic theory employed. In the present work, the two-dimensional subsonic cascade unsteady aerodynamic theory of Jones and Rao (Ref. 1) is applied in a strip theory manner with appropriate modifications recognizing the variability of blade sweep with radius.

The following sections discuss the structural and aerodynamic modelling, the equations and the method of modal flutter analysis of advanced turbopropellers.

NASTRAN Structural and Aerodynamic Models

With the assumption of a rigid hub and identical (tuned) blades, it suffices to model only one blade as shown in Figure 2. The finite element capabilities for structural modelling provided in the NASTRAN general purpose finite element program are used.

To facilitate the use of a two-dimensional cascade unsteady aerodynamic theory, the aerodynamic model is based on a grid defined by the intersection of a series of chords and "computing stations" as shown by the thick solid lines in Figure 2.

In order to apply strip theory in a manner similar to that of Ref. 2, the chords are selected normal to any "spanwise" reference curve such as the blade leading edge. The choice of the number and location of the chords and the computing stations is dictated by the expected variation of the relative flow

ORIGINAL PAGE IS
OF POOR QUALITY



Figure 1. An Advanced Turbopropeller

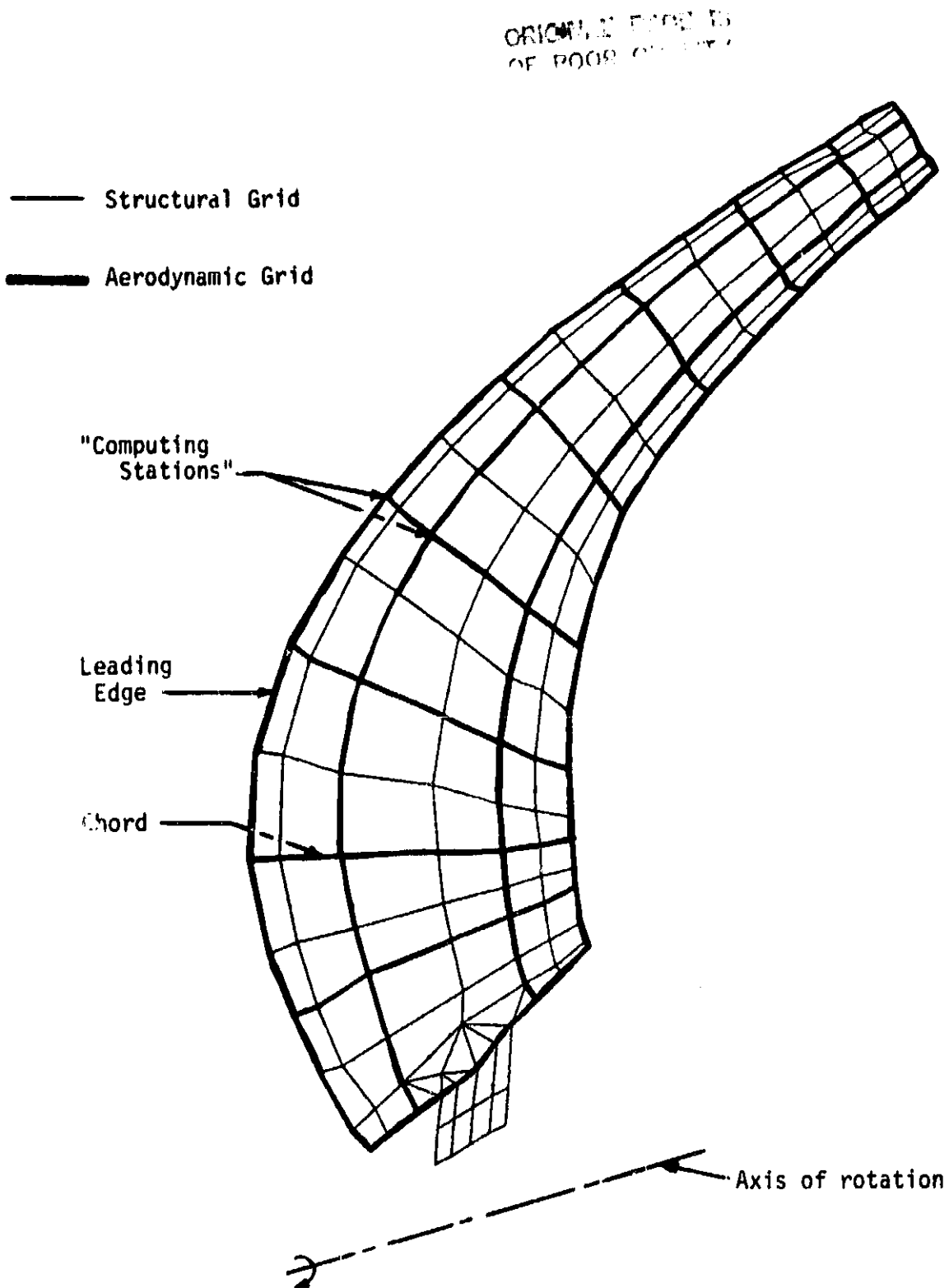


Figure 2. NASTRAN Structural and Aerodynamic Models of the Advanced Turbopropeller for Flutter Analysis

properties across the blade span, and the complexity of the mode shapes exhibited by the propeller blade. Due to its resemblance to the structural model of the blade, and the adequacy of a relatively coarse grid to describe the spanwise flow variations, the aerodynamic model is chosen as a subset of the structural model as shown in Figure 2.

Equations of Motion for Modal Flutter Analysis

If $\{u\}$ represents the physical degrees of freedom of any one representative blade, the equations of motion for flutter analysis of the advanced turbopropeller can be written as

$$[M] \{\ddot{u}\} + (1 + ig) \left[[K^e] + [K^d] \right] \{u\} - [Q] \{u\} = \{0\}, \quad (1)$$

where M is the mass matrix, K^e is the elastic stiffness matrix, K^d and Q are the differential stiffness matrix and the aerodynamic coefficient matrix, respectively, at the operating condition being considered. For the KE method of flutter analysis (Ref. 3) used in the present work, an artificial structural damping parameter g is introduced in the flutter equations. Although the assumption of harmonic motion in deriving the aerodynamic coefficients limits the flutter equations and their solutions to be strictly valid only at $g=0$, $g \rightarrow 0^+$ is taken to represent a stable system approaching flutter.

For modal flutter analysis, equations (1) are reformulated with the undamped structural modes $[\phi]$, computed with the effects of steady state loads taken into account, as the bases:

$$\left[-\omega^2 [M_{ii}] + (1 + ig) [K_{ii}] - [Q_{ii}] \right] \{\bar{x}_i\} = \{0\}, \quad (2)$$

where

$$\begin{aligned} \{u\} &= \{\bar{u}\} e^{i\omega t} = [\phi] \{\bar{x}_i\} e^{i\omega t}, \\ [M_{ii}] &= [\phi]^T [M] [\phi], \\ [K_{ii}] &= [\phi]^T \left[[K^e] + [K^d] \right] [\phi], \text{ and} \\ [Q_{ii}] &= [\phi]^T [Q] [\phi]. \end{aligned} \quad \left. \right\} \quad (3)$$

A detailed derivation of the generalized aerodynamic coefficients matrix Q_{ij} for the swept blades of advanced turbopropellers is presented in Appendix A.

For the KE method of flutter analysis in NASTRAN, equations (2) are rewritten as a complex eigenvalue problem

$$[\bar{M}_{ii}] p^2 + [K_{ii}] \{\bar{\xi}_i\} = \{0\}, \quad (4)$$

where

$$p = \frac{iV_{s,ref}}{\sqrt{1+ig}} = V_{s,ref} \left(\frac{g}{2} + i \right) \text{ is the complex eigenvalue,}$$

$$[\bar{M}_{ii}] = \left(\frac{k_{s,ref}}{\omega_{s,ref}} \right)^2 [M_{ii}] + \frac{\rho_{s,ref}}{2} [\bar{Q}_{ii}],$$

$$[\bar{Q}_{ii}] = \frac{1}{\frac{1}{2} \rho_{s,ref} V_{s,ref}^2} [Q_{ii}], \text{ and}$$

$$\omega_{s,ref} = \frac{\omega_{s,ref}}{V_{s,ref}} \text{ is the reduced frequency.}$$

} (5)

Method of Flutter Analysis

An overall flowchart for modal flutter analysis of advanced turbopropellers is shown in Figure 3.

For an N -bladed propeller with the blades set at a known reference pitch angle, the operating condition to be examined for stability is defined in terms of rotational speed and free stream density, velocity and Mach number.

The steady state loads are used to estimate the differential stiffness of the propeller blade. In the examples presented in this report, the differential stiffness due to only centrifugal loads is estimated by iteratively solving

$$[[K^e] + [K^d(u)]]\{u\} = P^{cf} \quad (6)$$

for u to determine $K^d(u)$.

The real eigenvalue problem

$$[-\omega^2[M] + [[K^e] + [K^d]]]\{\bar{u}\} = \{0\} \quad (7)$$

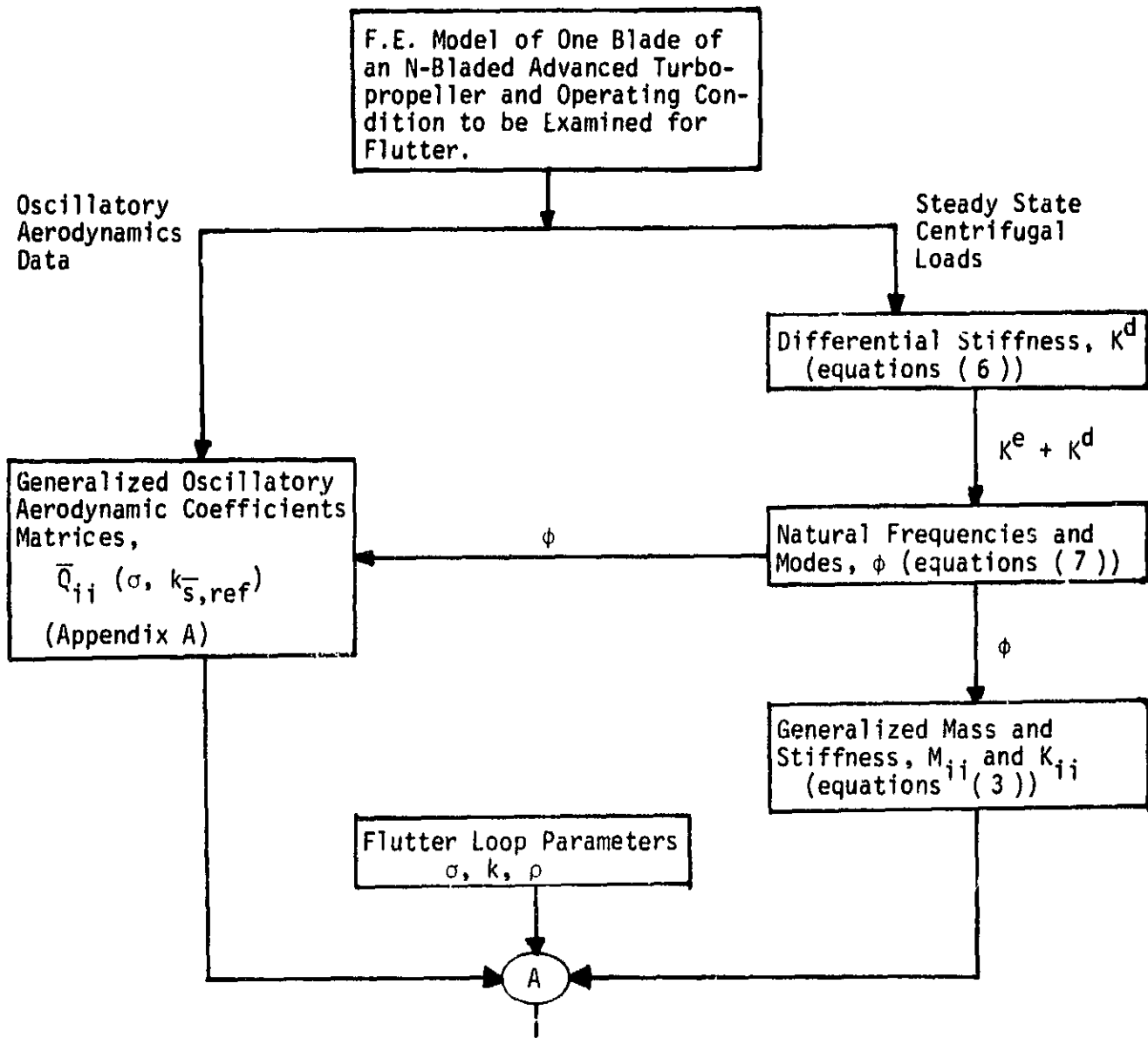


Figure 3. Overall Flowchart of Advanced Turbopropeller Modal Flutter Analysis (continued).

ORIGINAL PAGE IS
OF POOR QUALITY

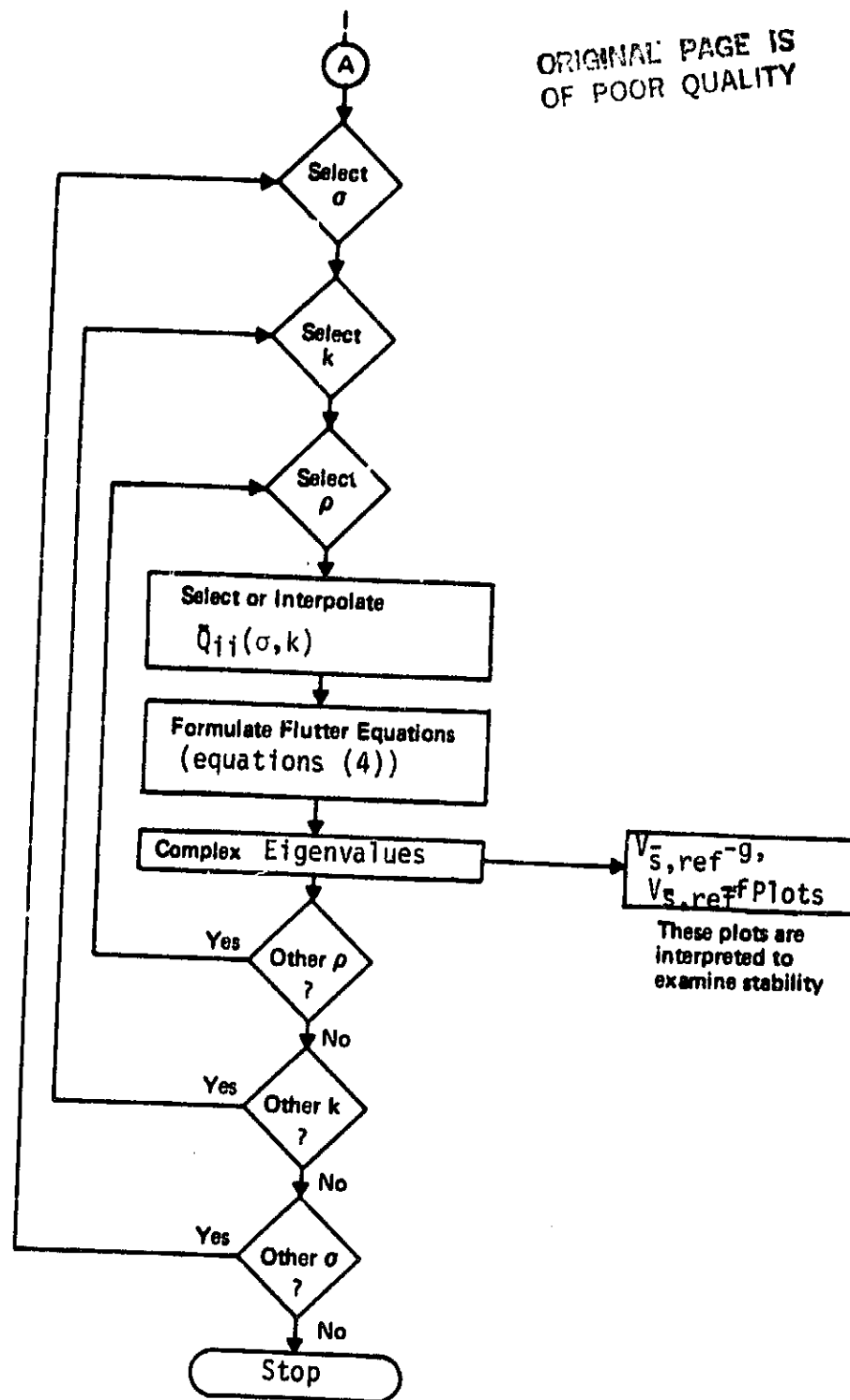


Figure 3. Overall Flowchart of Advanced Turbopropeller Modal Flutter Analysis (Concluded)

is solved to determine the natural frequencies and mode shapes of the propeller blade.

For selected values of reduced frequency, $k_{s,\text{ref}}$, and all possible values of the inter-blade phase angle, σ , a series of generalized oscillatory aerodynamic coefficients matrices \bar{Q}_{ij} is computed as shown in Appendix A.

For each of the possible combinations of $(\rho_{s,\text{ref}}, k_{s,\text{ref}}, \sigma)$, the complex eigenvalues of the flutter equations, (4), are determined. The complex eigenvalue

$$p = V_{s,\text{ref}} \left(\frac{g}{2} + i \right)$$

yields

$$V_{s,\text{ref}} = \text{Im}(p) ,$$

$$g = 2 \text{Re}(p)/V_{s,\text{ref}}, \text{ and}$$

$$f = \frac{1}{2\pi} \cdot \frac{k_{s,\text{ref}} \cdot V_{s,\text{ref}}}{\rho_{s,\text{ref}}} .$$

For each $(\rho_{s,\text{ref}}, \sigma)$ combination, $V_{s,\text{ref}}-g$ and $V_{s,\text{ref}}-f$ plots of the type shown in Figure 4 are generated. At the $(\rho_{s,\text{ref}}, V_{s,\text{ref}})$ representing the operating condition being examined, the stability of each of the structural modes included for flutter analysis is examined by the value of the damping parameter g being ≤ 0 . $g > 0$ indicates an unstable mode. In Figure 4, mode 1 (first bending) with an in-vacuo frequency of 187.9 Hz. ($V_{s,\text{ref}} = 0$) is seen to be unstable at the operating condition $V_{s,\text{ref}} = 7046$ in/sec. at an inter-blade phase angle of -108 degrees.

The root locus of this mode with inter-blade phase angle as the parameter, at the $(\rho_{s,\text{ref}}, V_{s,\text{ref}})$ representing the operating condition is shown in Figure 5. The ordinate is the non-dimensional frequency $v = f/f_{\text{vacuum}}$, and the abscissa is the non-dimensional damping $\mu = (g/2) \cdot v$. It is seen that this mode is unstable for $\sigma = 72^\circ, 180^\circ, -144^\circ, -108^\circ$ and -72° , with -108° and -72° representing the most and the least unstable conditions, respectively.

ORIGINAL PAGE IS
OF POOR QUALITY

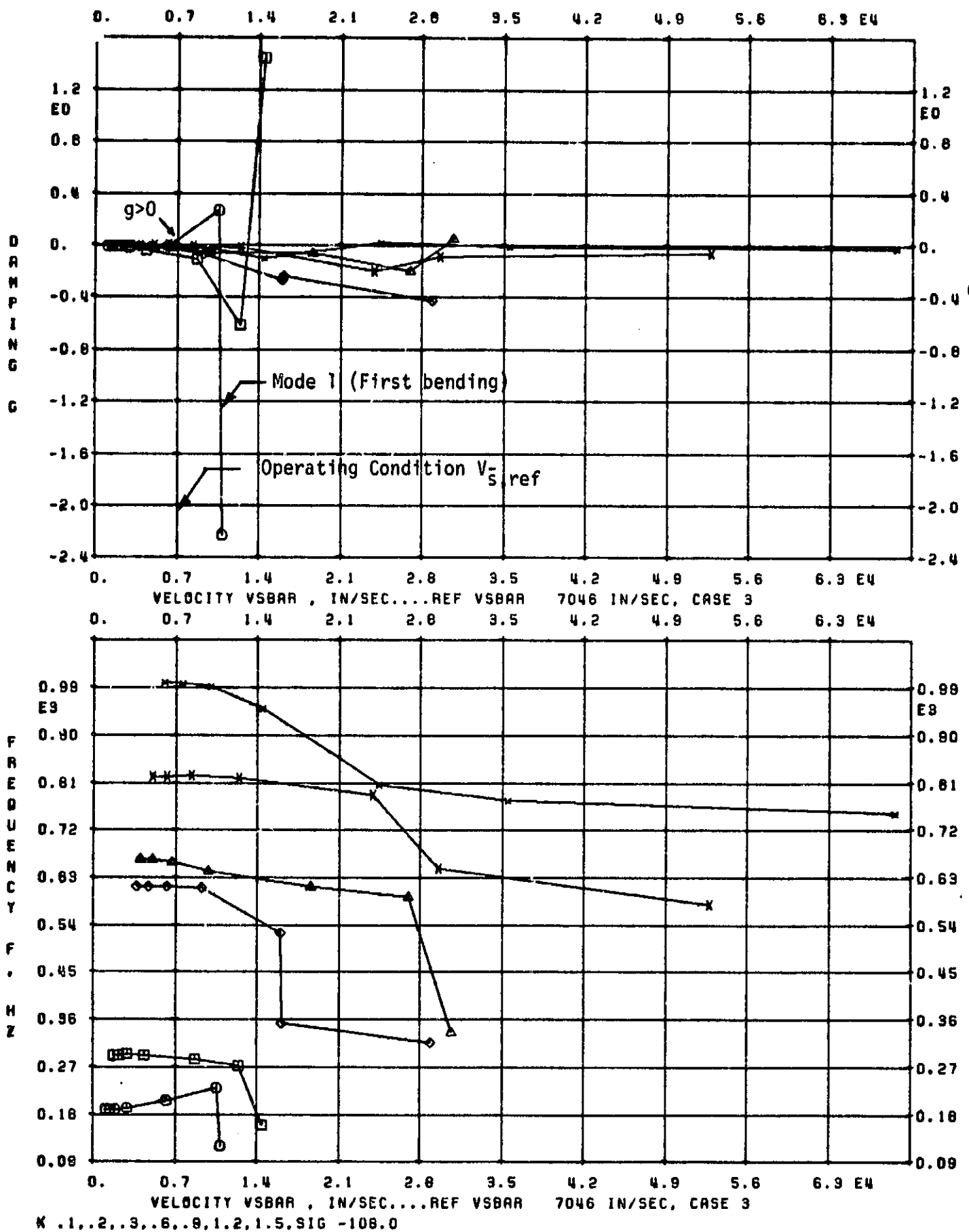


Figure 4. Typical V-g, V-f Curves

SR-5 FLUTTER ANALYSIS AT 6800 RPM (10 BLADES)
 ROOT LOCUS OF FIRST BENDING MODE (FREQ IN VACUUM = 187.9 Hz.)

ORIGINAL PAGE IS
 OF POOR QUALITY

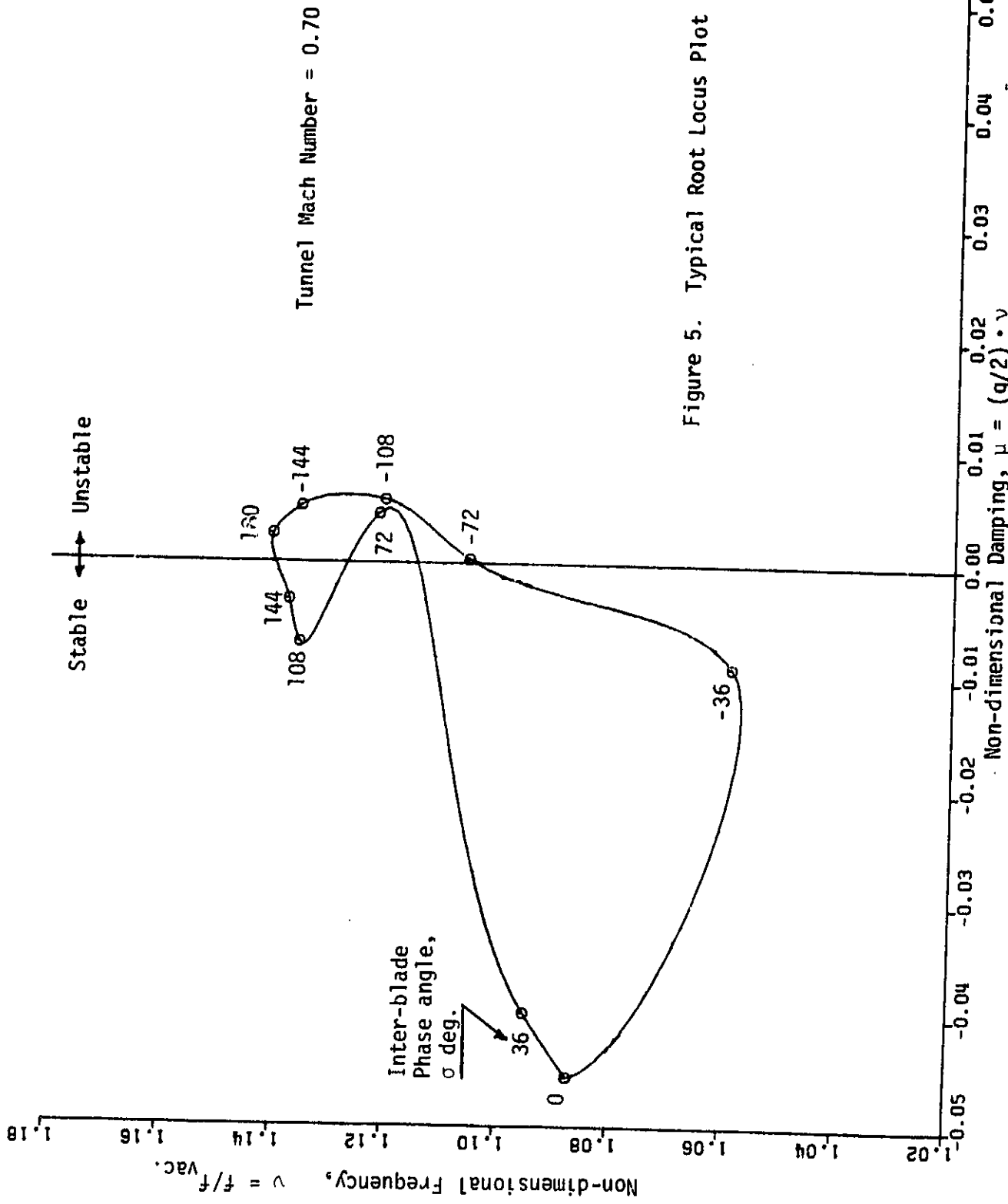


Figure 5. Typical Root Locus Plot

With regards to the use of two-dimensional subsonic cascade unsteady aerodynamic theories, it is relevant to mention that for certain combinations of Mach number, inter-blade phase angle, blade spacing to chord ratio and stagger angle, there exist critical values of reduced frequency about which the aerodynamic coefficients are very sensitive, and at which they vanish (Ref. 4). A brief description of such "acoustic resonance" conditions is given in Ref. 5. In the case of the advanced turbopropeller application, however, the extent to which such conditions on isolated chords influence the generalized aerodynamic matrix and therefore affect the flutter results, is difficult to judge. Although no attempt has been made in this report to study the influence of the presence of acoustically resonant chords, the following points are offered:

1. At any given operating condition, the ratio of the work done by the aerodynamic forces on the strips associated with all "acoustically resonant" chords to the work done by the aerodynamic forces on the entire blade in any given structural mode may be a good indication of the influence of the acoustic resonance.
2. By increasing the number of chords spanning the blade, the aerodynamic work done per strip can be reduced.
3. Due to the large spanwise variation in the parameters defining the critical reduced frequencies, it may be possible to eliminate acoustic resonance conditions by relocating some of the blade chords.

The method of flutter analysis discussed in this section can be repeated at other operating conditions till neutrally stable structural modes are found. The subsonic classical flutter boundary may then be defined.

3.0 APPLICATION

The theoretical development of the preceding section, as implemented in the NASTRAN general purpose finite element program (Ref. 6), was applied to conduct the modal flutter analysis of the SR-5 advanced turbopropeller developed by the NASA Lewis Research Center and the Hamilton Standard Division of the United Technologies Corporation. Two (five- and ten-bladed) propellers were analyzed.

The four operating conditions for analysis were selected by NASA LeRC from wind tunnel test conditions, and are shown in Table 1.

The propeller hub was considered rigid compared to blades, and only one of the blades was modelled. The NASTRAN structural model, shown in Figure 2, consisted of 130 bending-cum-membrane plate elements with a total of 155 grid points.

The aerodynamic model, also shown in Figure 2, consisted of 10 chords with four computing stations each. The chords were selected approximately normal to the blade leading edge. For the four operating conditions, the corresponding unsteady aerodynamics data are presented in Tables 2 through 5. For case 3, the rate of change of blade chord with spanwise reference distance, $\partial c_s / \partial z$, was computed from a finer (20 chords) mesh.

To investigate flutter instability, the following steps were taken at each of the operating conditions:

1. Centrifugal loads at the operating rpm were applied to the as manufactured (pretwisted) blade shape to compute the differential stiffness.
2. The displacements at the end of the differential stiffness calculations were added to the pretwisted blade shape to define the deformed blade shape. The elastic and differential stiffnesses were then used to determine the natural frequencies and mode shapes of the deformed blade.

ORIGINAL PAGE IS
OF POOR QUALITY

TABLE I. SR-5 OPERATING CONDITIONS

Case No.	NASA Test Reading No.	RPM	No. of Blades	Free Stream Conditions			Mach No. M_∞
				Blade Setting Angle	Velocity ft/sec	Density Slug/ft ³	
1	7646	6900	5	69.0°	911.7	1.8411 E-3	0.85
2	6221	6000	10	69.0°	865.7	1.9534 E-3	0.80
3	7725	6800	10	69.0°	778.0	2.0244 E-3	0.70
4	7739	6200	10	69.0°	921.6	1.7756 E-3	0.85

ORIGINAL PAGE IS
OF POOR QUALITY

TABLE 2 . UNSTEADY AERODYNAMICS DATA FOR CASE 1

Chord No. \bar{s}	Stagger Angle, $\lambda_{\bar{s}}$, deg.	Chord, $c_{\bar{s}}$, in.	$\frac{\partial c_{\bar{s}}}{\partial \bar{z}}$	Blade Spacing, $B_{\bar{s}}$, in.	Relative Inflow Mach No., $M_{\bar{s}}$	Relative Inflow Velocity $V_{\bar{s}}$, in/sec.	Sweep Angle, $\Lambda_{\bar{s}}$, deg.
1 (root)	11.078	3.028	.266	3.252	.829	10,671	-15.896
2	13.903	3.559	.322	5.466	.883	11,361	2.894
3	14.964	4.129	.041	7.636	.853	10,982	20.212
4	16.540	4.214	-.433	10.136	.735	9,463	38.823
5	17.818	3.543	-.435	11.651	.671	8,640	46.120
6 (ref.)	16.343	2.905	-.395	12.846	.626	8,061	50.140
7	18.140	2.377	-.358	13.831	.632	8,138	50.791
8	20.242	1.938	-.394	14.701	.654	8,423	50.308
9	23.771	1.558	-.418	15.366	.651	8,379	51.881
10 (tip)	28.032	1.280	-.418	15.830	.682	8,778	50.951

TABLE 3. UNSTEADY AERODYNAMICS DATA FOR CASE 2

ORIGINAL PAGE IS
OF POOR QUALITY

Chord No. \bar{S}	Stagger Angle, $\lambda_{\bar{S}}$, deg.	Chord, $c_{\bar{S}}$, in.	$\frac{\partial c_{\bar{S}}}{\partial \bar{Z}}$	Blade Spacing, $B_{\bar{S}}$, in.	Relative No., $M_{\bar{S}}$	Inflow Mach	Relative Inflow Velocity $V_{\bar{S}}$, in/sec.	Sweep Angle, $\lambda_{\bar{S}}$, deg.
1 (root)	11.057	3.628	.266	1.626		.778	10,104	-15.918
2	13.838	3.559	.322	2.732		.826	10,727	2.858
3	14.813	4.130	.041	3.817		.797	10,344	20.154
4	16.133	4.214	-.434	5.067		.684	8,882	38.738
5	16.912	3.540	-.436	5.824		.622	8,074	46.048
6 (ref.)	14.843	2.902	-.396	6.421		.577	7,495	50.109
7	16.188	2.372	-.358	6.912		.579	7,520	50.818
8	18.122	1.933	-.393	7.344		.597	7,746	50.419
9	21.622	1.555	-.417	7.674		.591	7,669	52.104
10 (tip)	25.977	1.277	-.417	7.904		.617	8,009	51.271

TABLE 4. UNSTEADY AERODYNAMICS DATA FOR CASE 3

Chord No. \bar{s}	Stagger Angle, $\lambda_{\bar{s}}$, deg.	Chord, $c_{\bar{s}}$, in.	$\frac{\partial c_{\bar{s}}}{\partial \bar{z}}$	Blade Spacing, $B_{\bar{s}}$, in.	Relative Inflow Mach No., $M_{\bar{s}}$	Relative Inflow Velocity $V_{\bar{s}}$, in./sec.	Sweep Angle, $\Lambda_{\bar{s}}$, deg.
1 (root)	11.075	3.028	.278	1.626	.686	9,152	-15.899
2	13.895	3.559	.336	2.733	.734	9,794	2.890
3	14.946	4.129	.152	3.818	.713	9,512	20.206
4	16.492	4.214	-.355	5.068	.618	8,246	38.813
5	17.712	3.542	-.389	5.825	.567	7.558	46.112
6 (ref.)	16.167	2.905	-.367	6.423	.528	7,046	50.138
7	17.910	2.376	-.316	6.915	.535	7,139	50.796
8	19.990	1.557	-.369	7.350	.556	7,419	50.323
9	23.516	1.558	-.294	7.682	.557	7,424	51.910
10 (tip)	27.788	1.280	-.541	7.913	.587	7,830	50.992

TABLE 5. UNSTEADY AERODYNAMICS DATA FOR CASE 4

Chord No. $\frac{S}{S}$	Stagger Angle, λ_S , deg.	Chord, c_S , in.	$\frac{\partial c_S}{\partial z}$	Blade Spacing, B_S , in.	Relative Inflow Mach: No., M_S	Relative Inflow Velocity V_S , in/sec.	Swept Angle A_S , deg.
1 (root)	11.961	3.028	.266	1.626	.826	10,748	-15.913
2	13.851	3.559	.322	2.732	.876	11,399	2.865
3	14.845	4.130	.041	3.817	.844	10,983	20.166
4	16.218	4.214	-.434	5.067	.724	9,421	38.755
5	17.103	3.541	-.436	5.824	.658	8,562	46.064
6 (ref.)	15.159	2.902	-.396	6.421	.612	7,957	50.117
7	16.596	2.373	-.358	6.913	.614	7,985	50.816
8	18.560	1.934	-.393	7.345	.632	8,223	50.399
9	22.068	1.555	-.417	7.676	.625	8,133	52.062
10 (tip)	26.403	1.278	-.417	7.906	.652	8,482	51.208

3. The first six structural modes of the deformed blade were used to derive the generalized aerodynamic forces on the blade. The KE method of modal flutter analysis was used to obtain the subcritical, critical (flutter) and supercritical eigenvalues and to generate the V-g and V-f curves.
4. The V-g curves were interpreted to determine the stability of the structural modes. For the unstable modes, the root locus plots with inter-blade phase angle as the parameter were analyzed to determine the dominant flutter inter-blade phase angle.

For the 10-bladed propeller (Table 1, cases 2-4), steps 3 and 4 were repeated once in order to locate the neutrally stable operating conditions (flutter boundary). In order to retain the structural modes computed in step 2, rpm's were unchanged while varying the free stream Mach numbers.

The results of the analysis are presented and discussed in Section 4.

4.0 RESULTS AND DISCUSSION

Results of differential stiffness, modal and flutter analyses for all the cases discussed in the preceding section are presented with a view to

1. determine if the given operating conditions (cases 1 through 4) are stable or unstable, and
2. locate the subsonic classical flutter boundary for the 10-bladed propeller (cases 2 through 4, and their iterations).

Figure 6 schematically illustrates the streamwise blade tip deflections obtained at the end of the differential stiffness computations for cases 1 through 4. These computations included the effects of only centrifugal loads and neglected those due to steady state airloads. The blade tip, represented by a straight chord, is seen to deflect 4.3 degrees to 5.8 degrees as the propeller speed varies from 6000 to 6900 rpm.

Figures 7 and 8 are for case 3, and typically show the deformed blade shapes obtained by excluding and including the differential stiffness, respectively.

Figure 9 presents a summary of the modal analysis of the SR-5 blade for cases 1 through 4 and static condition (0 rpm). The differential stiffness was included for each case in determining the natural frequencies and mode shapes. Bench test frequencies available for the first four natural modes, under static conditions, are also shown in the figure. Excellent agreement with analysis is indicated except for the third mode frequency which is predicted about 16% higher. As seen in Figure 12, this is primarily the first torsion mode about the blade pitch axis, and the higher frequency is possibly due to the over-representation of the torsional stiffness by using plate elements near the blade root and shank.

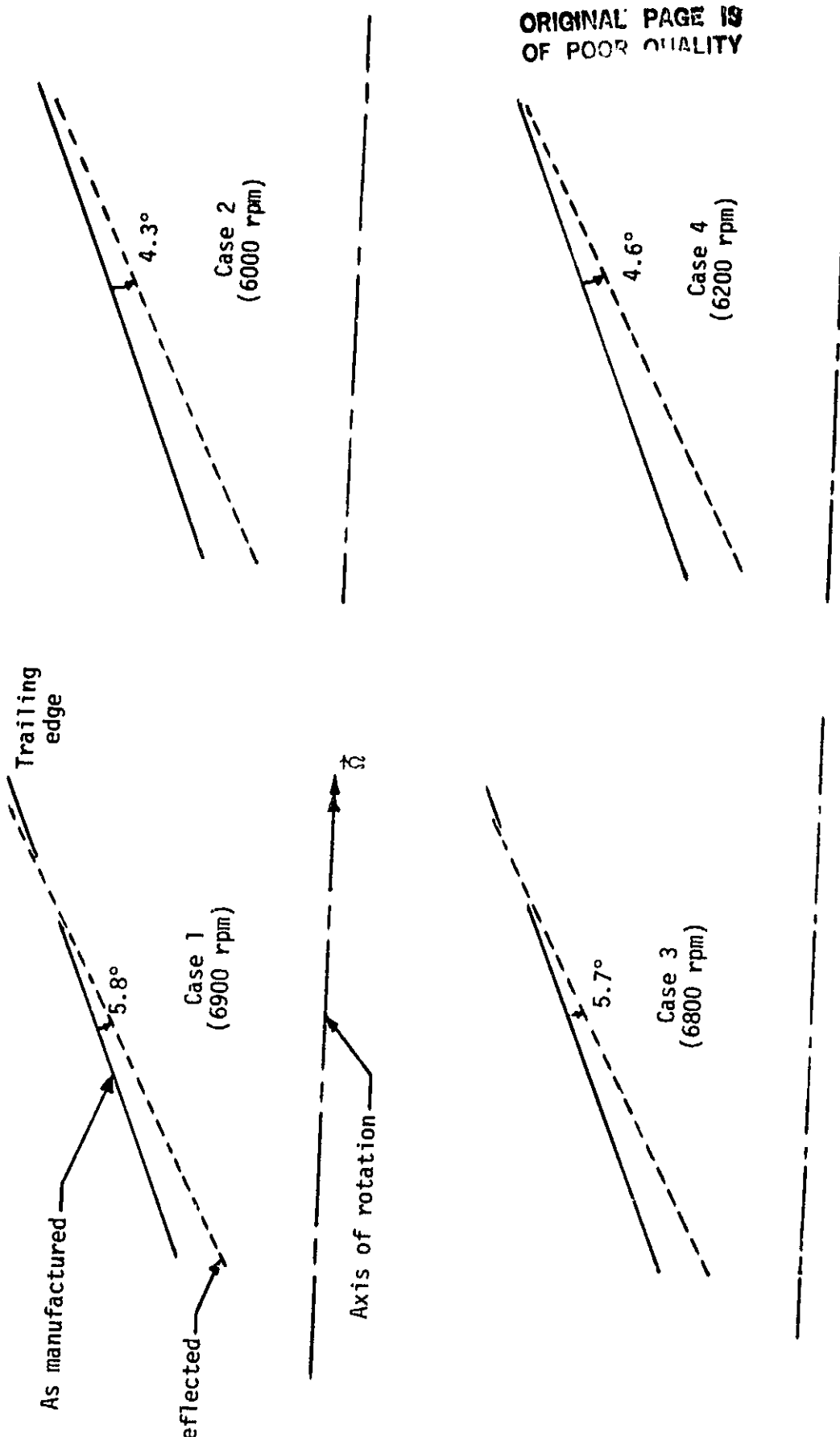


Figure 6. SR-5 STREAMWISE BLADE TIP DEFLECTIONS DUE TO CENTRIFUGAL LOADS

ORIGINAL PAGE IS
OF POOR QUALITY

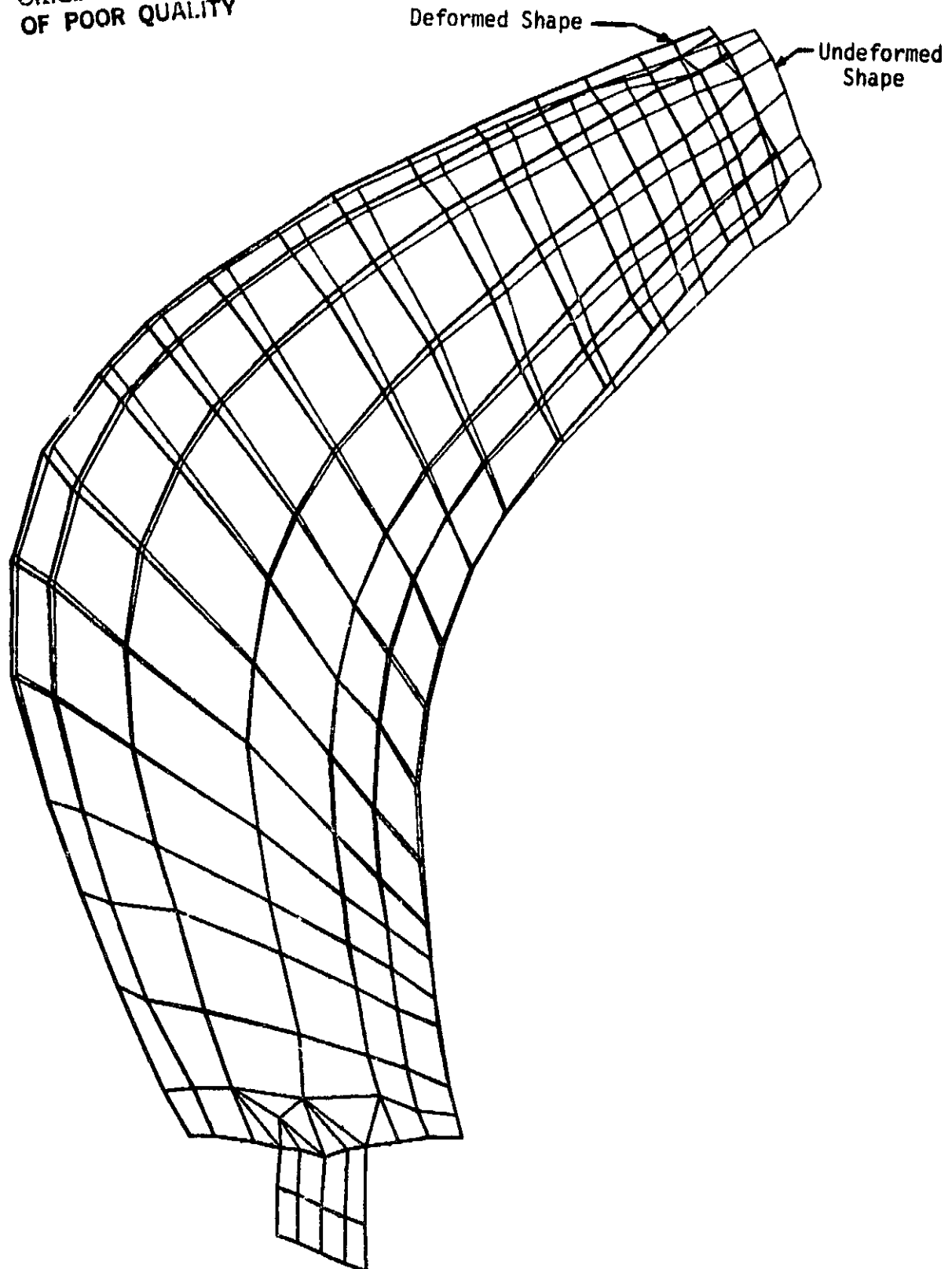


Figure 7. SR-5 Steady State Deflections Without Differential Stiffness
(Case 3)

ORIGINAL PAGE IS
OF POOR QUALITY

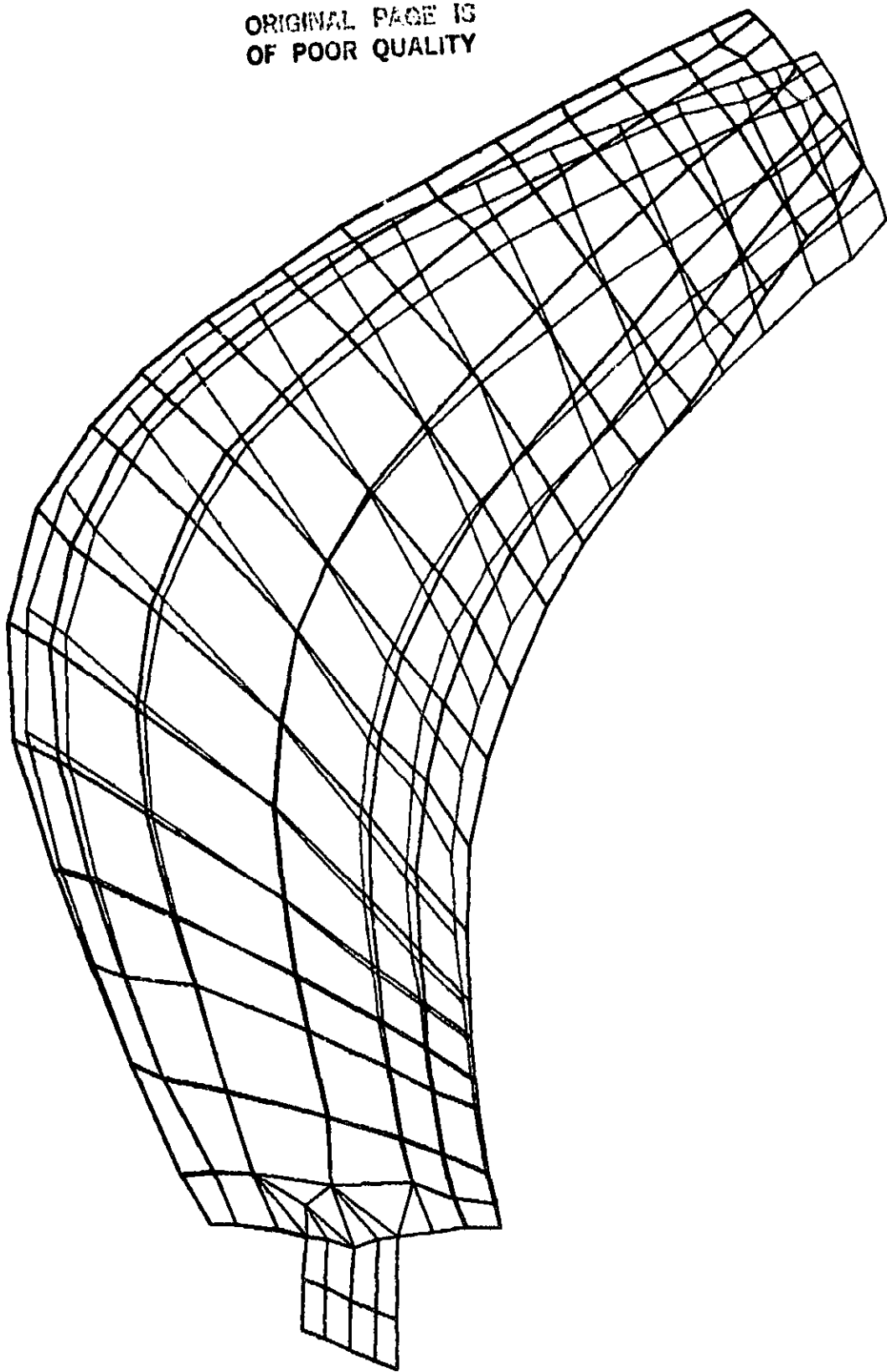
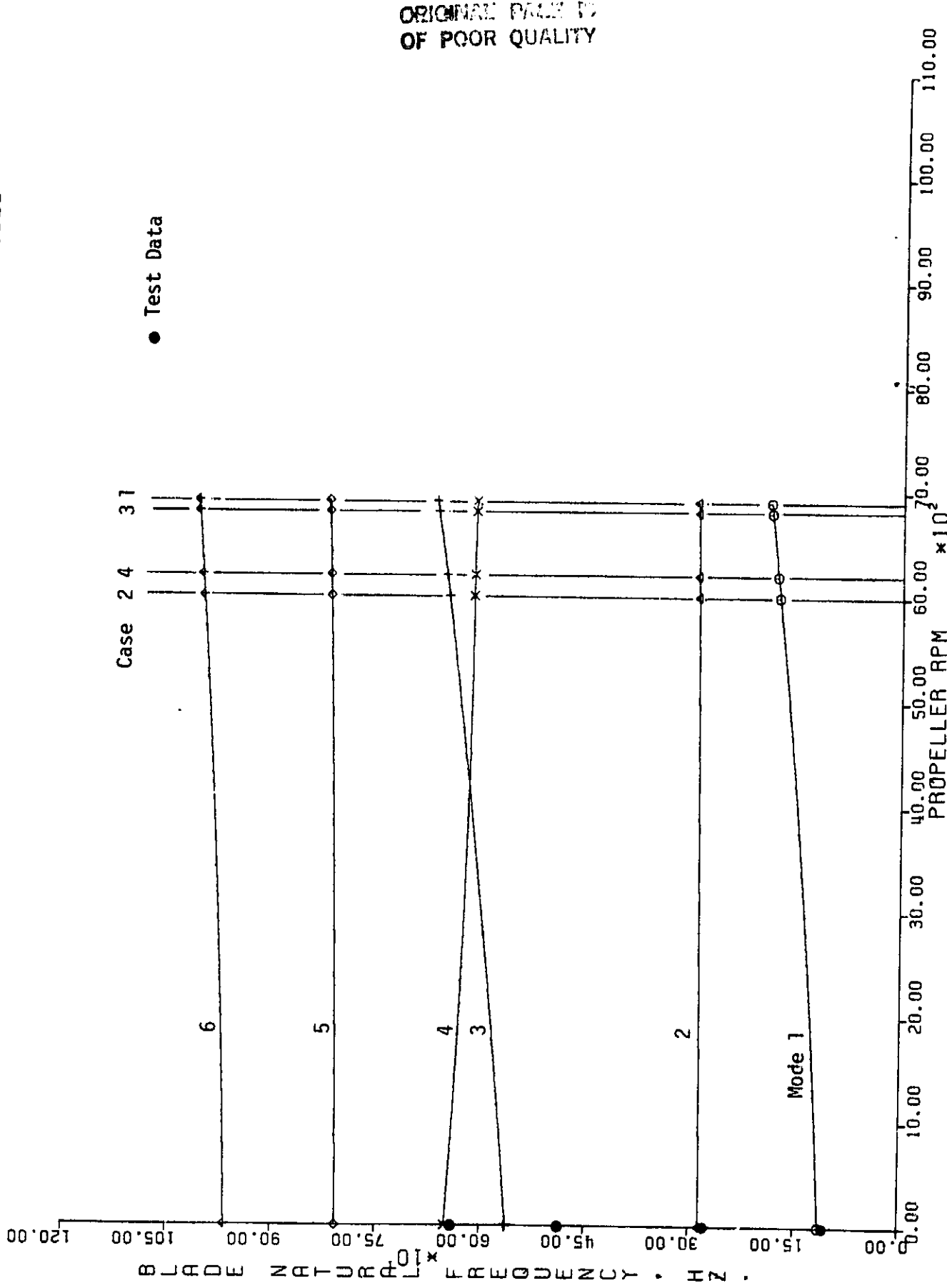


Figure 8. SR-5 Steady State Deflections with Differential Stiffness
(Case 3)

FIGURE 9. SR-5 MODAL ANALYSIS SUMMARY
DIFFERENTIAL STIFFNESS DUE TO CENTRIFUGAL LOADS INCLUDED



Figures 10 through 15 , and 16 through 21 , respectively, represent the SR-5 blade mode shapes under static and case 3 conditions. Table 6 lists the contour values for these figures. Figures 10 through 13 also show the mode shapes determined by holographic bench tests. The comparison between the computed and observed mode shapes is generally good.

Figures 22 through 26 (case 1), 27 through 36 (case 2), 37 through 46 (case 3) and 47 through 56 (case 4) are the V-g, V-f curves generated by the solution of the flutter equations as a complex eigenvalue problem. For each of these figures,

1. the density of the inflow was constant, and as given by Table 1 ,
2. the inter-blade phase angle was constant at one of its permissible values:

$$\sigma = 2\pi n/N ,$$

with N = the number of blades on the propeller,

$$n = 0, \pm 1, \pm 2, \dots, \pm N_1, N_2,$$

where for N odd,

$$N_1 = (N-1)/2, N_2 \text{ does not exist, and}$$

for N even,

$$N_1 = (N-2)/2, N_2 = N/2,$$

3. the reduced frequency at reference chord, $k_{s,\text{ref}}$, was varied as 0.1, 0.2, 0.3, 0.6, 0.9, 1.2 and 1.5 to cover the frequency range of the first six structural modes,
4. a vertical line at the $V_{s,\text{ref}}$ corresponding to the operating condition is drawn to facilitate determination of the equilibrium of the various structural modes from the V-g curves.

With regards to the V-g, V-f curves for all four cases, the following general observations are made:

1. At the given operating conditions, the frequencies of modes 1, 3 and 5 increased, with mode 1 gaining the most. The frequencies of modes 2, 4 and 6 decreased marginally.

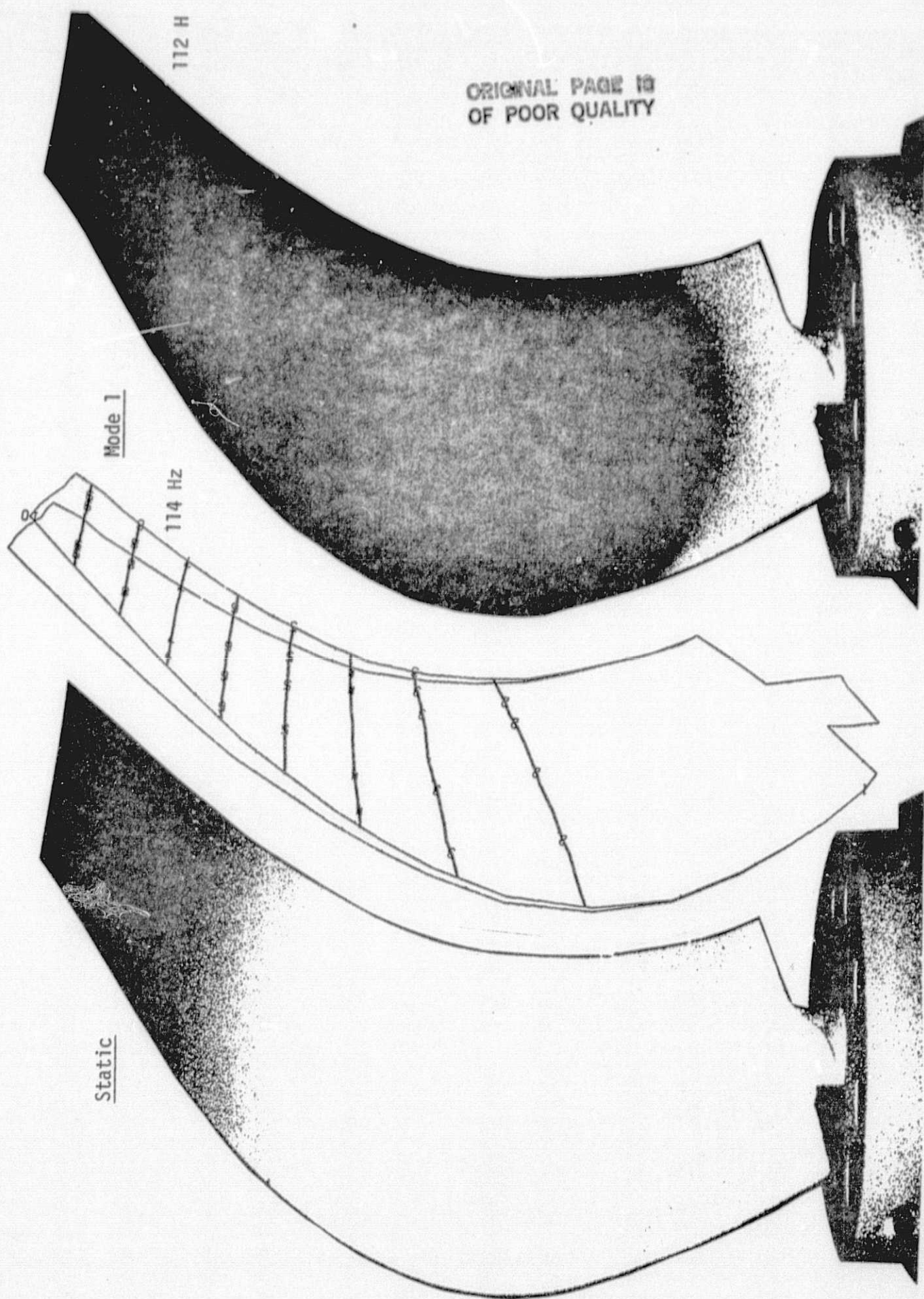
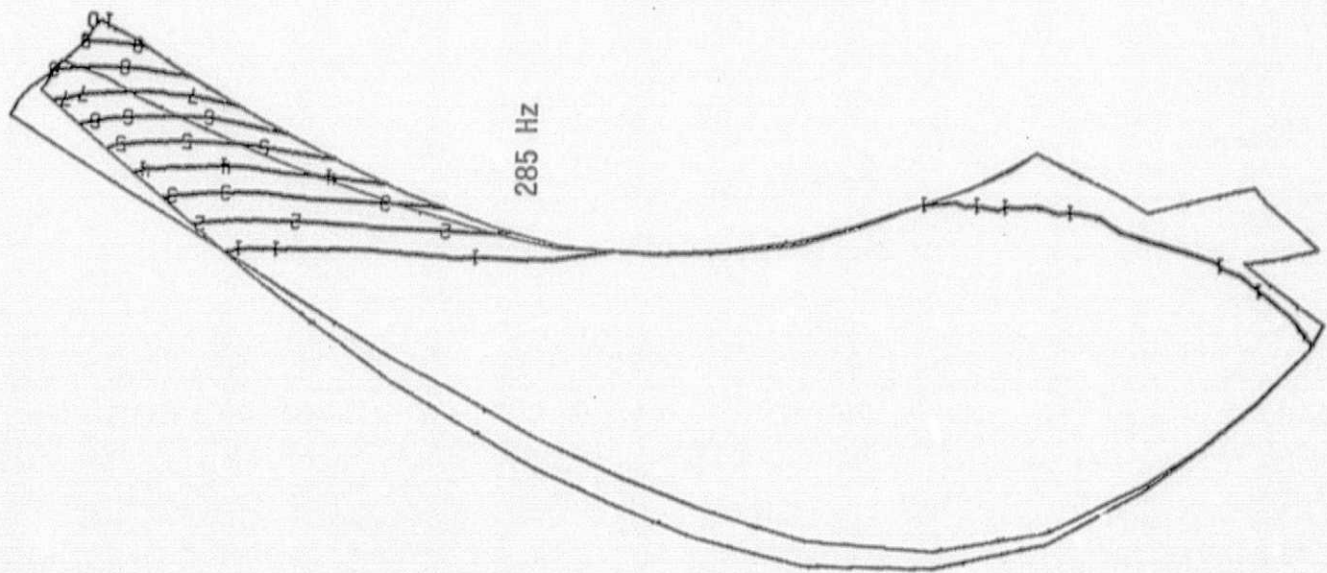


Figure 10 . SR-5 Mode Shapes, 0 rpm, Mode 1

ORIGINAL PAGE IS
OF POOR QUALITY

278 Hz



285 Hz

Figure 11. SR-5 Mode Shapes, 0 rpm, Mode 2

ORIGINAL PAGE IS
OF POOR QUALITY

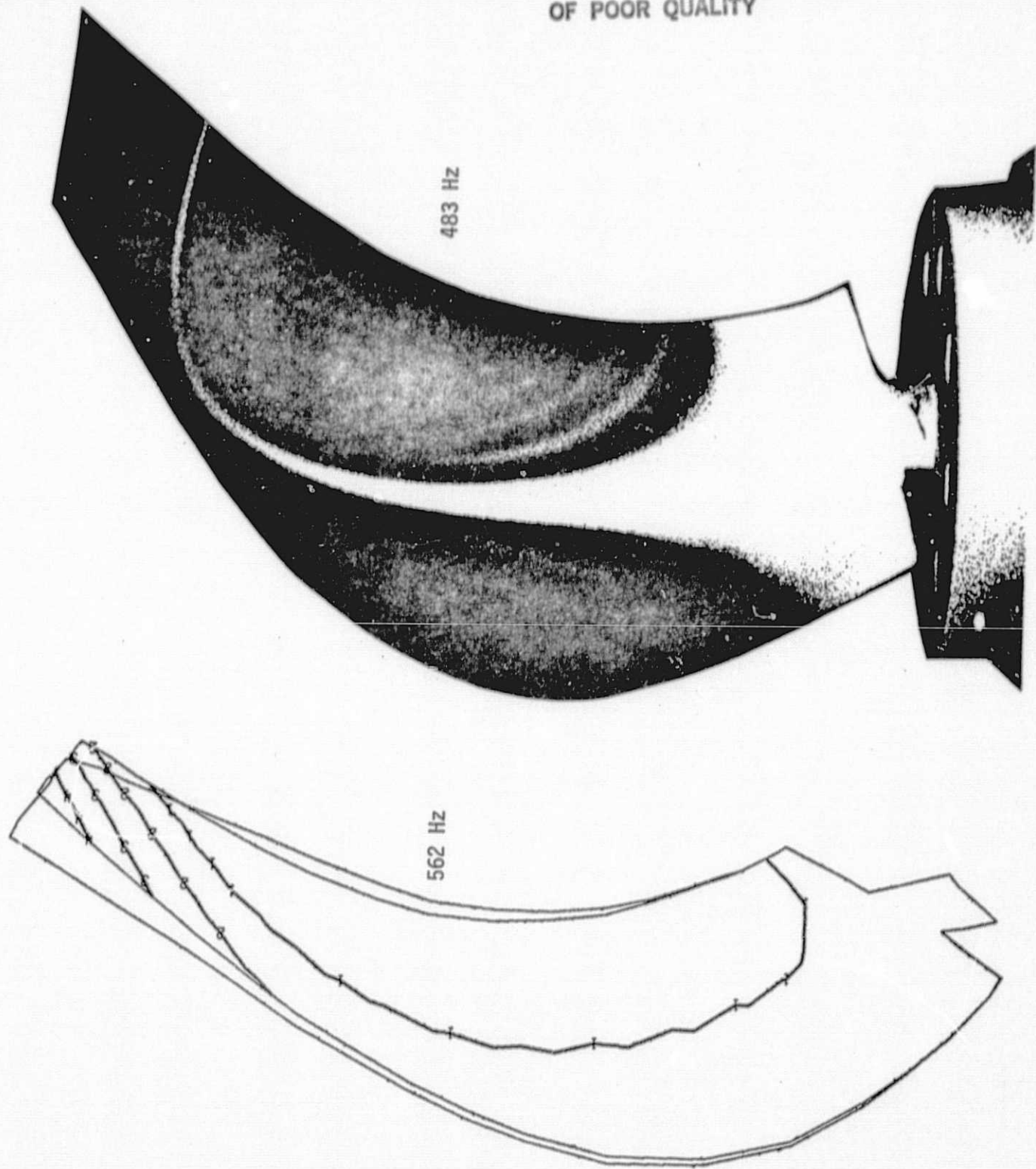


Figure 12. SR-5 Mode Shapes, 0 rpm, Mode 3

ORIGINAL PAGE IS
OF POOR QUALITY

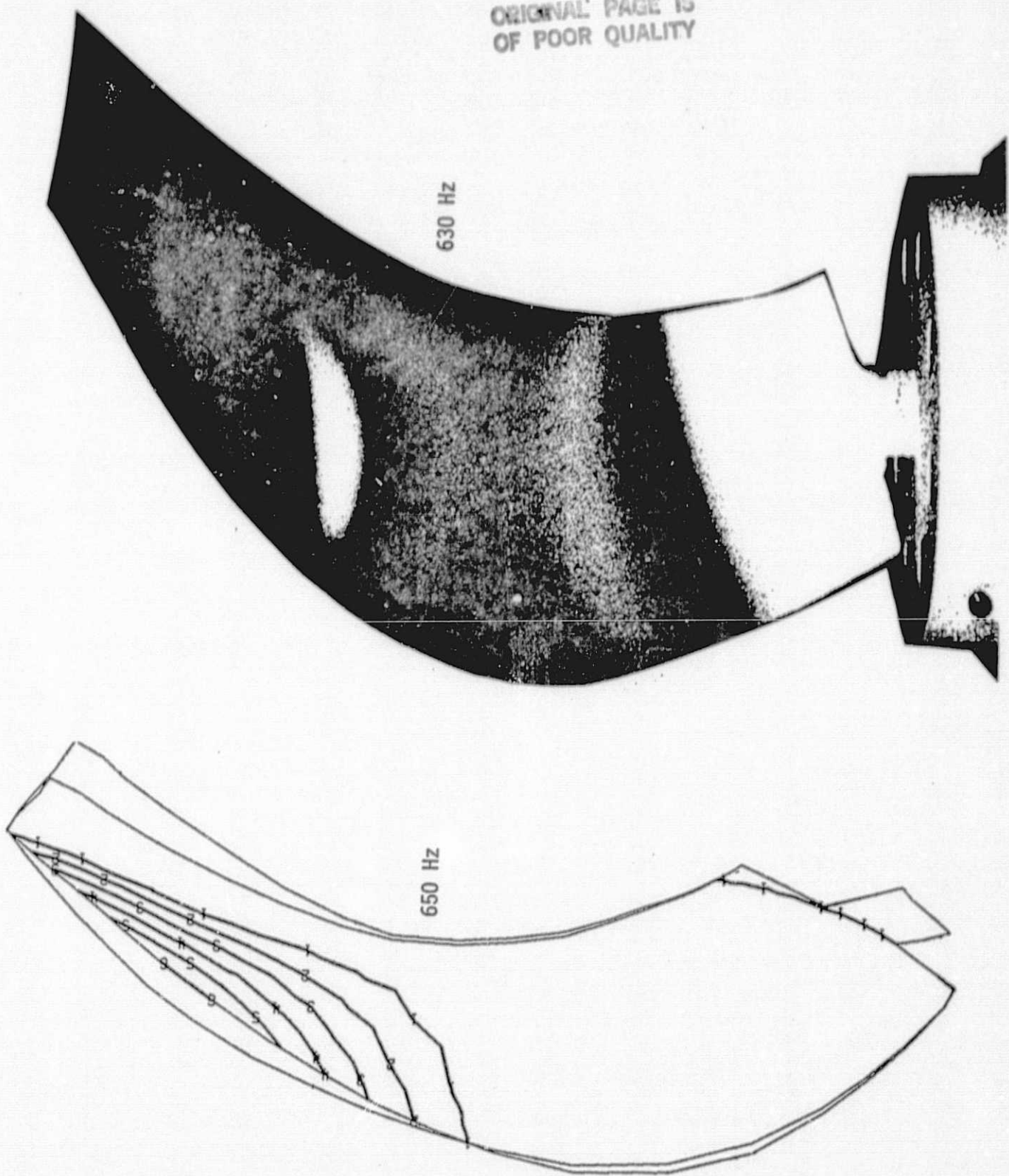


Figure 13. SR-5 Mode Shapes, 0 rpm, Mode 4

ORIGINAL PAGE IS
OF POOR QUALITY

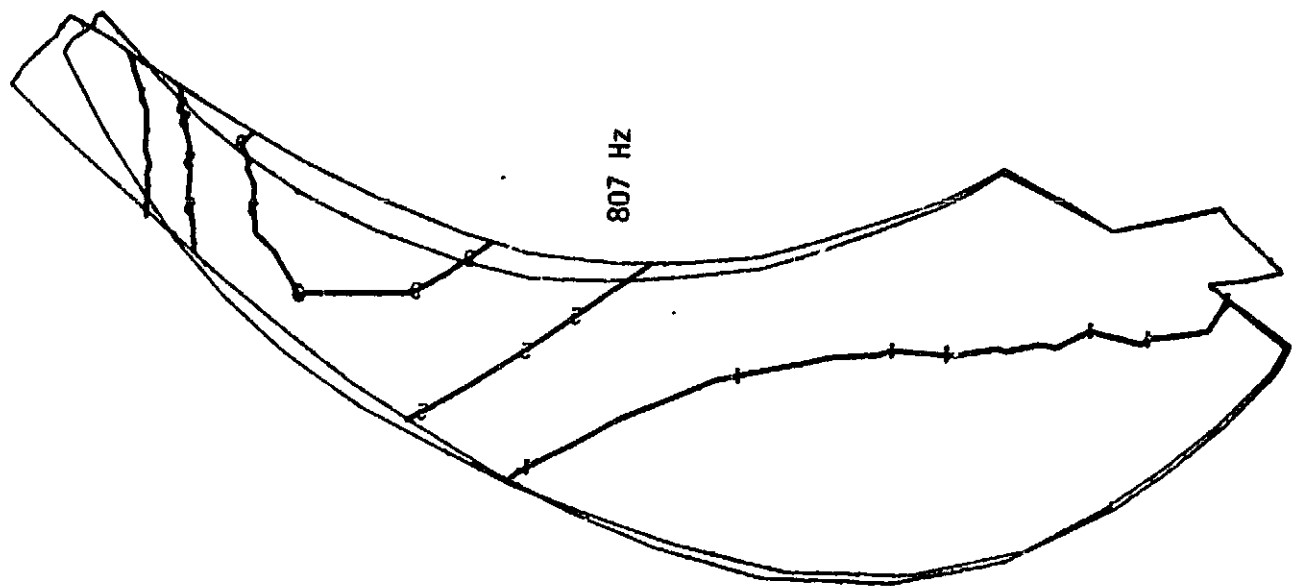


Figure 14. SR-5 Mode Shape, 0 rpm, Mode 5

ONIONSKY PAGE IS
OF POOR QUALITY

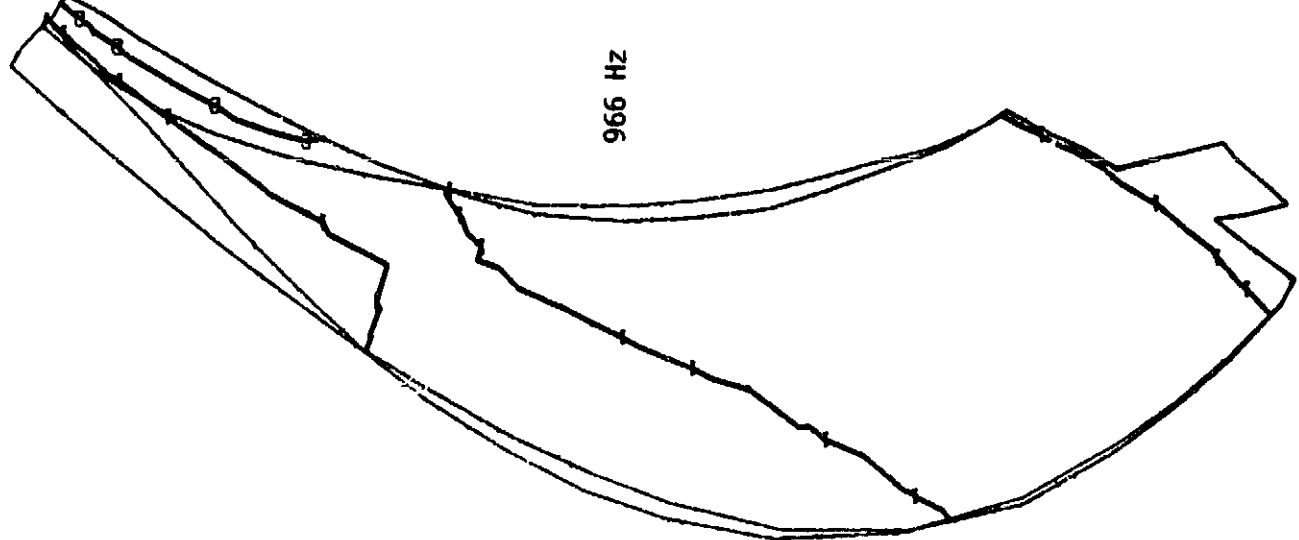
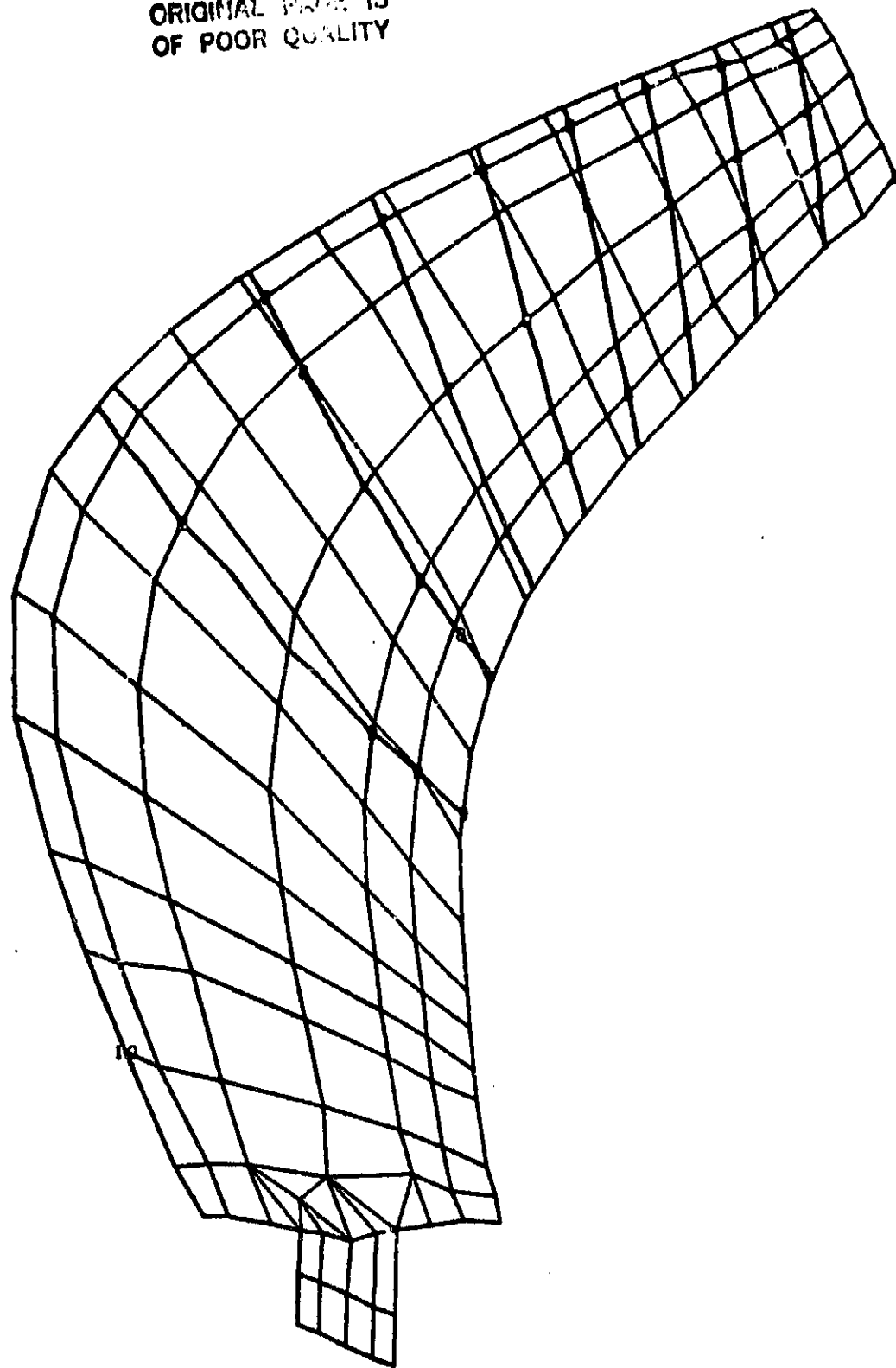


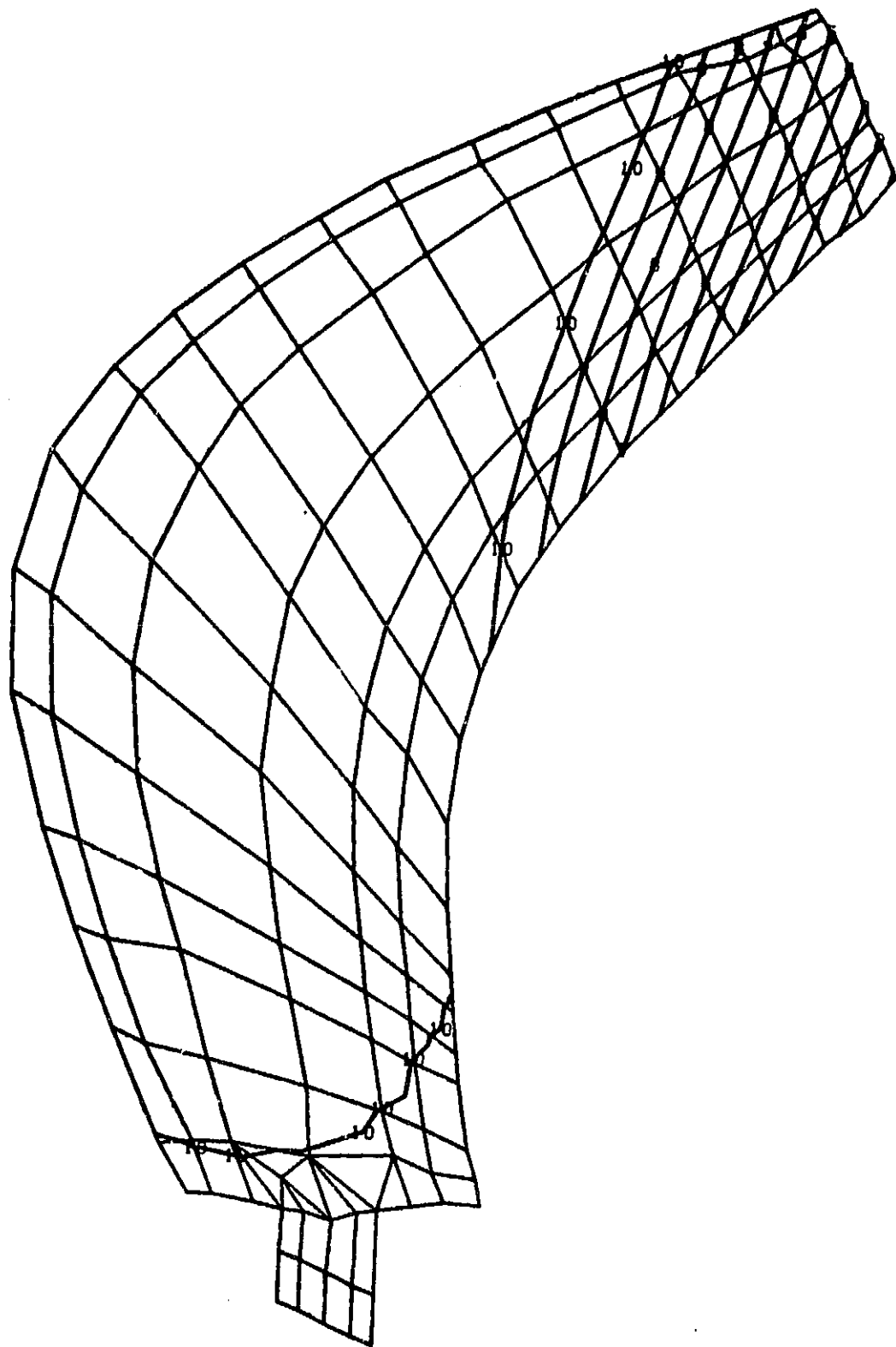
Figure 15. SR-5 Mode Shape, 0 rpm, Mode 6

ORIGINAL PAGE IS
OF POOR QUALITY



SAS ADVANCED TURBOPROP
DEFORMED MODEL AT 6800 RPM, CASE 3
SOL 9 AERO, EXIT AFTER K=0 MODES
MODAL DEFOR. SUBCASE 1 MODE 1 FREQ. 187.9298 Figure 16.

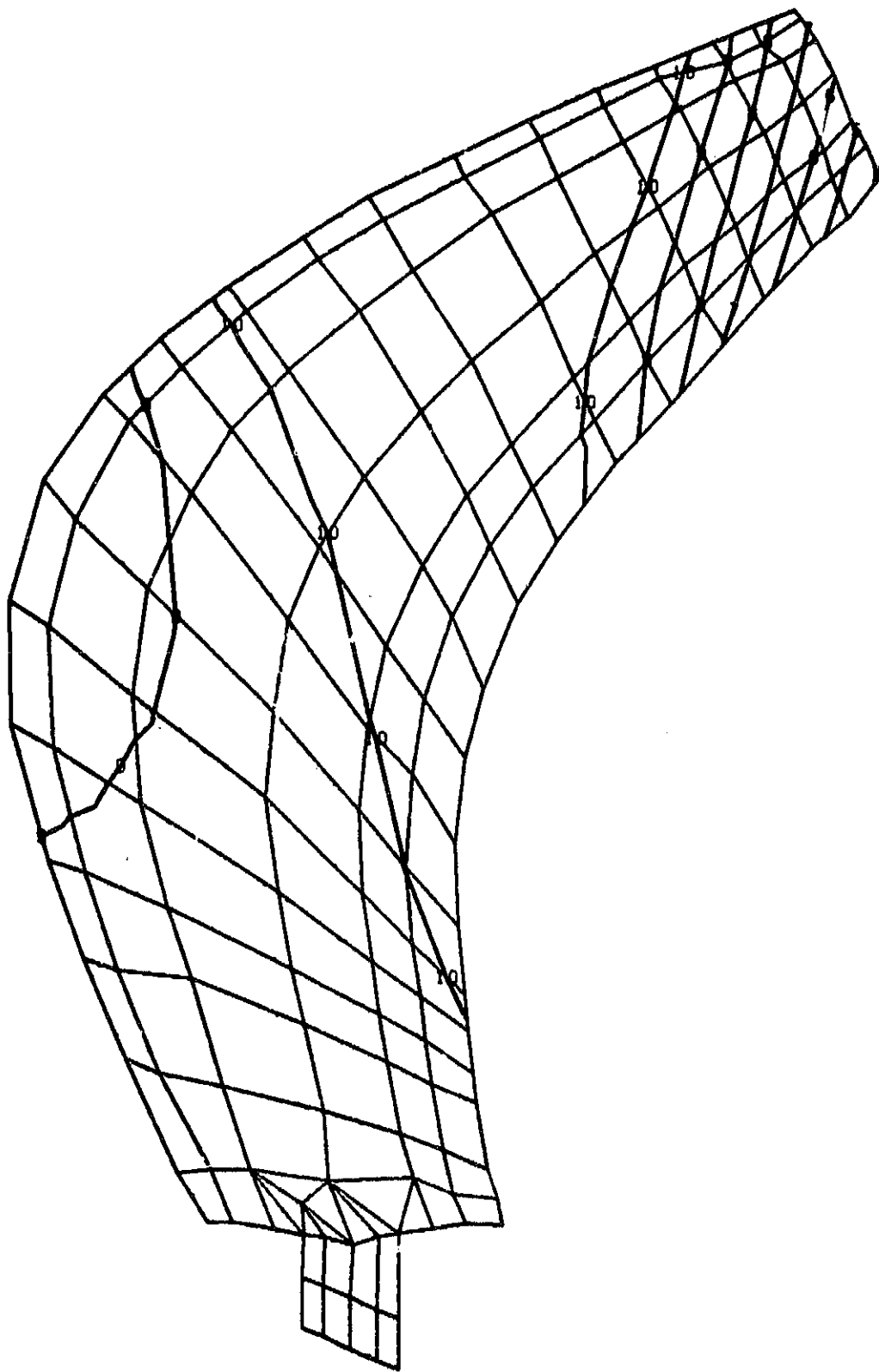
ORIGINAL PAGE IV
OF POOR QUALITY



SRS ADVANCED TURBOPROP
DEFORMED MODEL AT 6000 RPM, CASE 3
SOL 9 AERO, EXIT AFTER K=0 MODES
MODAL DEFOR. SUBCASE 1 MODE 2 FREQ. 292.8112

Figure 17.

ORIGINAL PAGE IS
OF POOR QUALITY

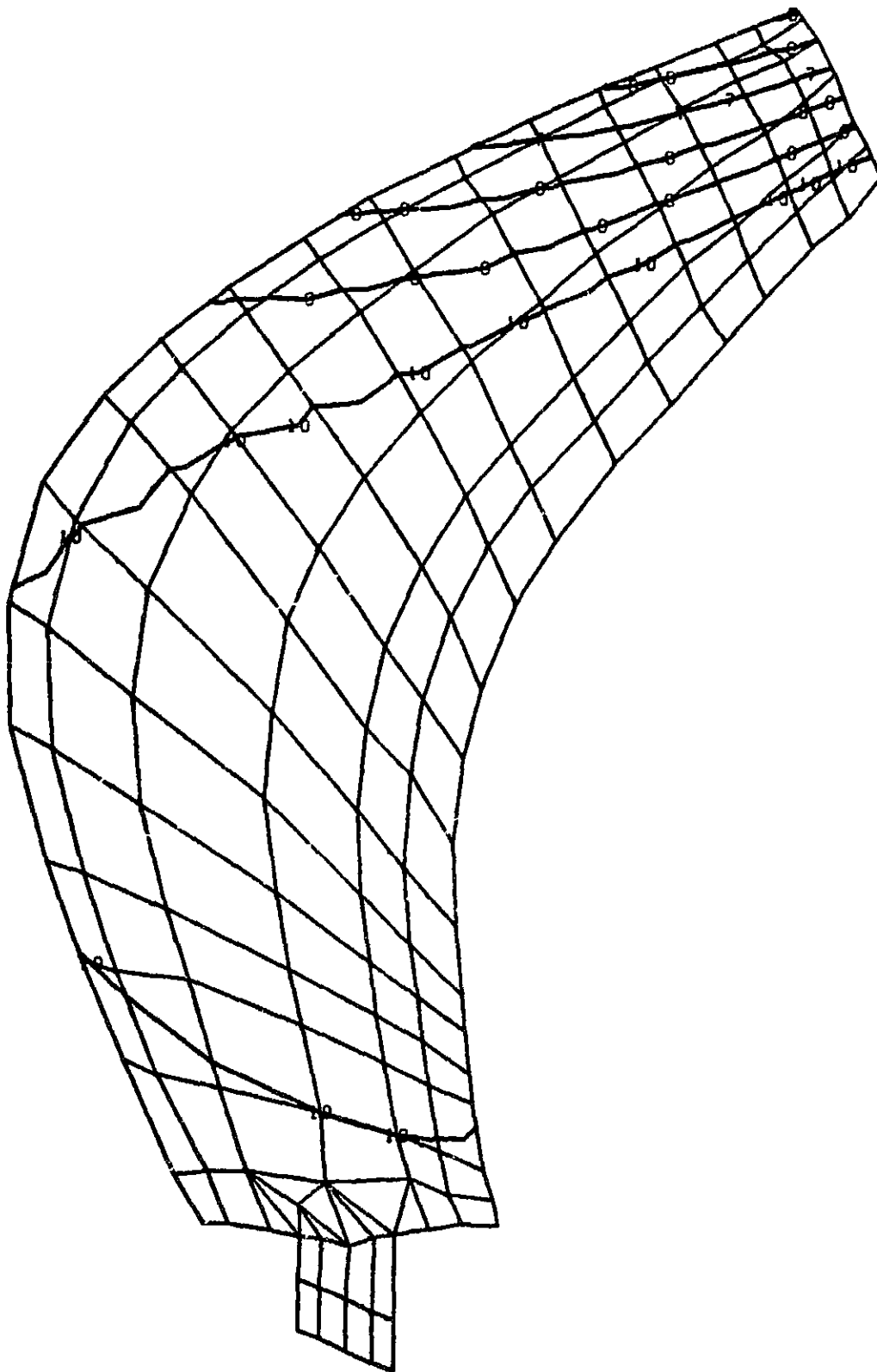


SRS ADVANCED TURBOPROP
DEFORMED MODEL AT 6800 RPM, CASE 3
SOL 9 AERO, EXIT AFTER K=0 MODES
MODAL DEFOR. SUBCASE 1 MODE 3 FREQ. 612.6408

SOL 9 AERO

Figure 18.

ORIGINAL PAGE IS
OF POOR QUALITY

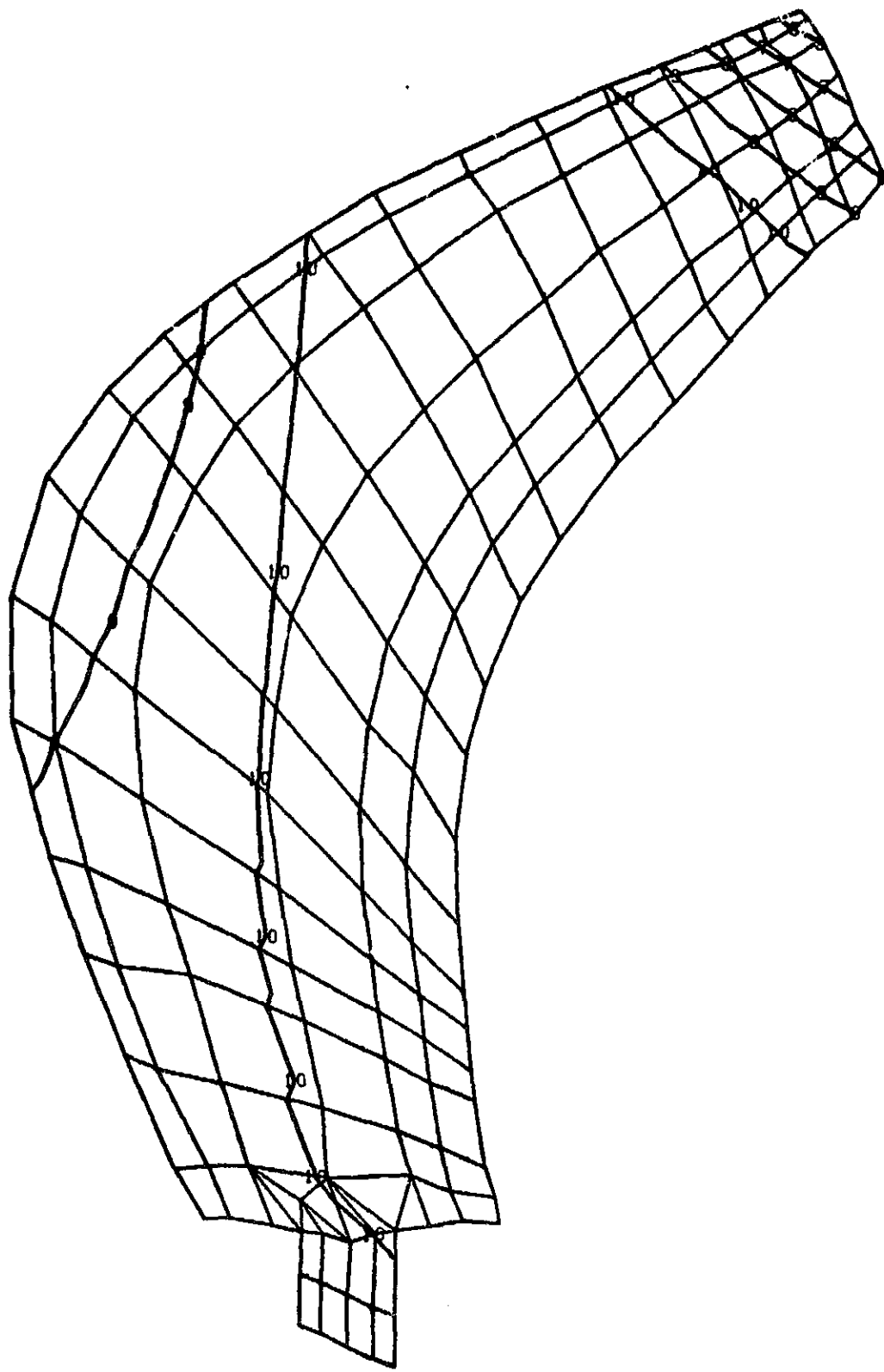


SRS ADVANCED TURBOPROP
DEFORMED MODEL AT 6800 RPM, CASE 3
SOL 8 AERO, EXIT AFTER K=0 MODES
MODAL DEFOR. SUBCASE 1 MODE 4 FREQ. 666.9909

SOL 8 AERO

Figure 19.

ORIGINAL PAGE IS
OF POOR QUALITY

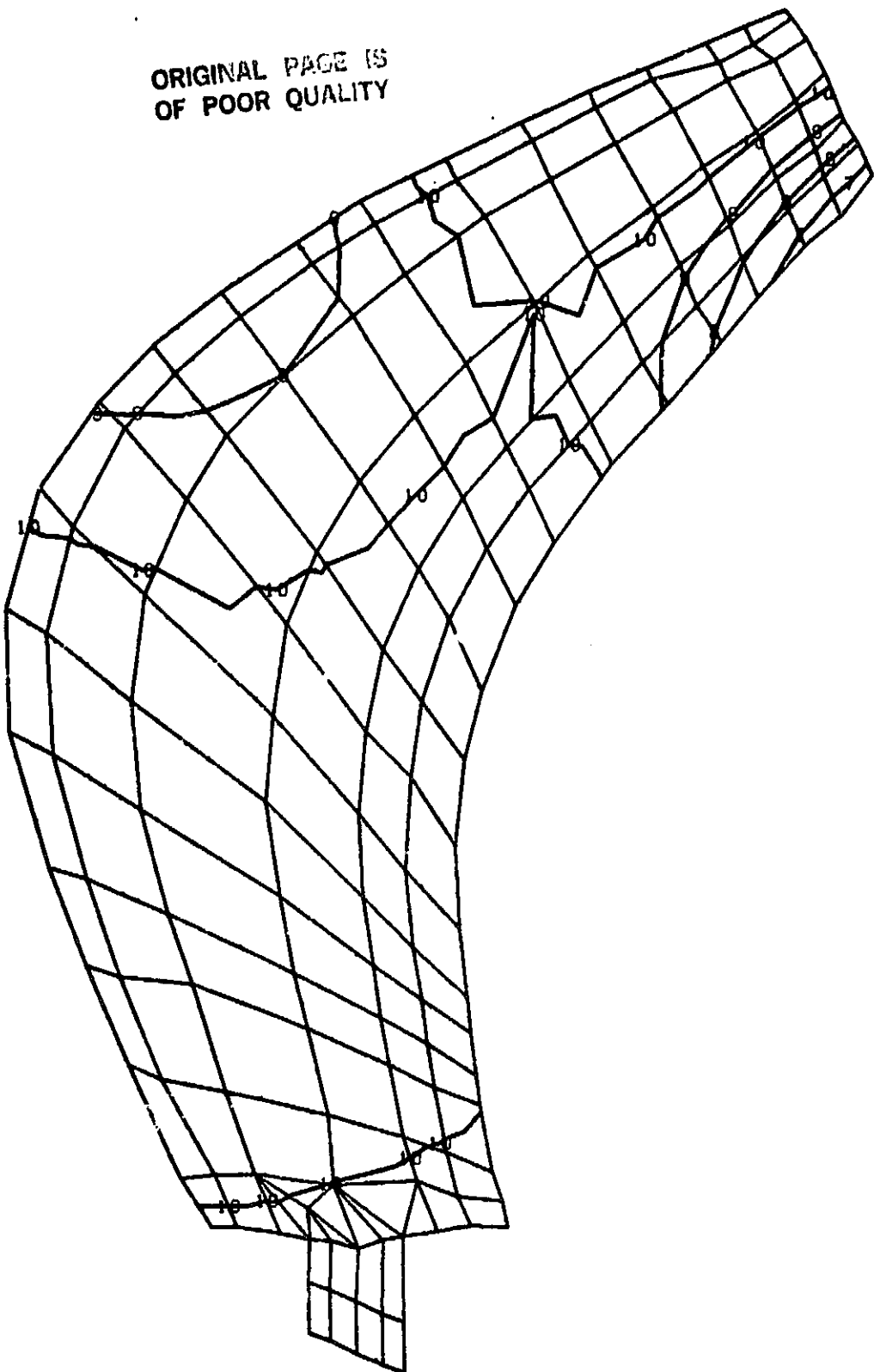


SRS ADVANCED TURBOPROP
DEFORMED MODEL AT 6800 RPM, CASE 3
SOL 9 AERO, EXIT AFTER K=0 MODES
MODAL DEFOR. SUBCASE 1 MODE 5 FREQ. 822.2677

SOL 9 AERO

Figure 20.

ORIGINAL PAGE IS
OF POOR QUALITY



SRS ADVANCED TURBOPROP
DEFORMED MODEL AT 6800 RPM, CASE 3
SOL 9 AERO, EXIT AFTER K=0 MODES
MODAL DEFOR. SUBCASE 1 MODE 6 FREQ. 1008.467

SOL 9 AERO

Figure 21.

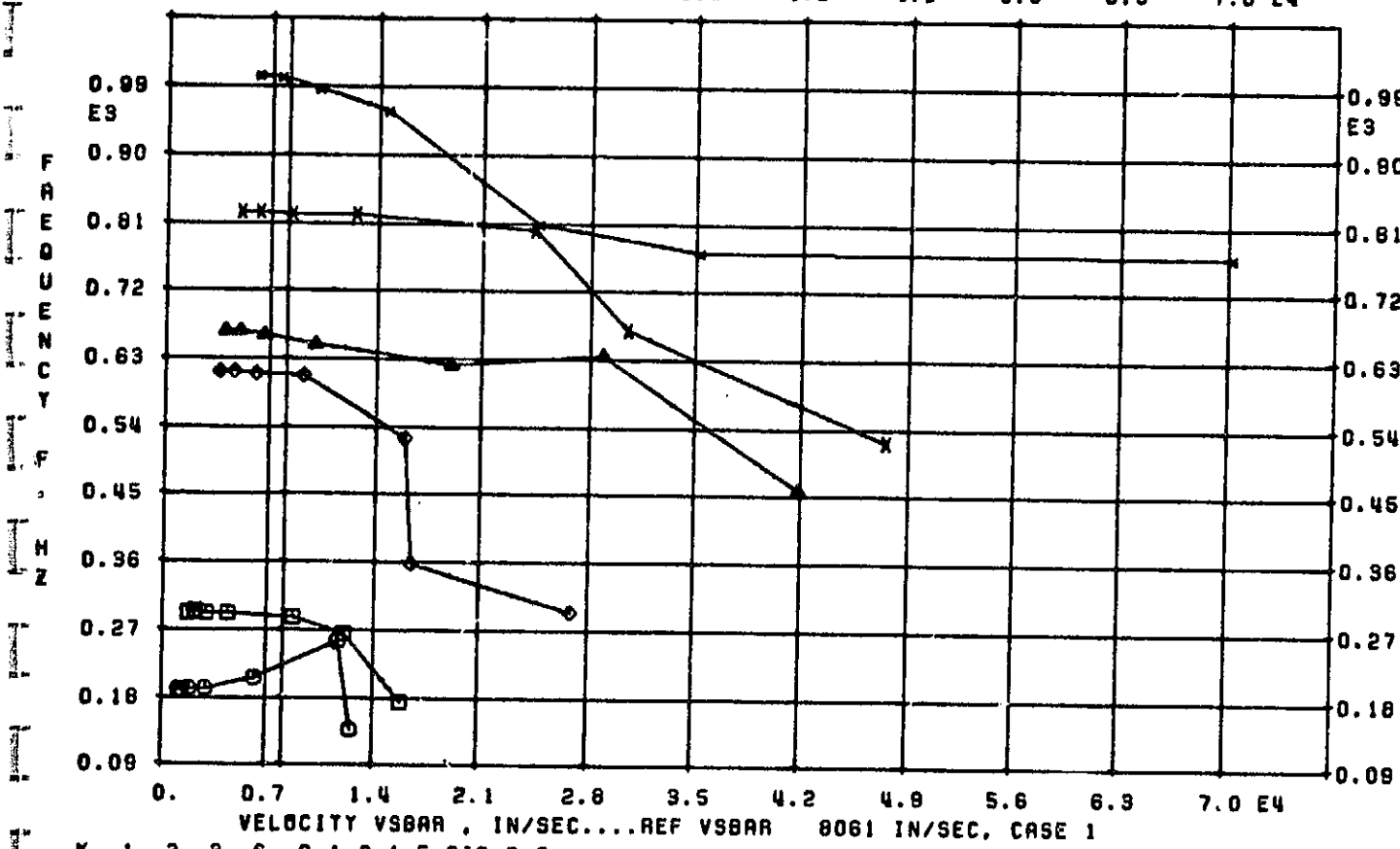
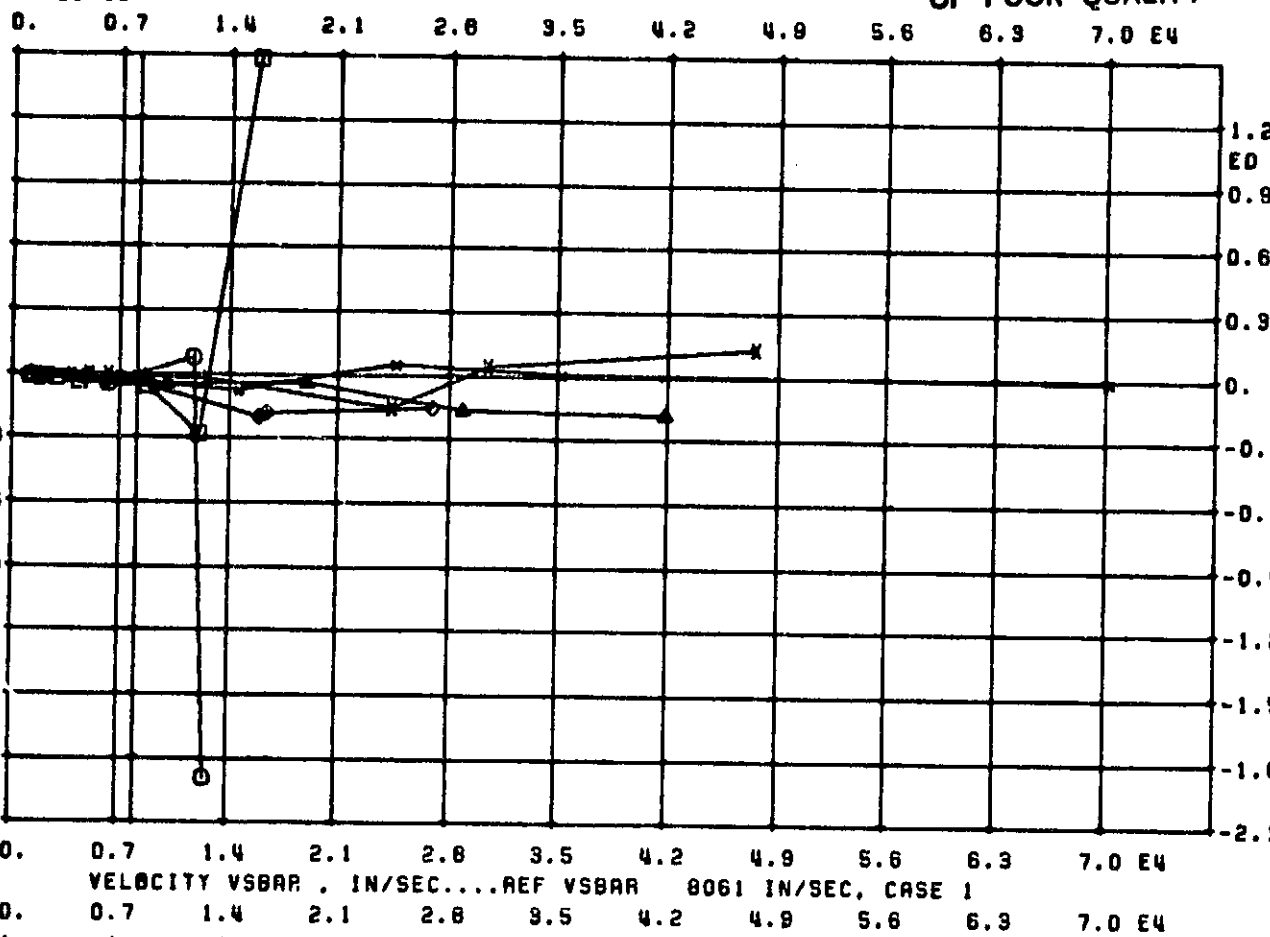
Table 6. CONTOUR VALUES FOR MODAL PLOTS
 (Figures 10-21)

Contour Symbol	Y-Displacement (Figures 10-15)	Y-Displacement (Figures 16-21)
1	-0.003	-1.0
2	0.11	-0.9
3	0.22	-0.78
4	0.33	-0.67
5	0.44	-0.56
6	0.55	-0.44
7	0.67	-0.33
8	0.78	-0.22
9	0.89	-0.10
10	1.0	+0.005

Notes:

1. For Figures 10 through 21 :
 - a) Contours are plotted on the undeformed shape.
 - b) Y axis is normal to the axis of rotation, and approximately normal to the blade mean surface.
2. For Figures 10 through 15 :
 - a) Outline of the deformed shape is also shown.
 - b) Contour with symbol '1' approximately represents a nodal line.
3. For Figures 16 through 21 :
 - a) Contour with symbol '10' approximately represents a nodal line.

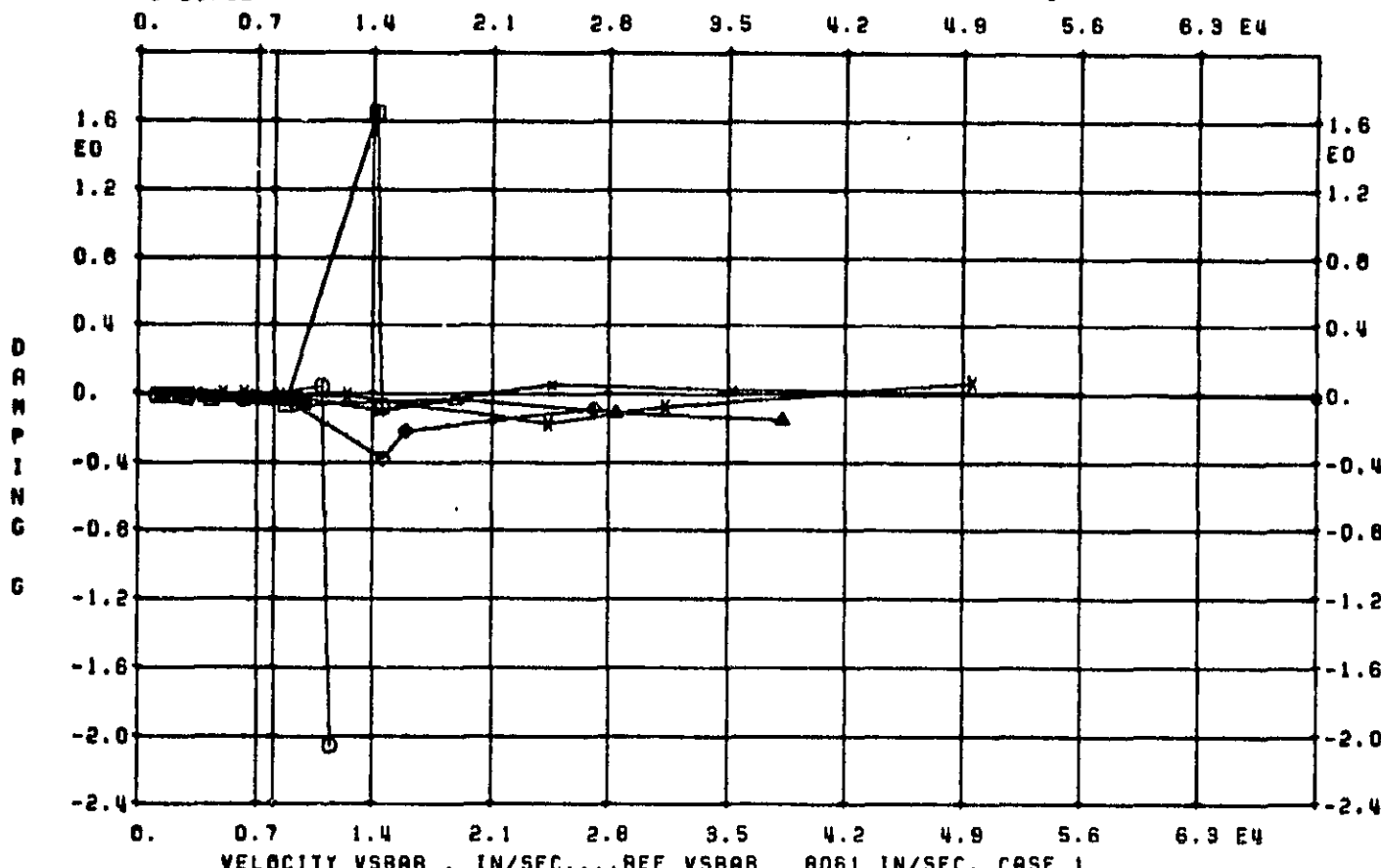
3/26/82



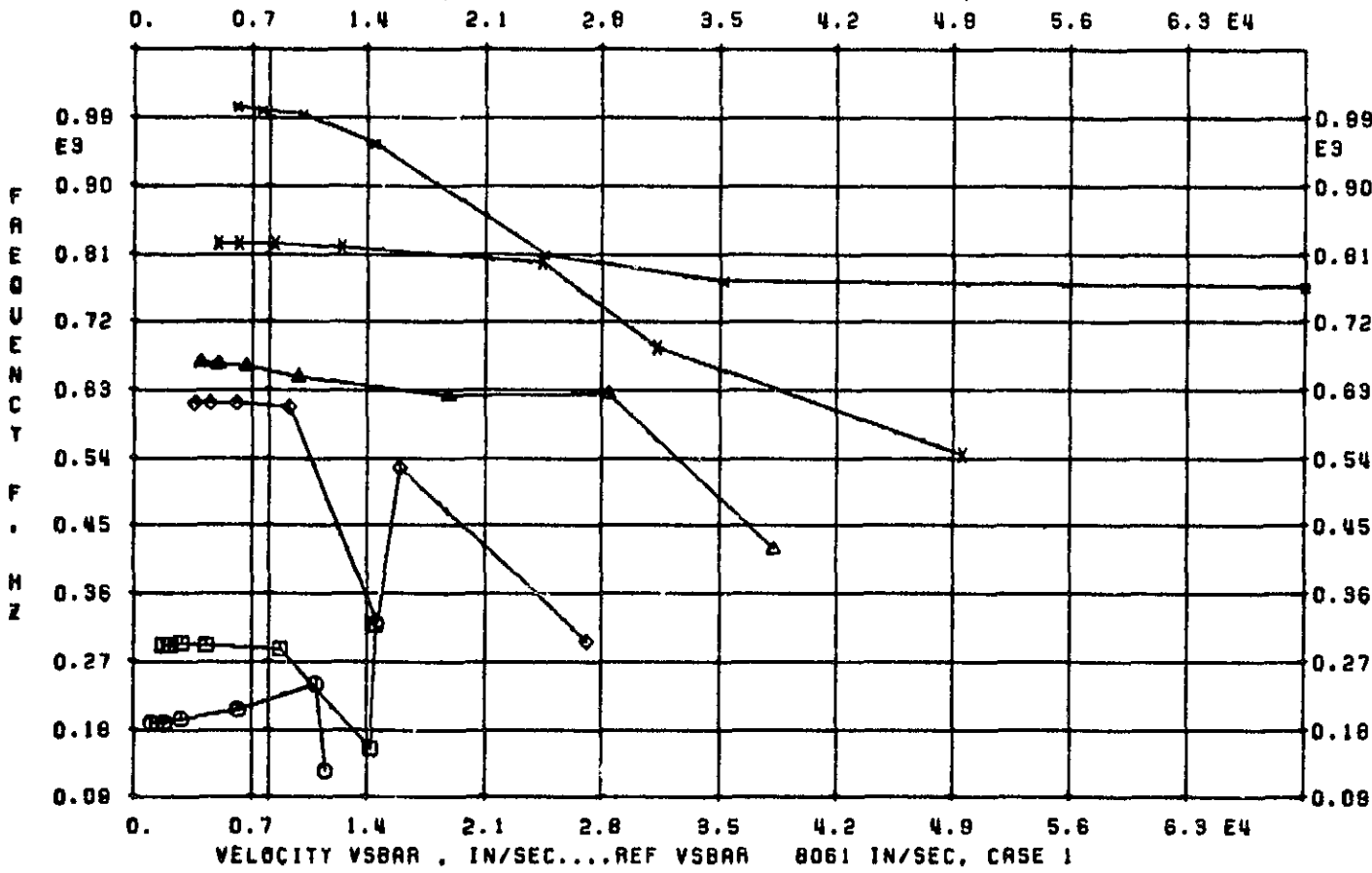
K .1..2,.9..6,.8.1.2,1.5,SIG 0.0
SOL 8 AERO,K 0 MODES AND FLUTTER

Figure 22. V-g, V-f Curves, Case 1

9/26/82



VELOCITY VSBAR , IN/SEC....REF VSBAR 8061 IN/SEC, CASE 1



VELOCITY VSBAR , IN/SEC....REF VSBAR 8061 IN/SEC, CASE 1

K .1..2..3..6..9..1..2..1..5..SIG 72.0
SOL 9 AERO,K 0 MODES AND FLUTTER

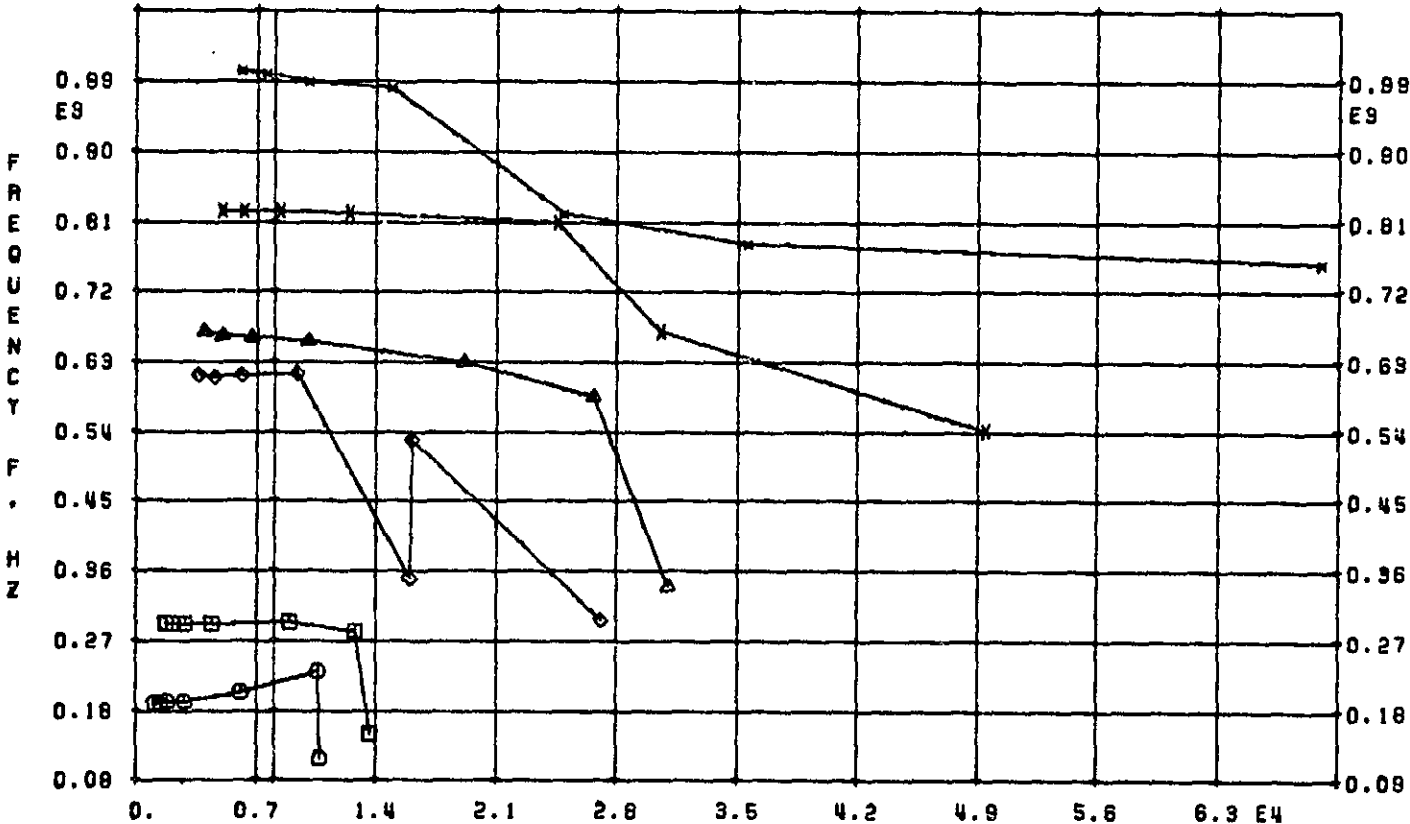
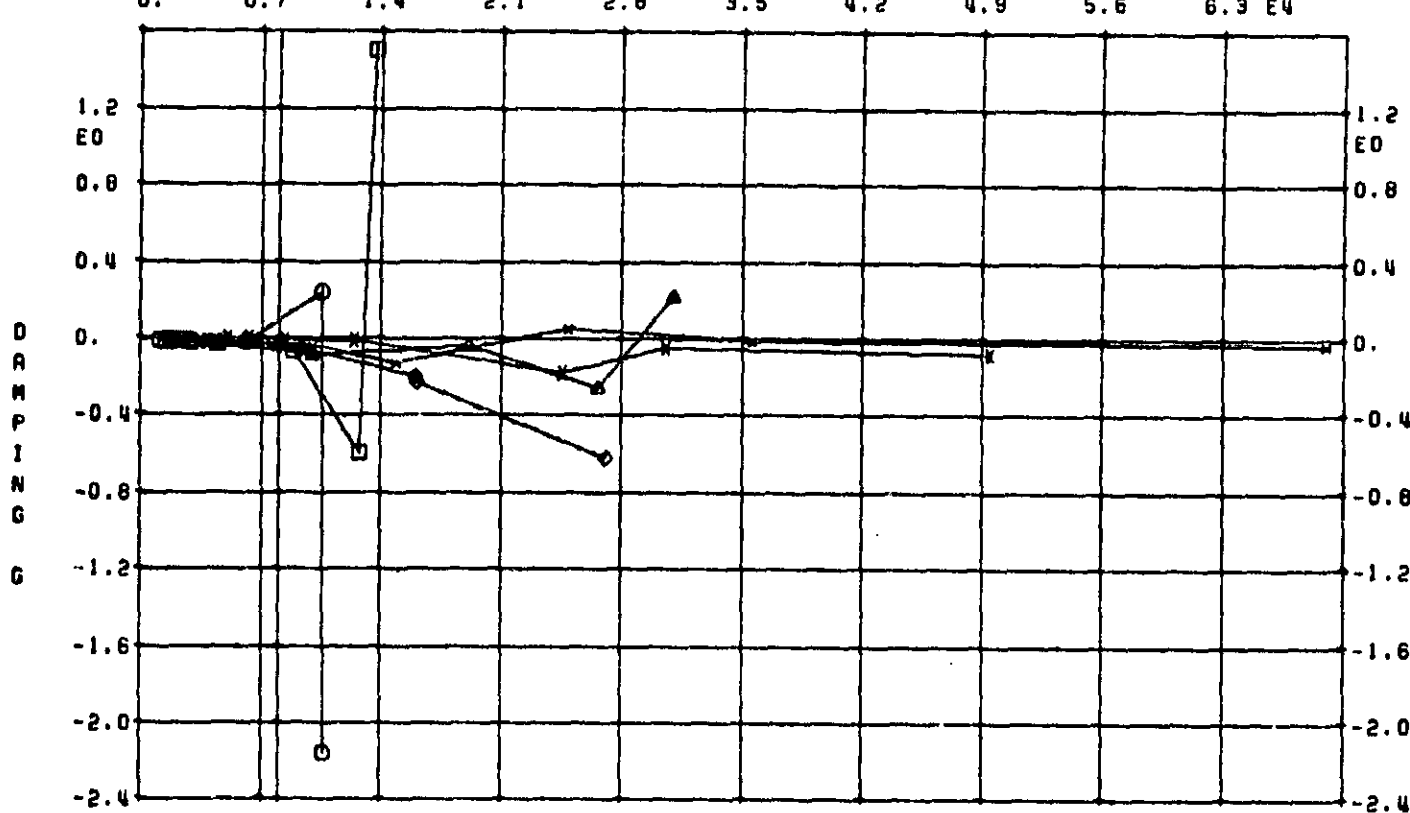
Figure 23. V-g, V-f Curves, Case 1

ORIGINAL PAGE IS
OF POOR QUALITY

9

3

3/26/82



K .1..2..3..6..8.1.2.1.5.SIG 144.0
SOL 9 AERO,K 0 MODES AND FLUTTER

Figure 24. V-g, V-f Curves, Case 1

ORIGINAL PAGE IS
OF POOR QUALITY
8/26/82

ORIGINAL PAGE IS
OF POOR QUALITY

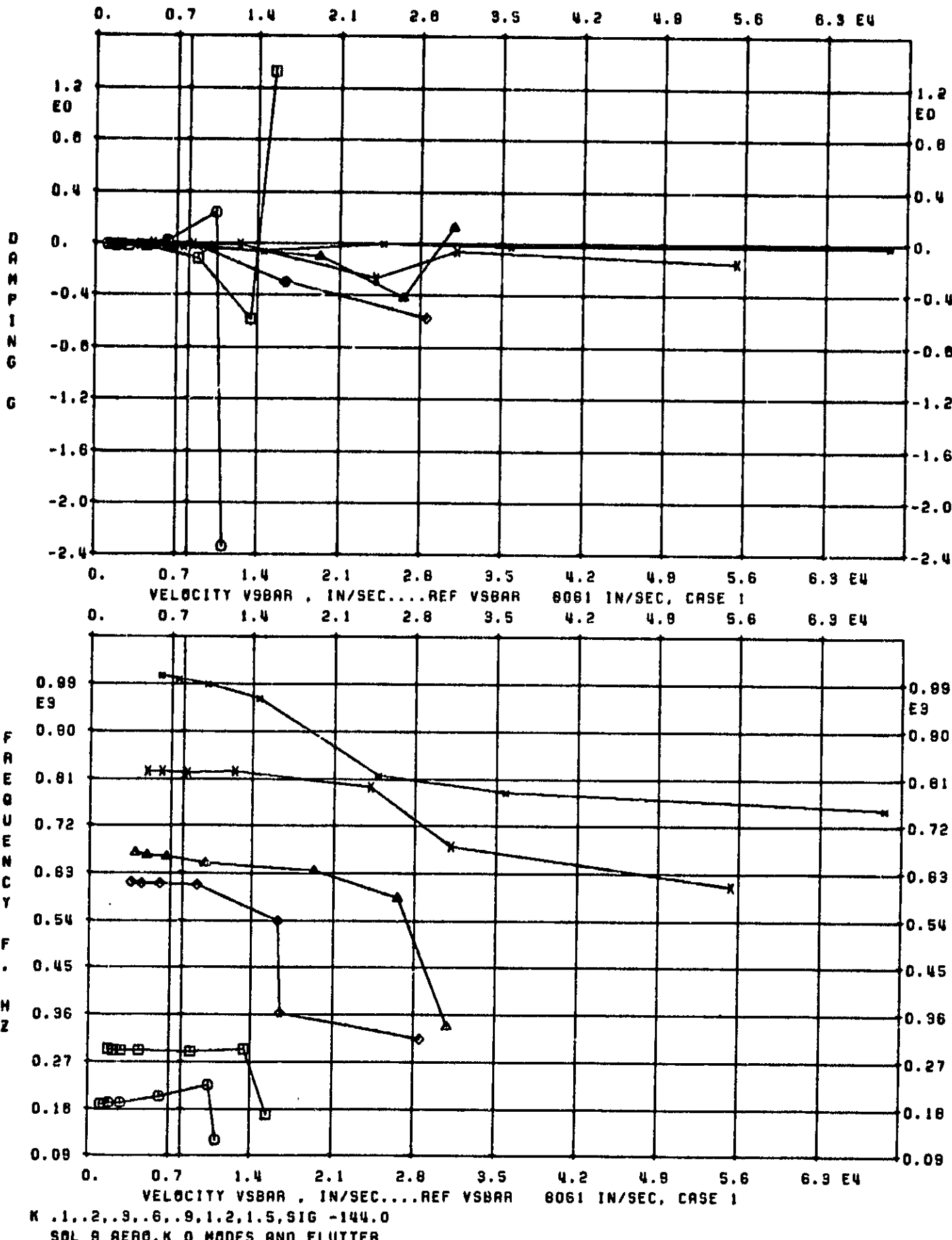
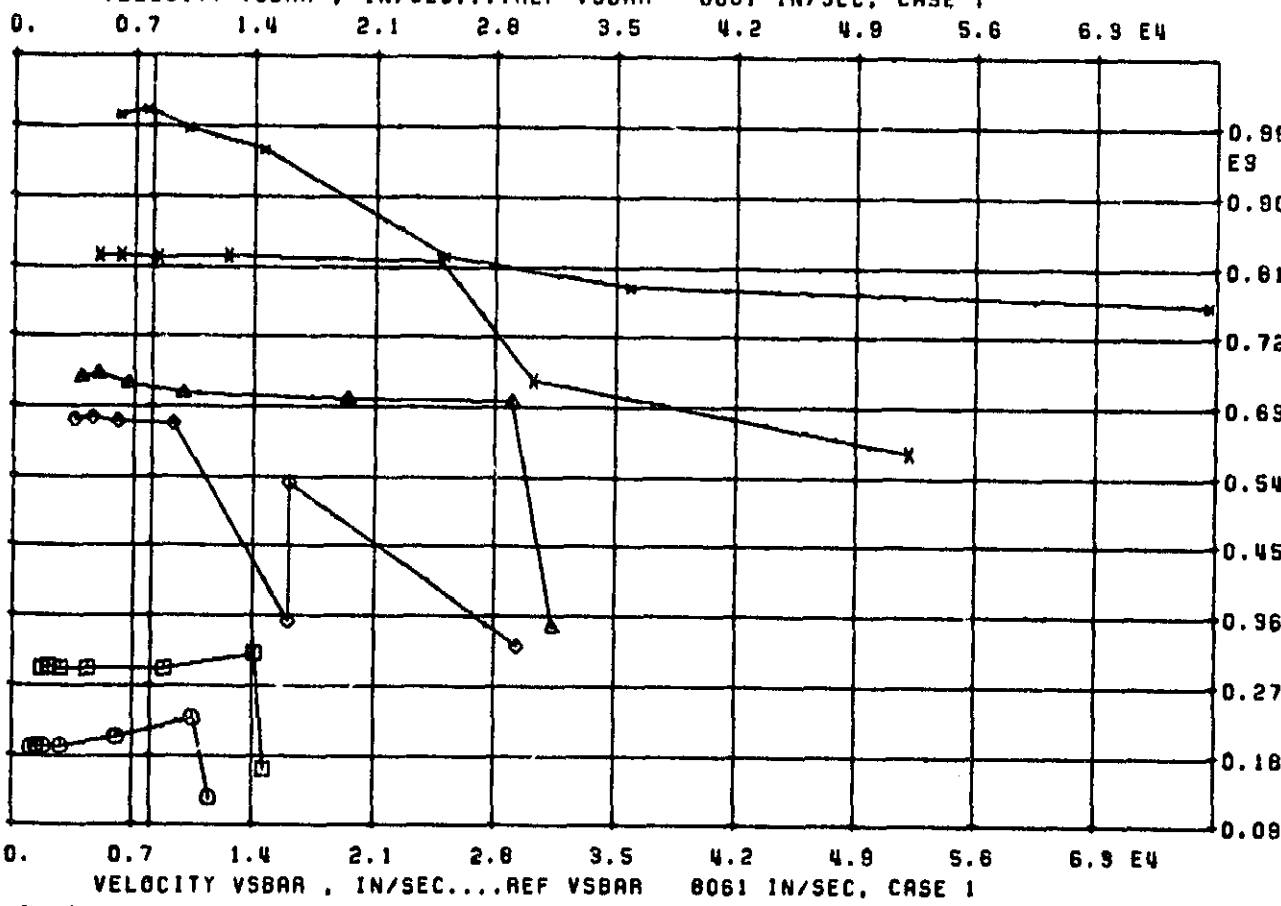
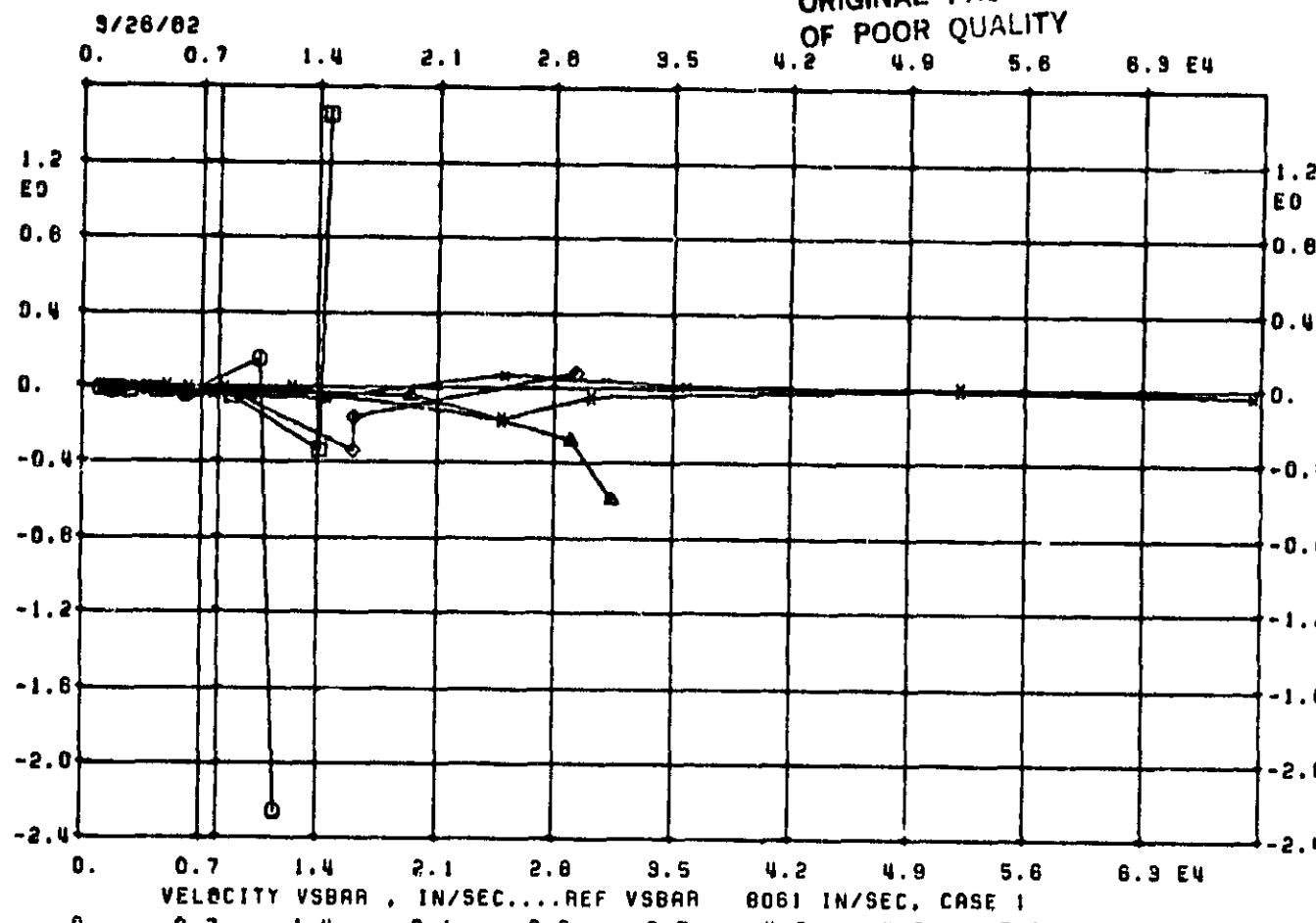


Figure 25. V-g, V-f Curves, Case 1



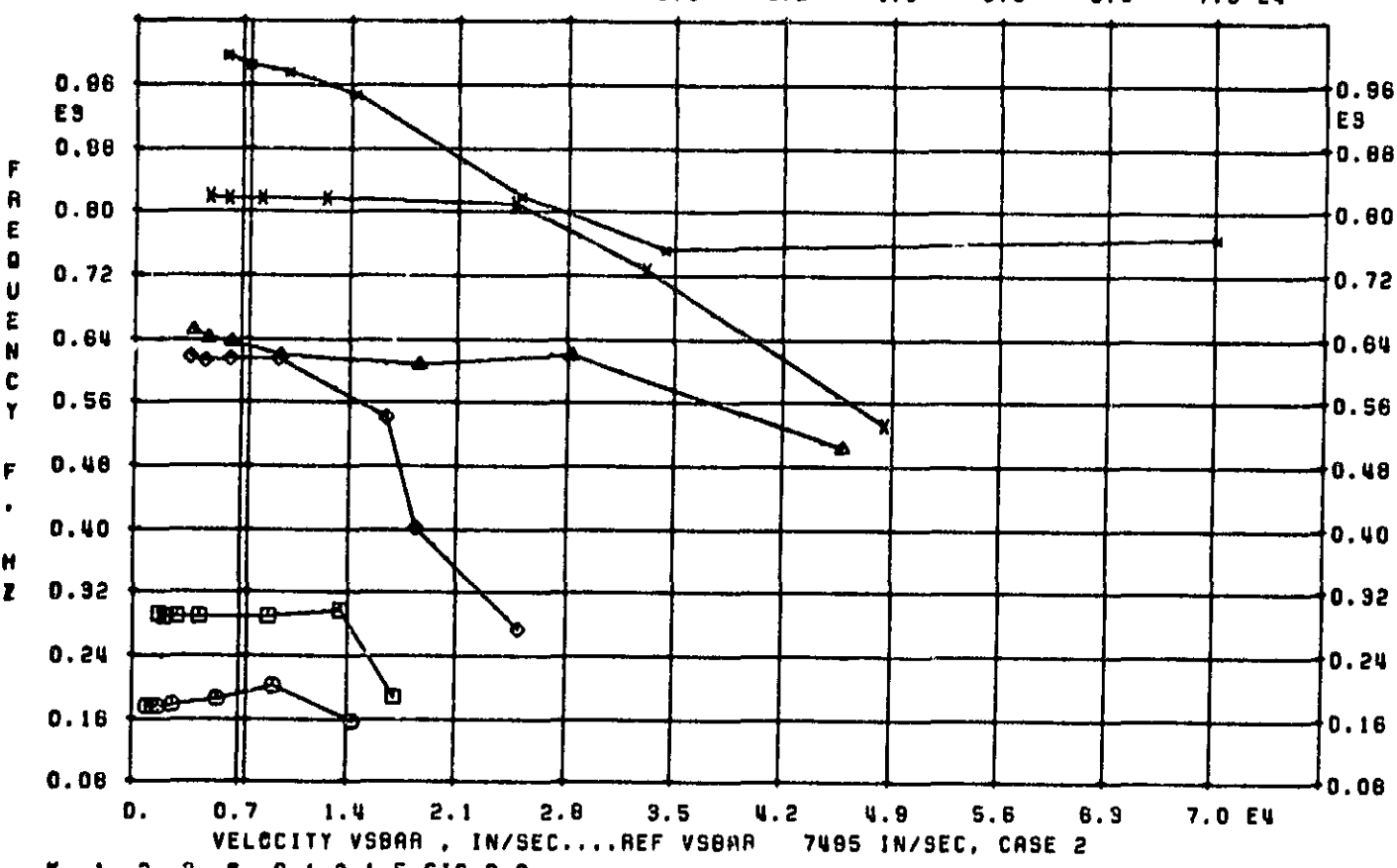
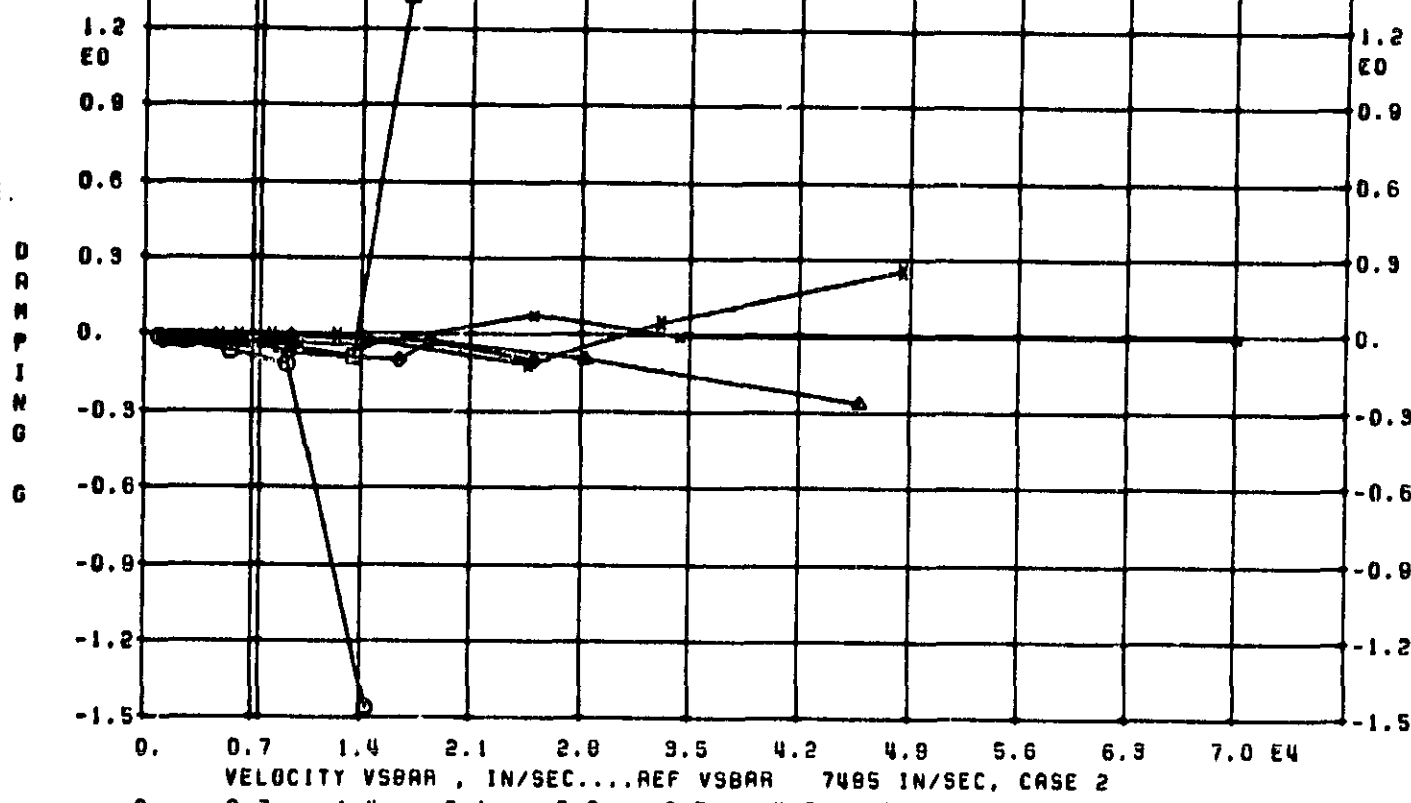
K .1,.2,.3,.6,.9,1.2,1.5,SIG -72.0
SOL 9 AERO,K 0 MODES AND FLUTTER

Figure 26. V-g, V-f Curves, Case 1

ORIGINAL PAGE IS
OF POOR QUALITY

8/26/62

0. 0.7 1.4 2.1 2.8 3.5 4.2 4.9 5.6 6.3 7.0 E4



K .1,.2,.3,.6,.9,1.2,1.5,SIG 0.0
SOL 8 AERO,K 0 MODES AND FLUTTER

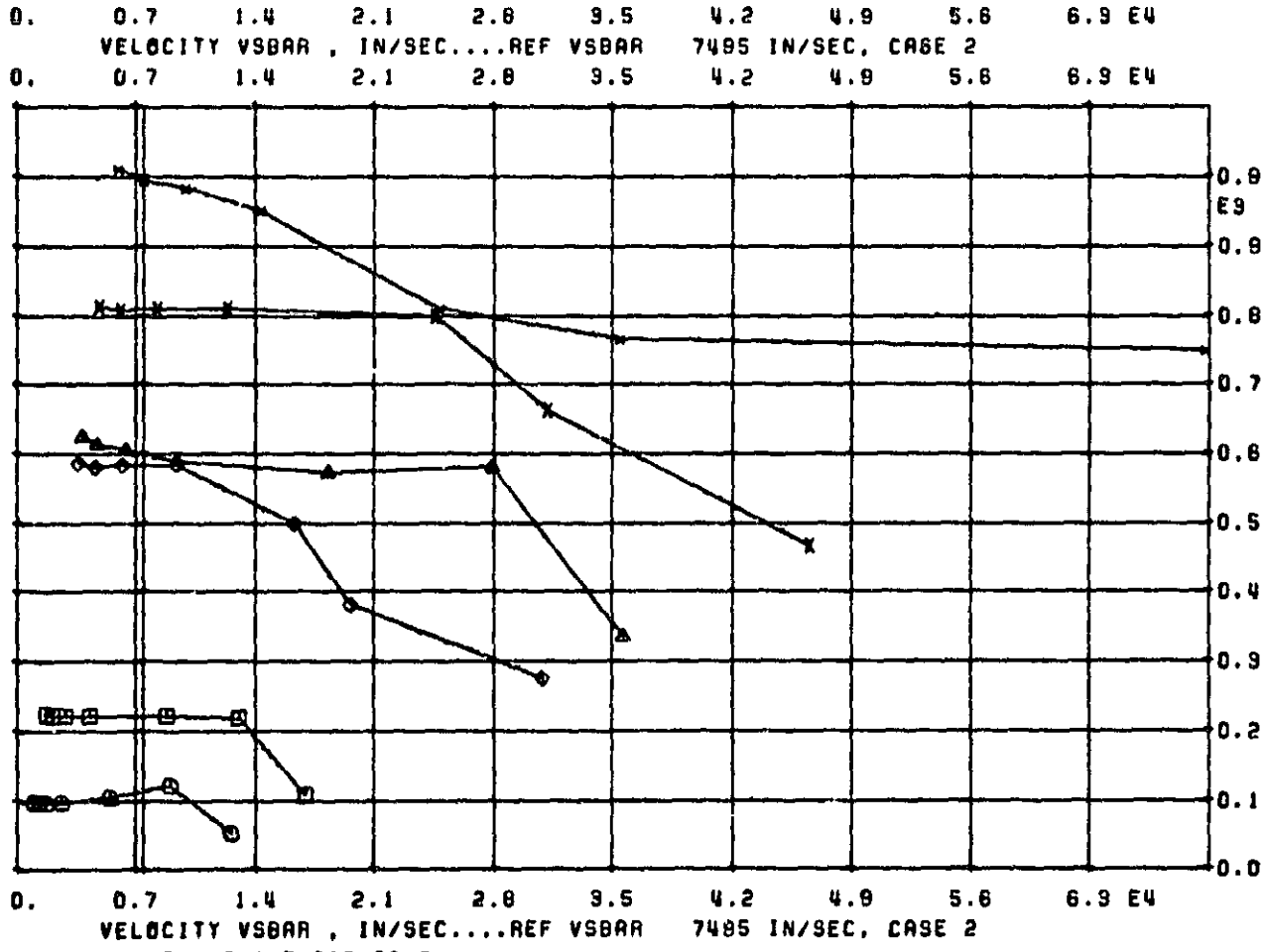
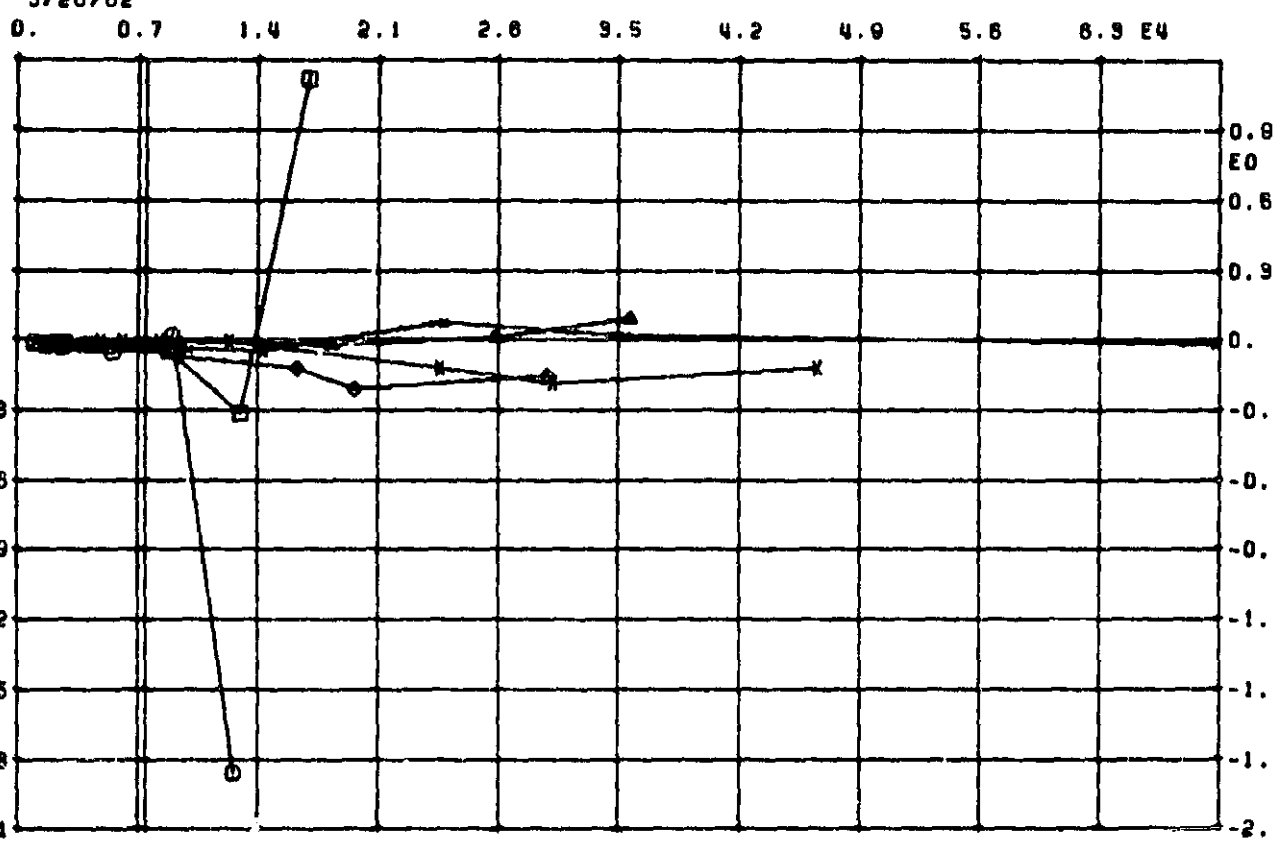
Figure 27. V-g, V-f Curves, Case 2

ORIGINAL PAGE IS
OF POOR QUALITY

2

9/26/82

2



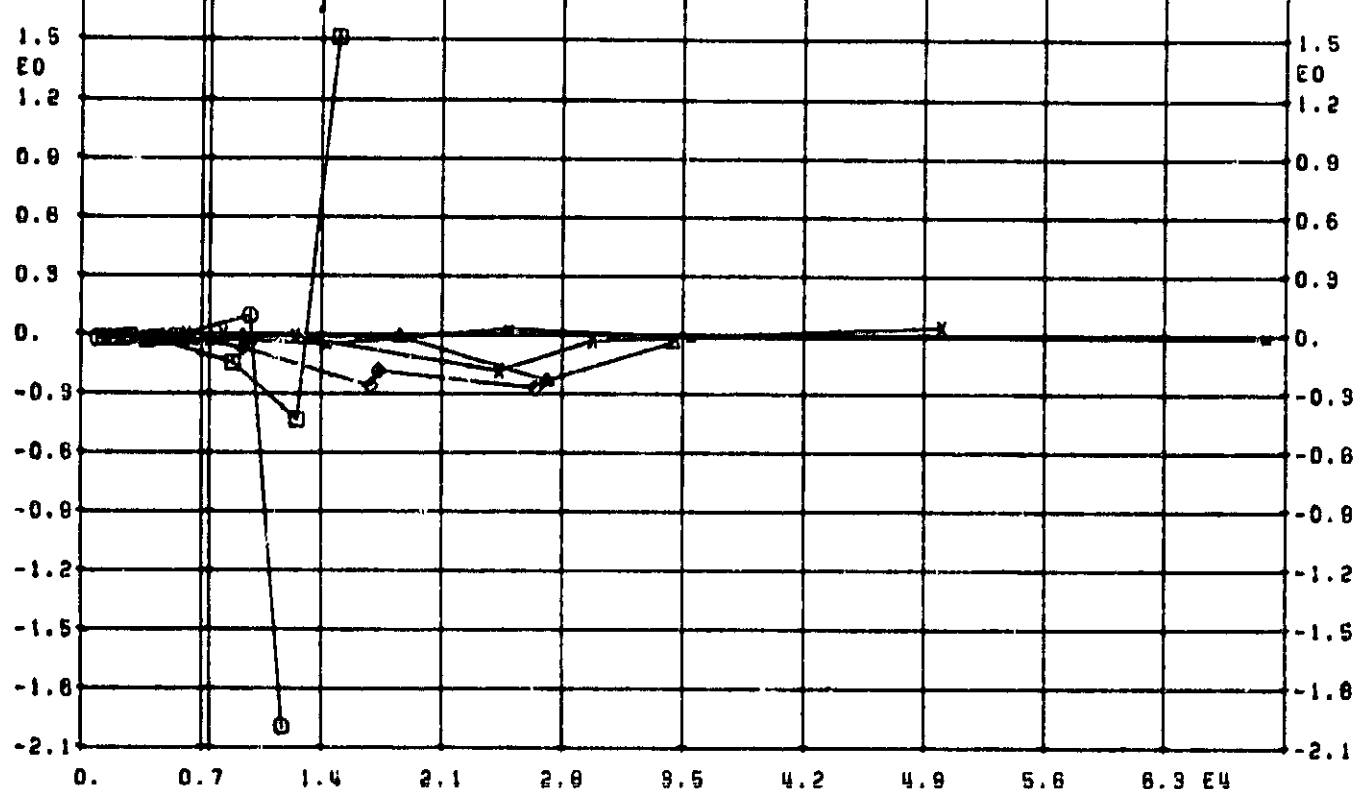
K .1..2..9..6..9..1..2..1..5..SIG 96.0
SOL 9 AERO,K 0 MODES AND FLUTTER

Figure 28. V-g, V-f Curves, Case 2

9/26/82

0. 0.7 1.4 2.1 2.8 3.5 4.2 4.9 5.6 6.3 E4

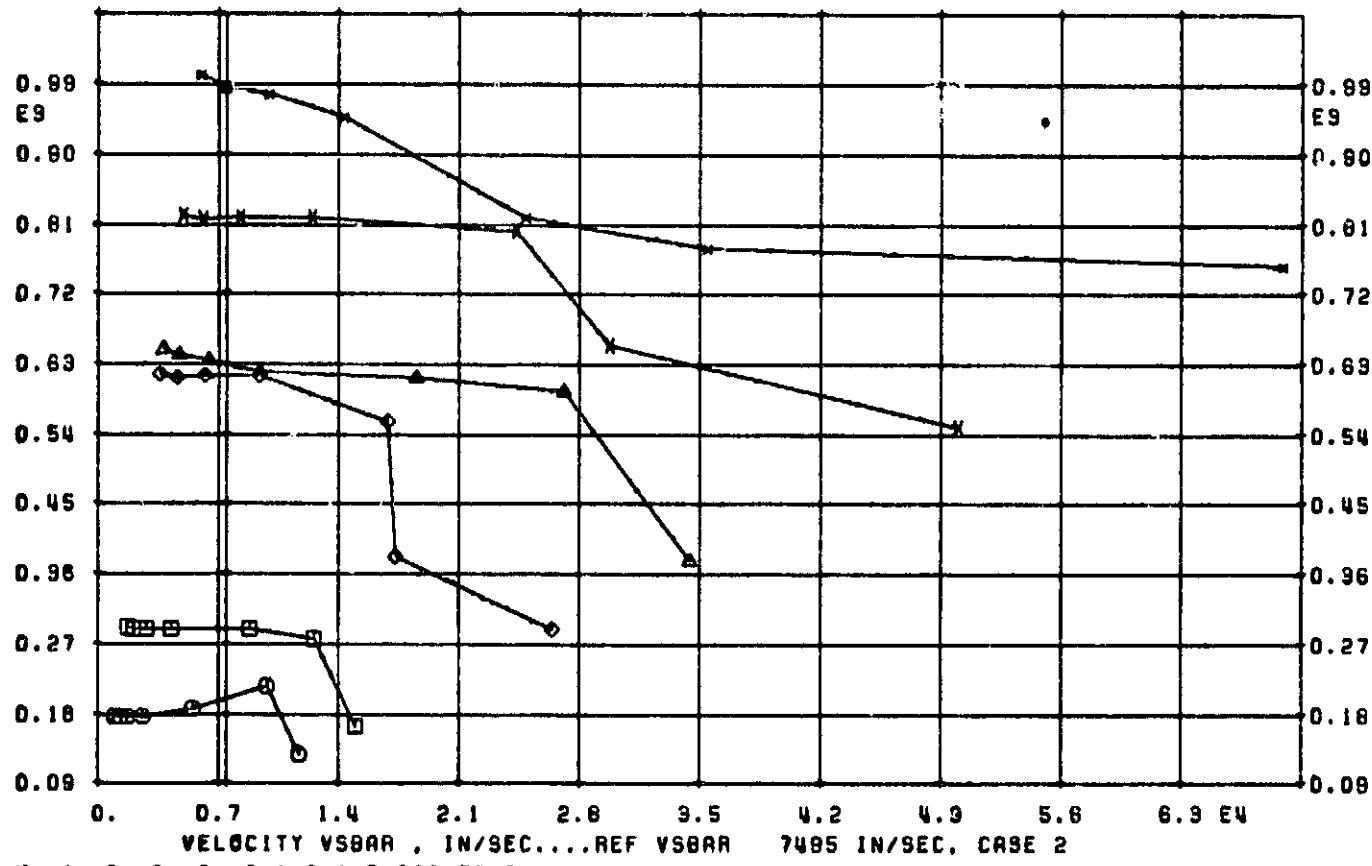
DAMPING



VELOCITY $V\bar{v}$, IN/SEC...REF $V\bar{v}$ 7485 IN/SEC, CASE 2

0. 0.7 1.4 2.1 2.8 3.5 4.2 4.9 5.6 6.3 E4

FREQUENCY F.



VELOCITY $V\bar{v}$, IN/SEC...REF $V\bar{v}$ 7485 IN/SEC, CASE 2

K .1..2..9..6..8.1.2.1.5.SIG 72.0
SOL 9 AERO,K 0 MODES AND FLUTTER

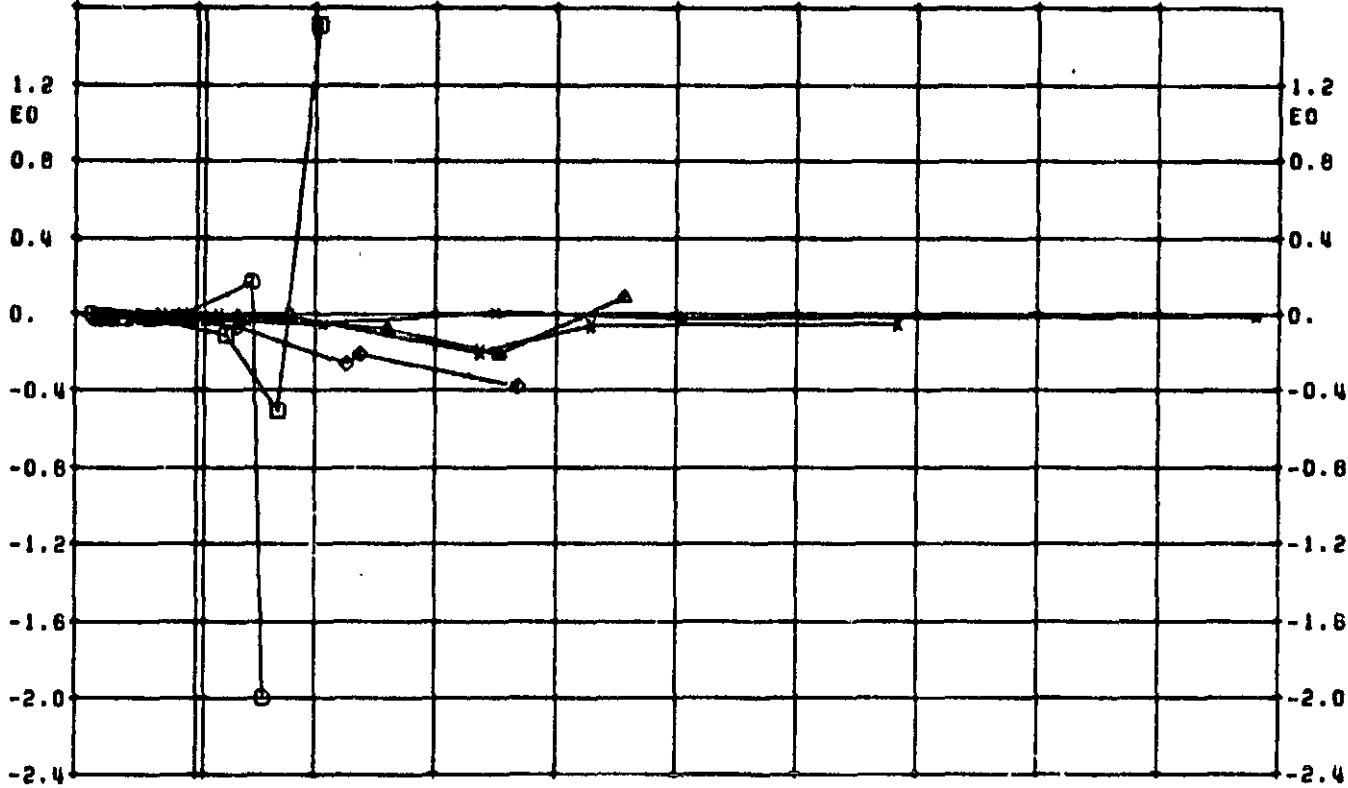
Figure 29. V-g, V-f Curves, Case 2

ORIGINAL PAGE IS
OF POOR QUALITY

3/26/62

0. 0.7 1.4 2.1 2.8 3.5 4.2 4.9 5.6 6.3 E4

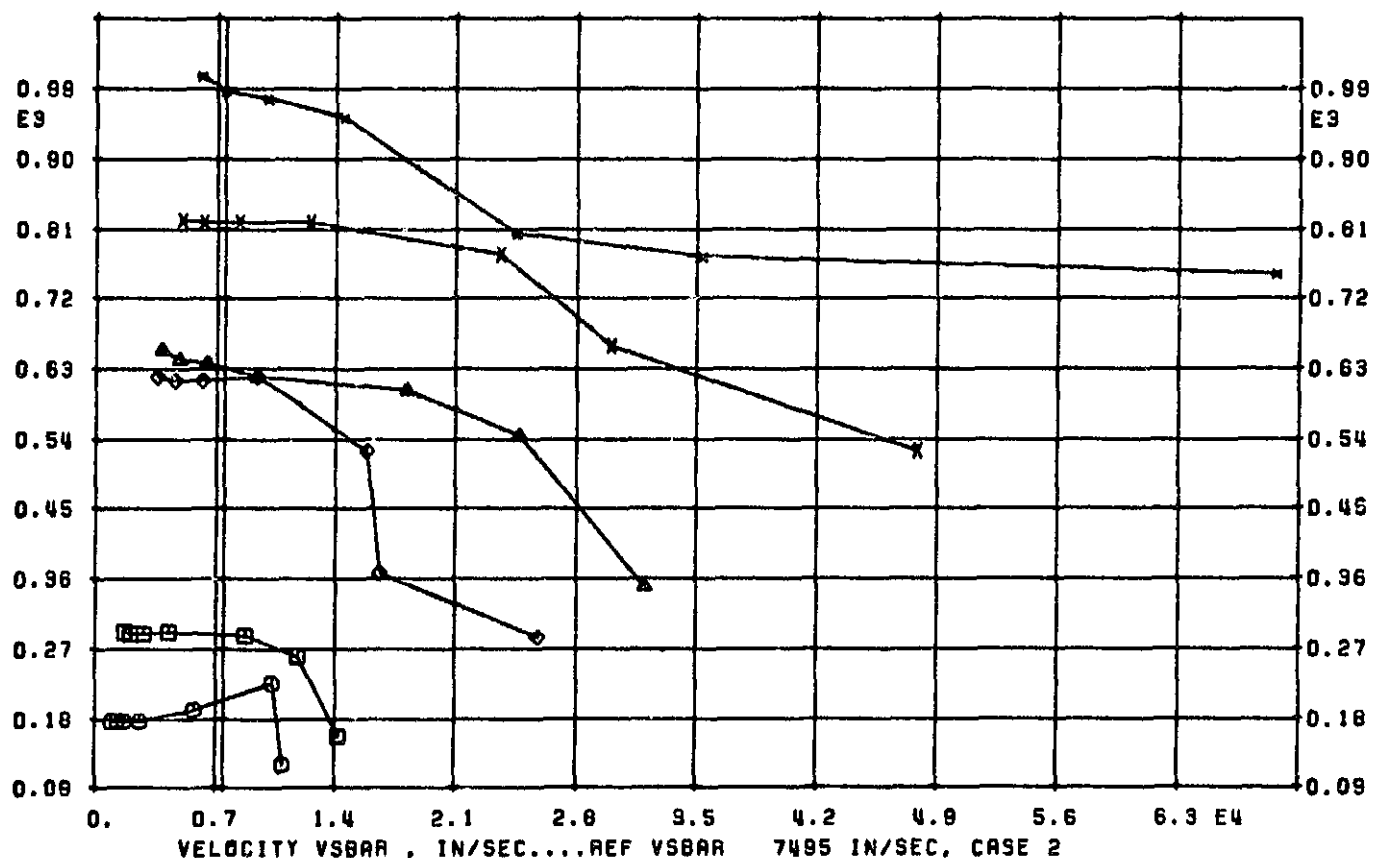
DAMPING



VELOCITY V_SBAR , IN/SEC....REF V_SBAR 7495 IN/SEC, CASE 2

0. 0.7 1.4 2.1 2.8 3.5 4.2 4.9 5.6 6.3 E4

FREQUENCY



VELOCITY V_SBAR , IN/SEC....REF V_SBAR 7495 IN/SEC, CASE 2

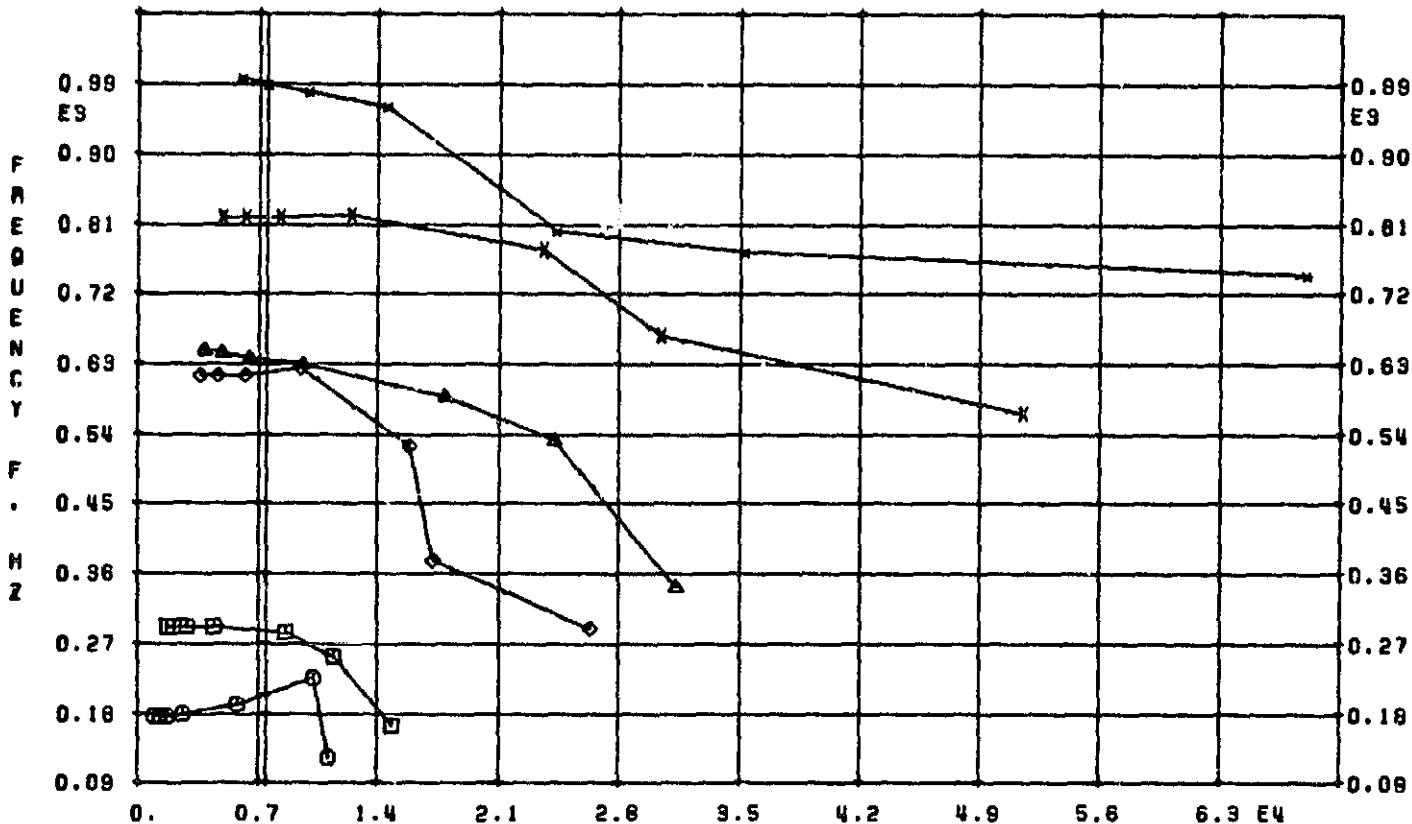
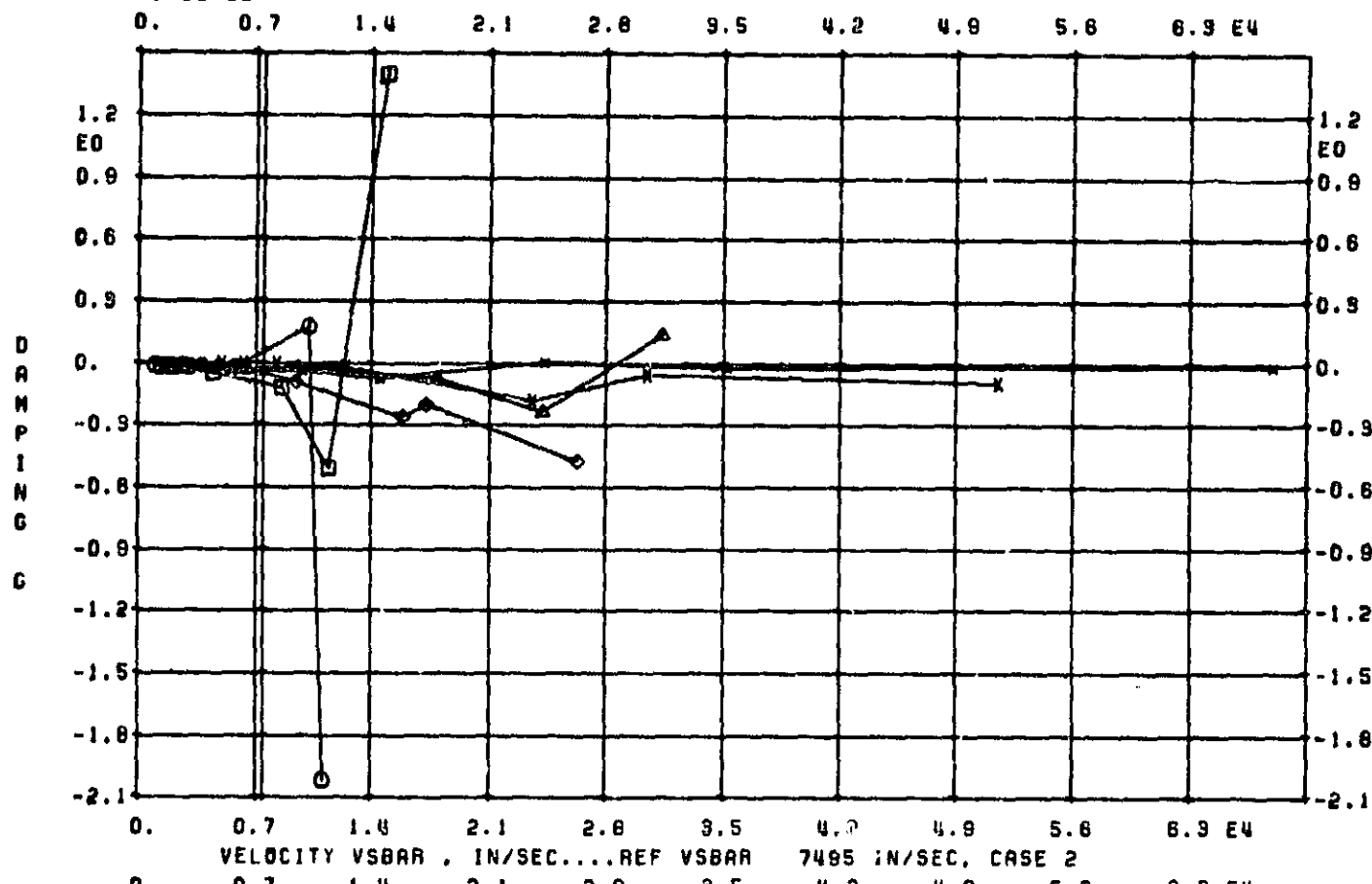
K .1,.2,.3,.6,.8.1.2.1.5,SIG 108.0
SOL 9 AERO,K 0 MODES AND FLUTTER

Figure 30. V-g, V-f Curves, Case 2

5

9/26/82

5



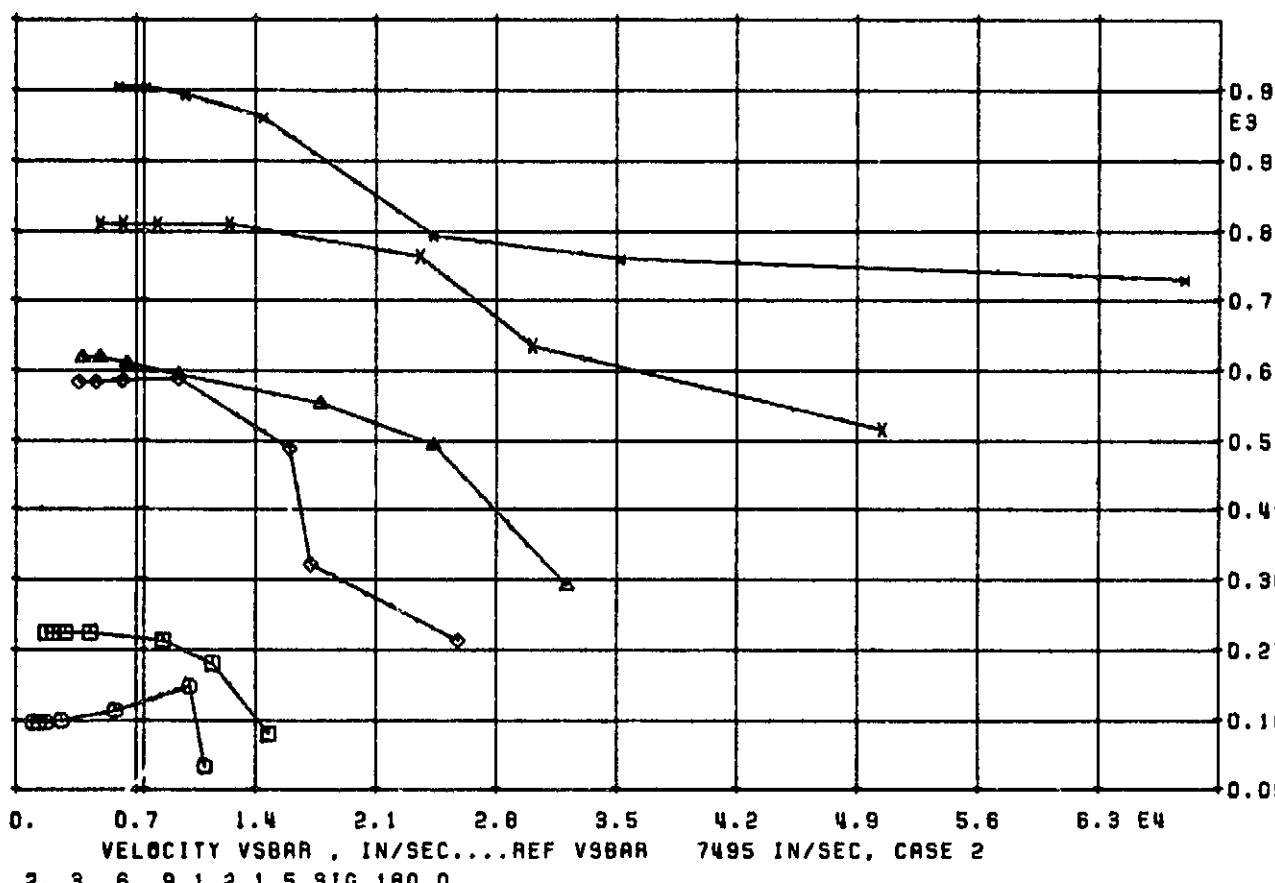
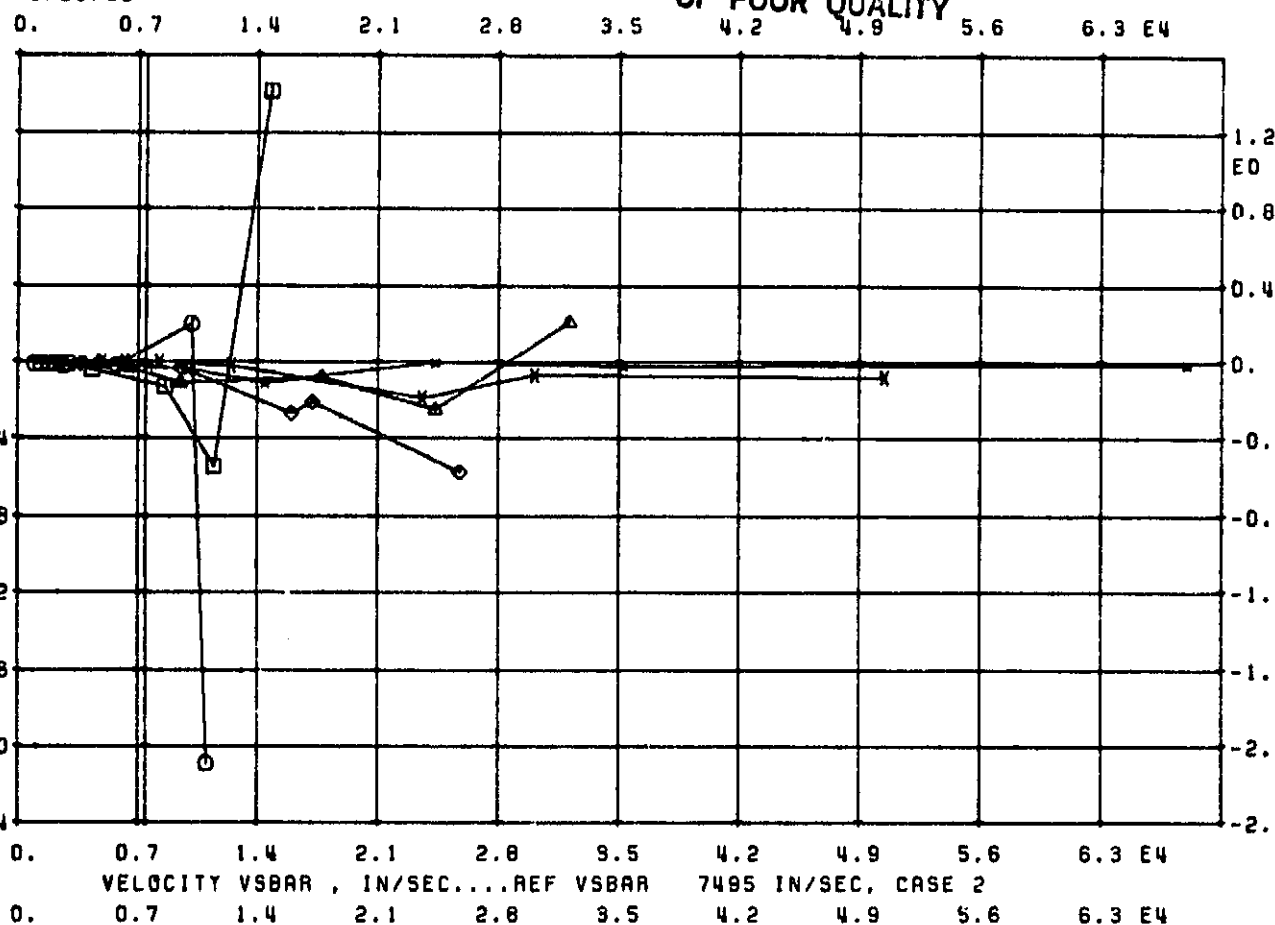
K .1..2..3..6..9.1.2.1.5.SIG 144.0
SOL 9 AERO,K 0 MODES AND FLUTTER

Figure 31. V-g, V-f Curves, Case 2

ORIGINAL PAGE IS
OF POOR QUALITY

3/26/82

6

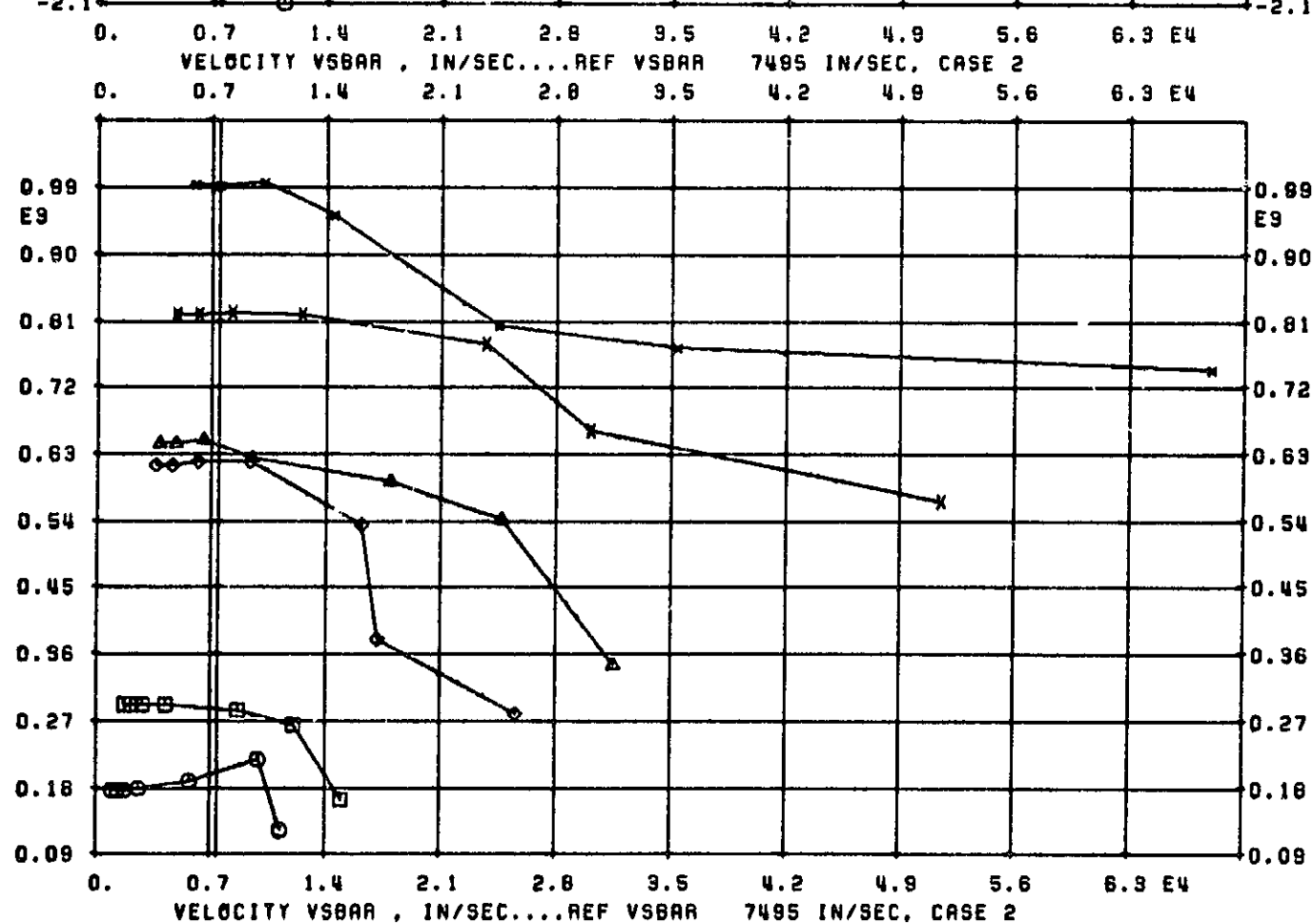
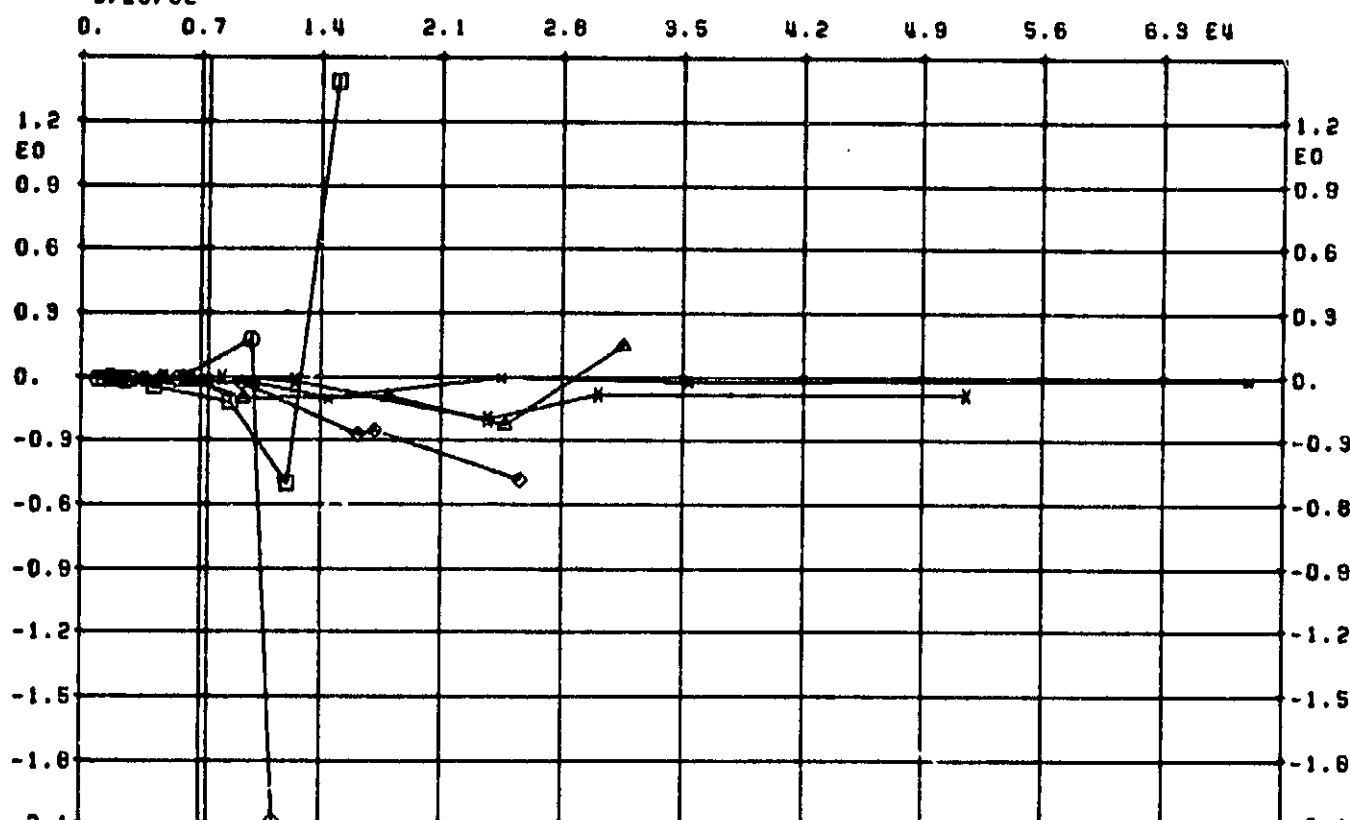


K .1..2..3..6..9.1.2.1.5.9IG 180.0
SOL 9 AERO.K 0 MODES AND FLUTTER

Figure 32. V-g, V-f Curves Case 2

ORIGINAL PAGE IS
OF POOR QUALITY

9/26/82

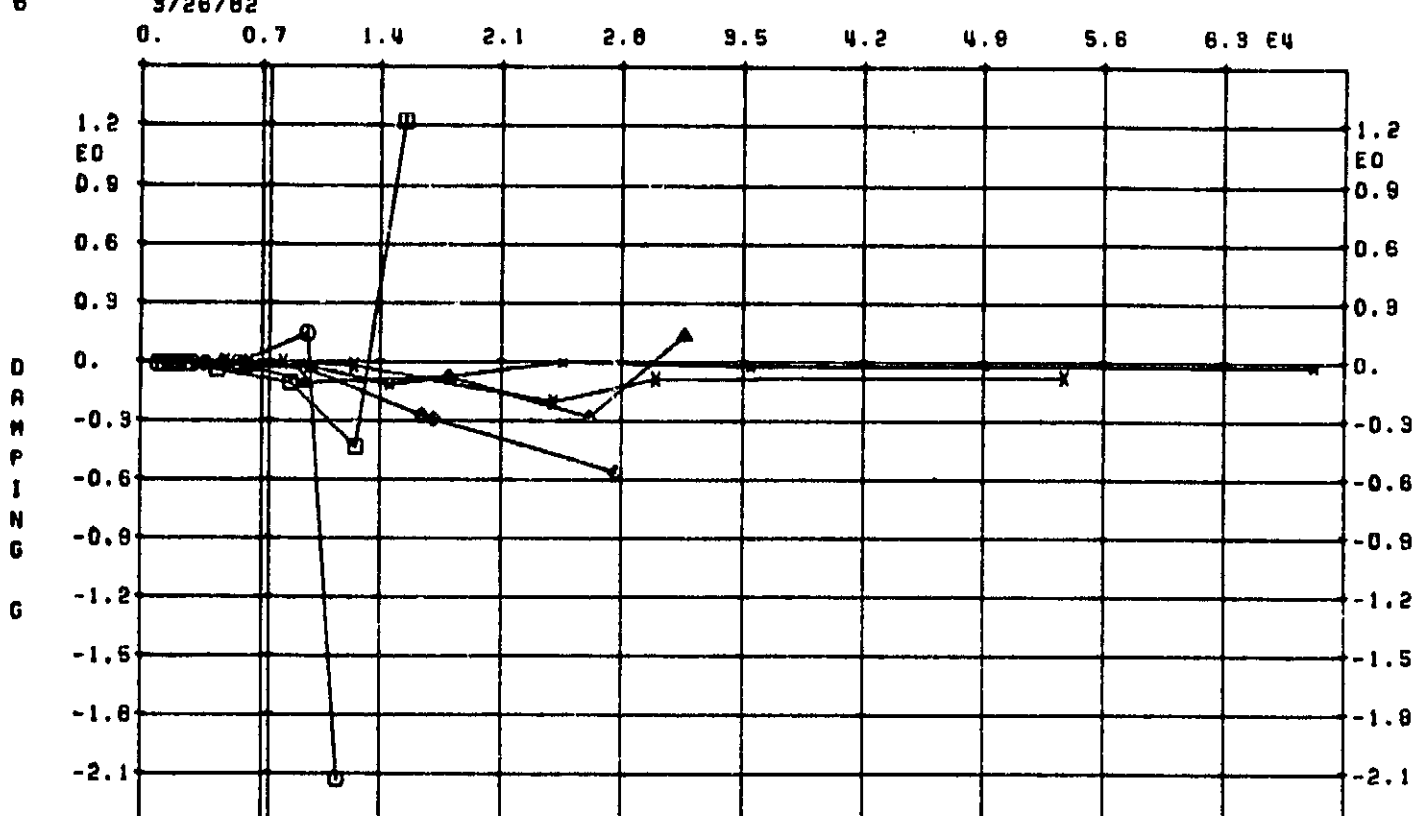


K .1..2..3..6..8.1.2.1.5.SIG -144.0
SQL 9 AERO,K 0 MODES AND FLUTTER

Figure 33. V-g, V-f Curves, Case 2

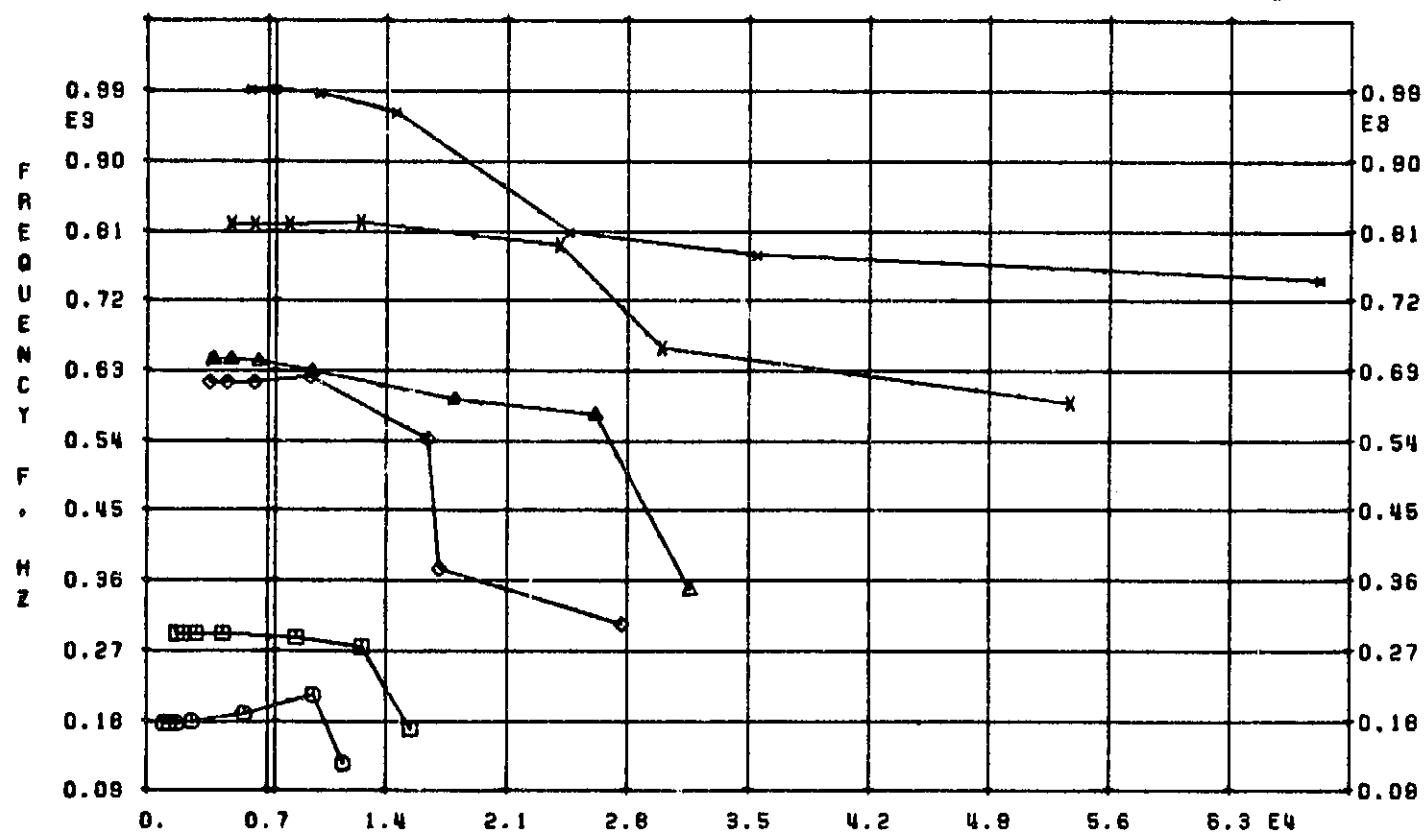
ORIGINAL PAGE IS
OF POOR QUALITY

3/26/62



VELOCITY $V\bar{S}$, IN/SEC....REF $V\bar{S}$ 7495 IN/SEC, CASE 2

0. 0.7 1.4 2.1 2.8 3.5 4.2 4.9 5.6 6.3 E4



VELOCITY $V\bar{S}$, IN/SEC....REF $V\bar{S}$ 7495 IN/SEC, CASE 2

K .1..2..3..6..8.1.2.1.5.SIG ~108.0

SOL 9 AERO,K 0 MODES AND FLUTTER

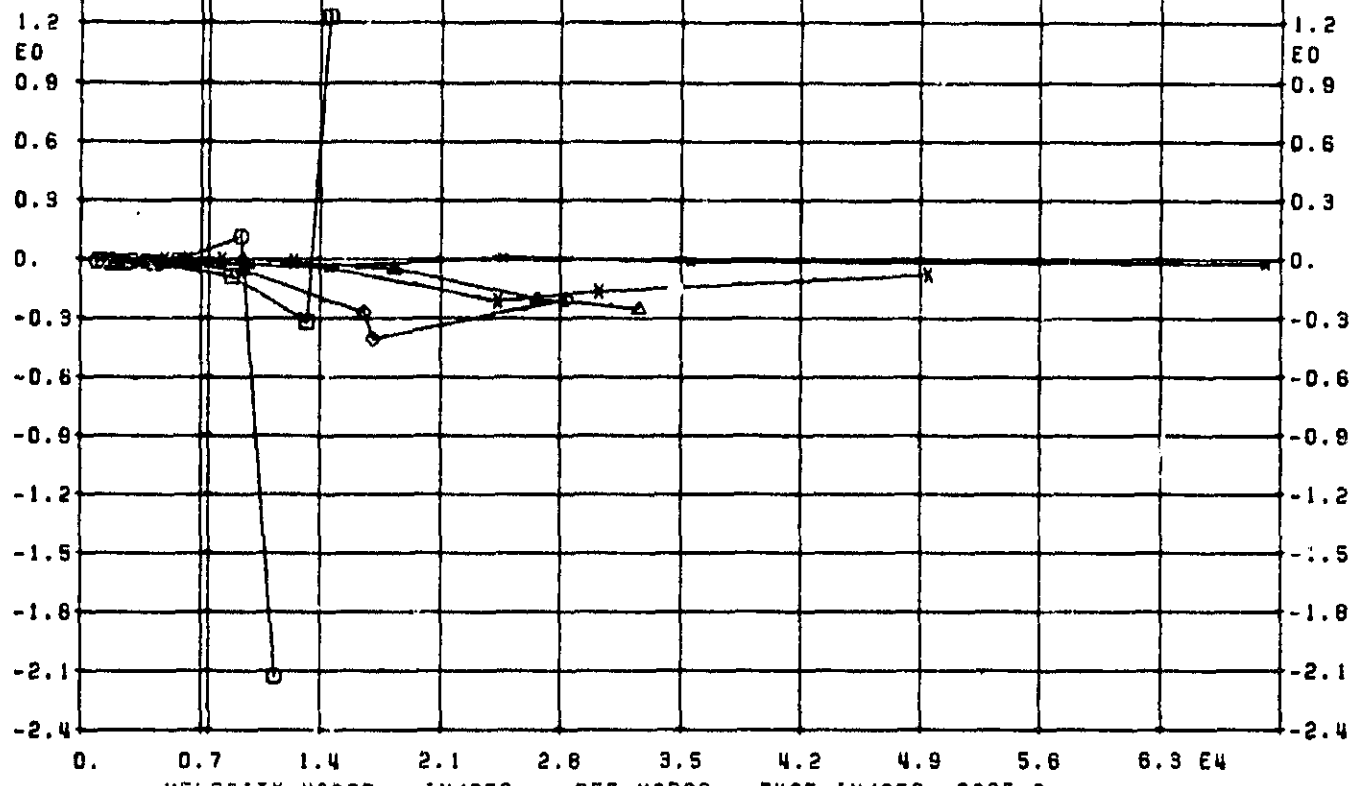
Figure 34. V-g, V-f Curves, Case 2

3/26/82

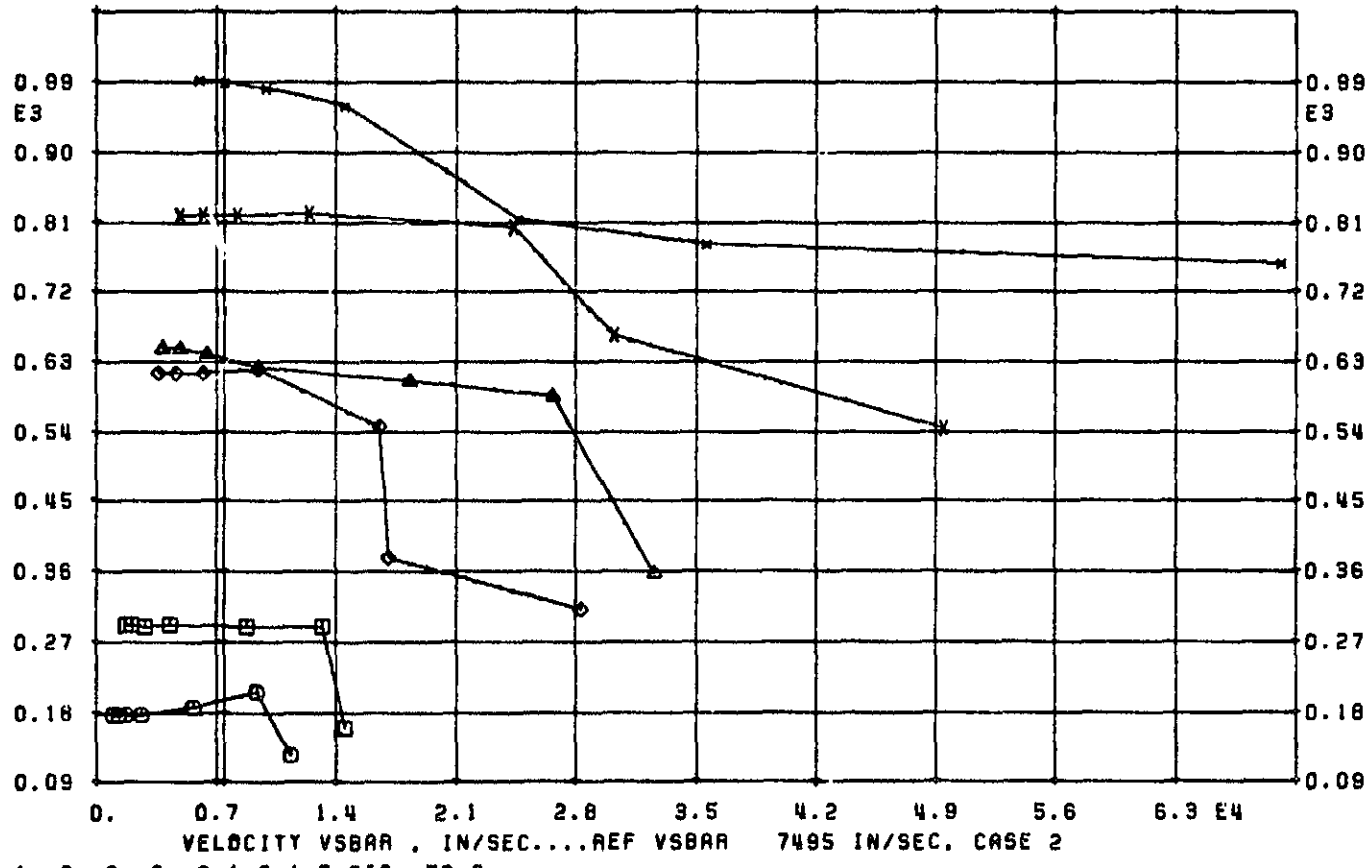
ORIGINAL PAGE IS
OF PQOR QUALITY

0. 0.7 1.4 2.1 2.8 3.5 5.6 6.3 E4

DAMPING



FREQUENCY



K .1..2..3..6..9.1.2.1.5.SIG -72.0

SOL 8 RERO,K 0 MODES AND FLUTTER

Figure 35. V-g, V-f Curves, Case 2

ORIGINAL PAGE IS
OF POOR QUALITY

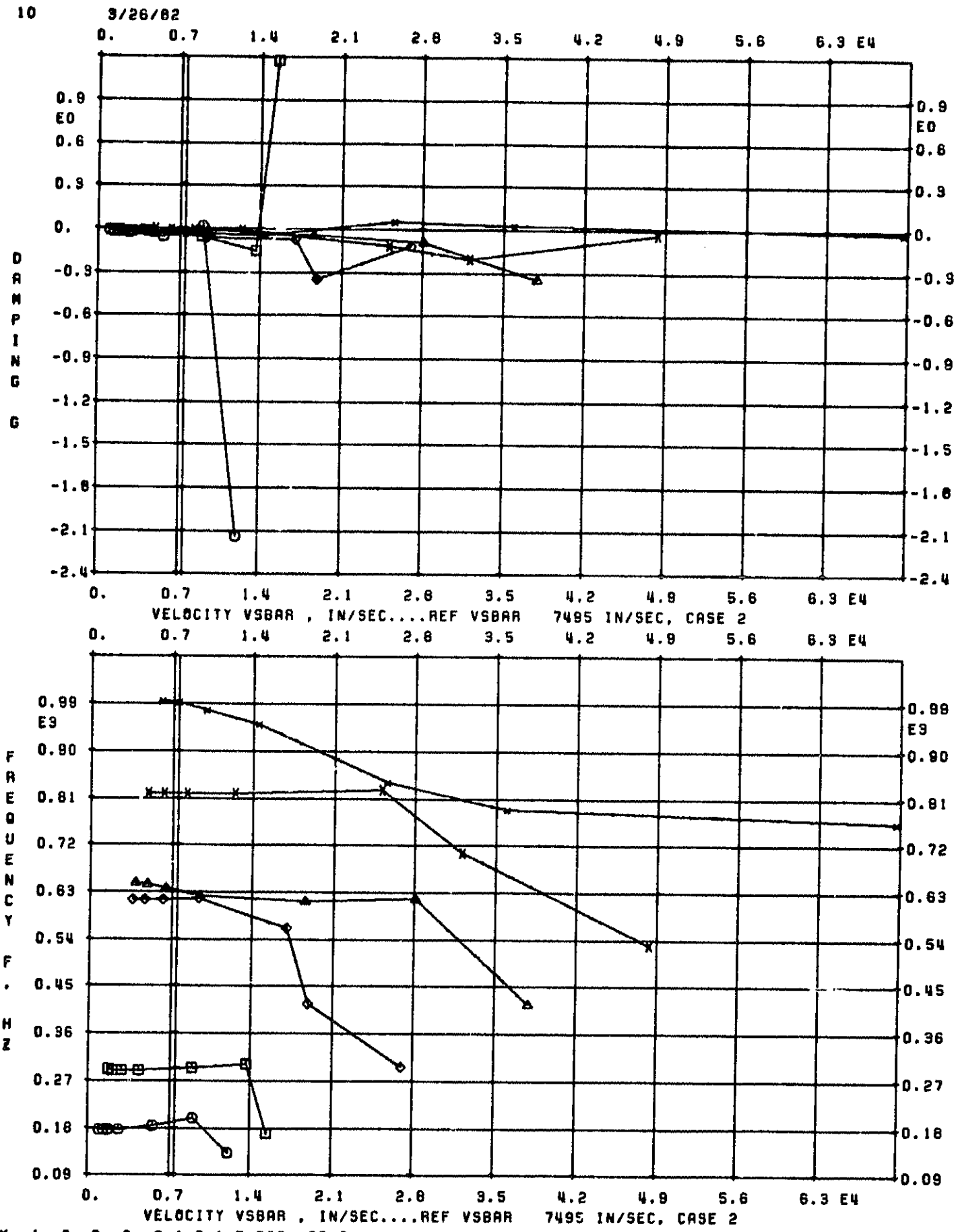
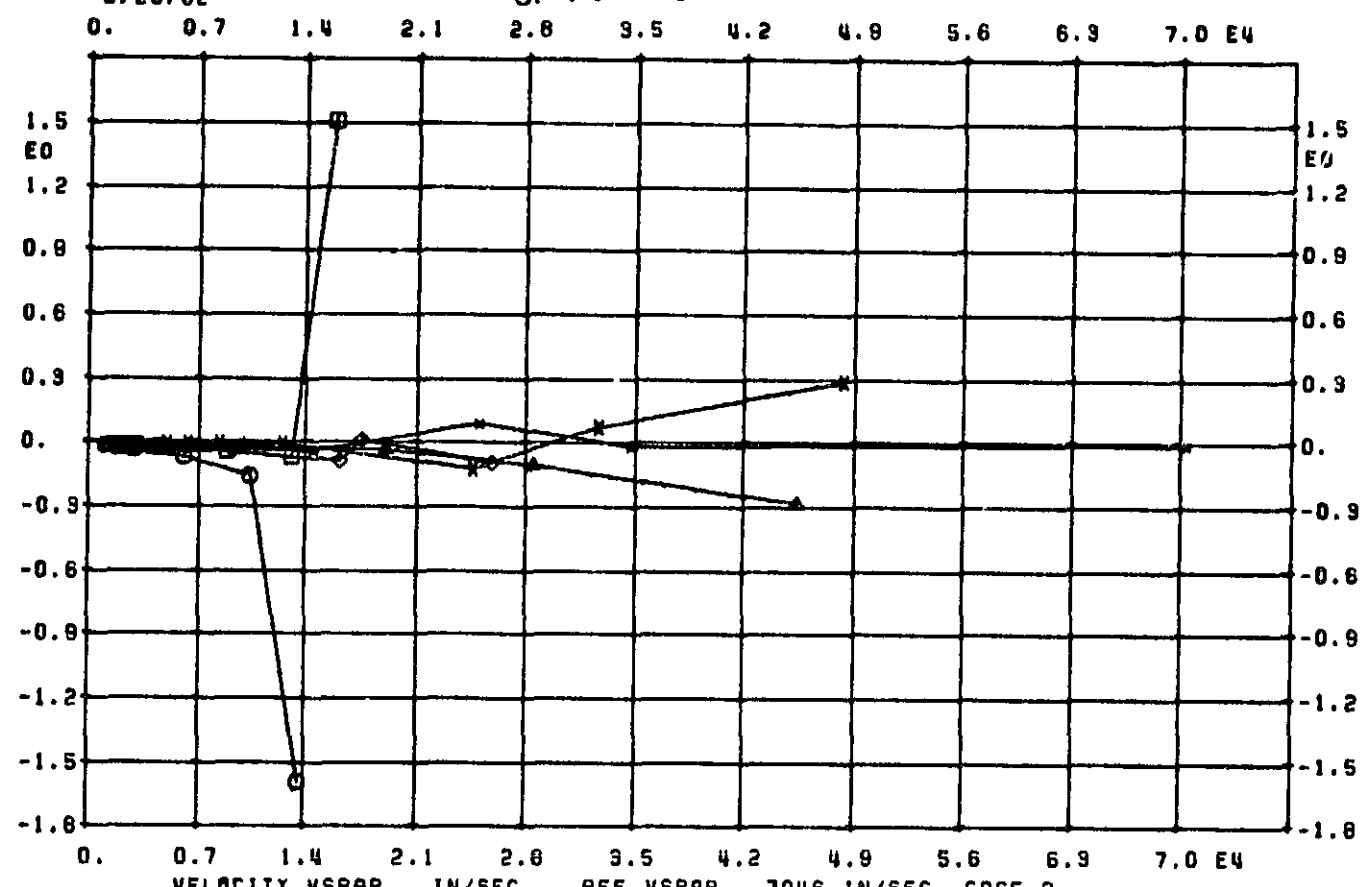


Figure 36. V-q, V-f Curves, Case 2

ORIGINAL PAGE IS
OF POOR QUALITY

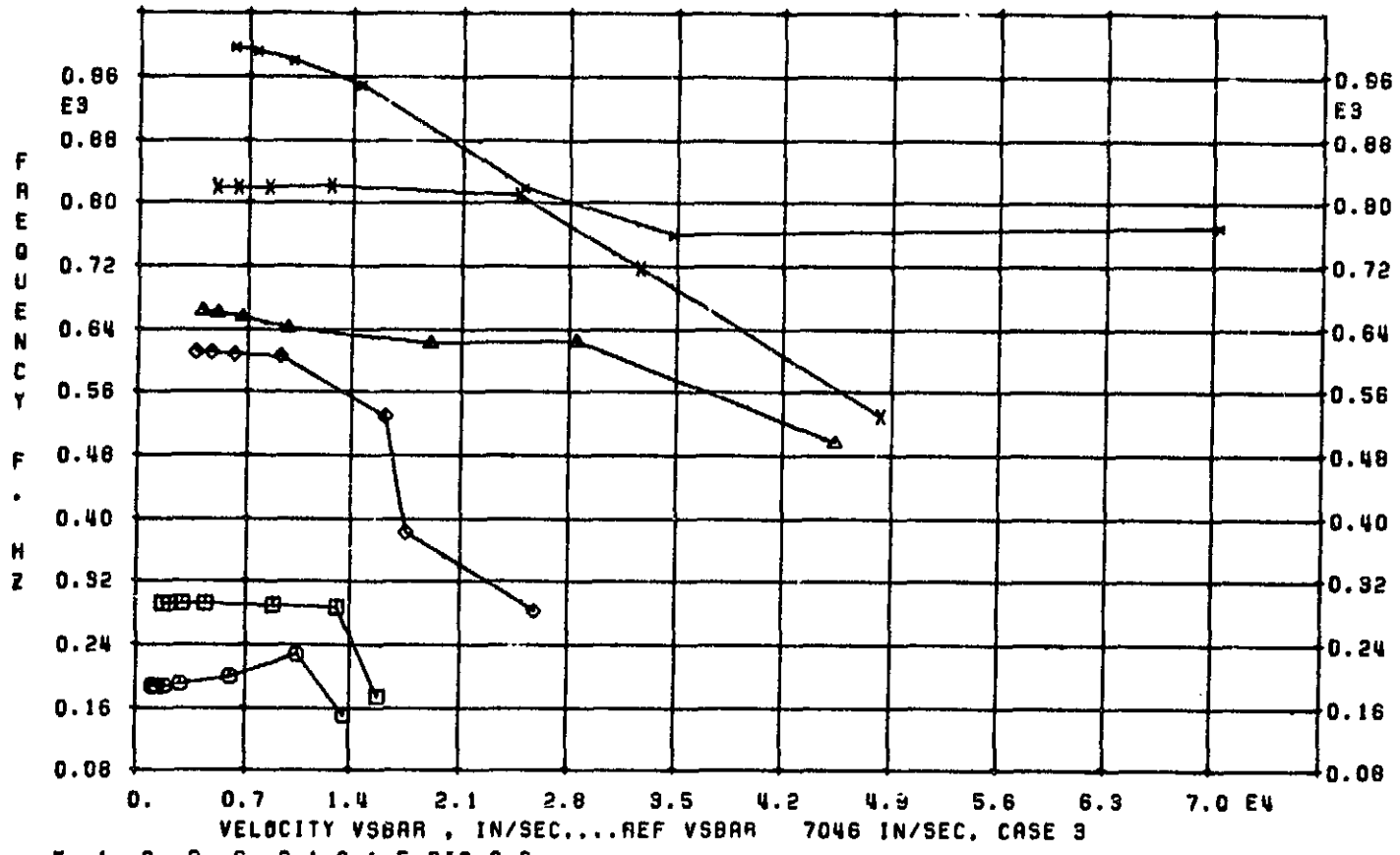
3/26/82



0. 0.7 1.4 2.1 2.8 3.5 4.2 4.9 5.6 6.9 7.0 E4

VELOCITY VSBAR , IN/SEC....REF VSBAR 7046 IN/SEC, CASE 3

0. 0.7 1.4 2.1 2.8 3.5 4.2 4.9 5.6 6.9 7.0 E4



0. 0.7 1.4 2.1 2.8 3.5 4.2 4.9 5.6 6.9 7.0 E4

VELOCITY VSBAR , IN/SEC....REF VSBAR 7046 IN/SEC, CASE 3

K .1..2..3..6..9.1.2.1.5.5IG 0.0

SOL 9 AERO,K 0 FLUTTER RUN,DEN RATIO 1.0

Figure 37. V-g, V-f Curves, Case 3

ORIGINAL PLOT IS
OF POOR QUALITY

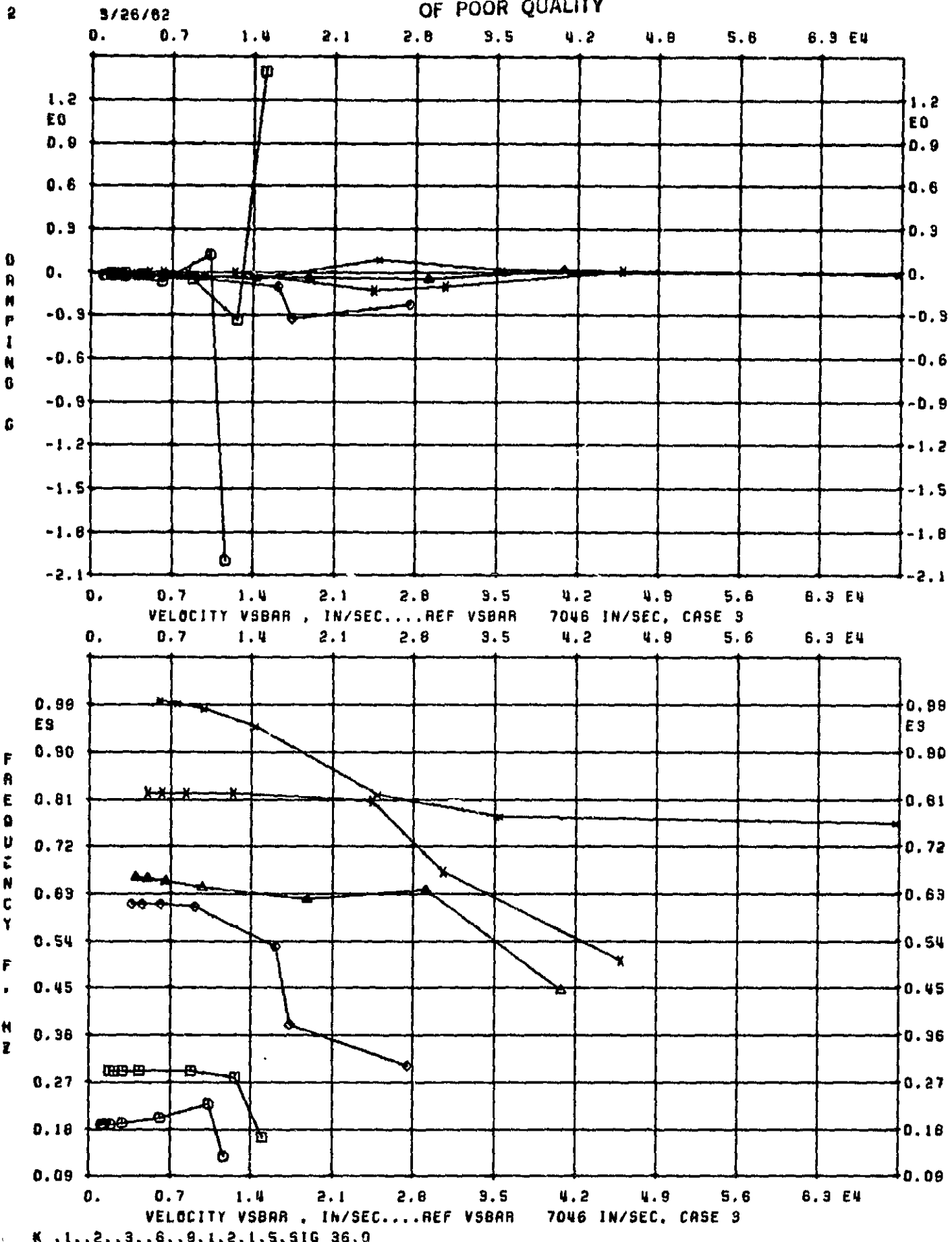


Figure 38. V-g, V-f Curves, Case 3

ORIGINAL PAGE IS
OF POOR QUALITY

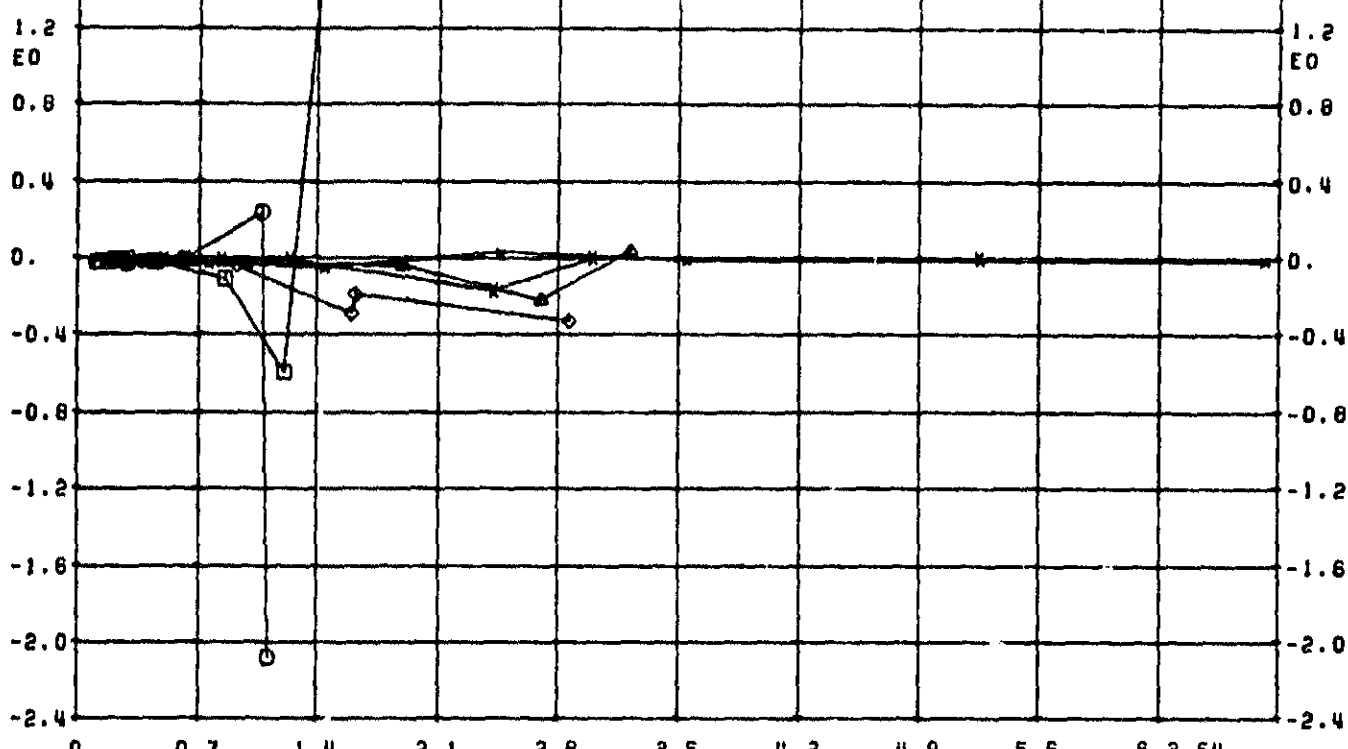
9

3/26/82

9

0. 0.7 1.4 2.1 2.8 3.5 4.2 4.9 5.6 6.3 E4

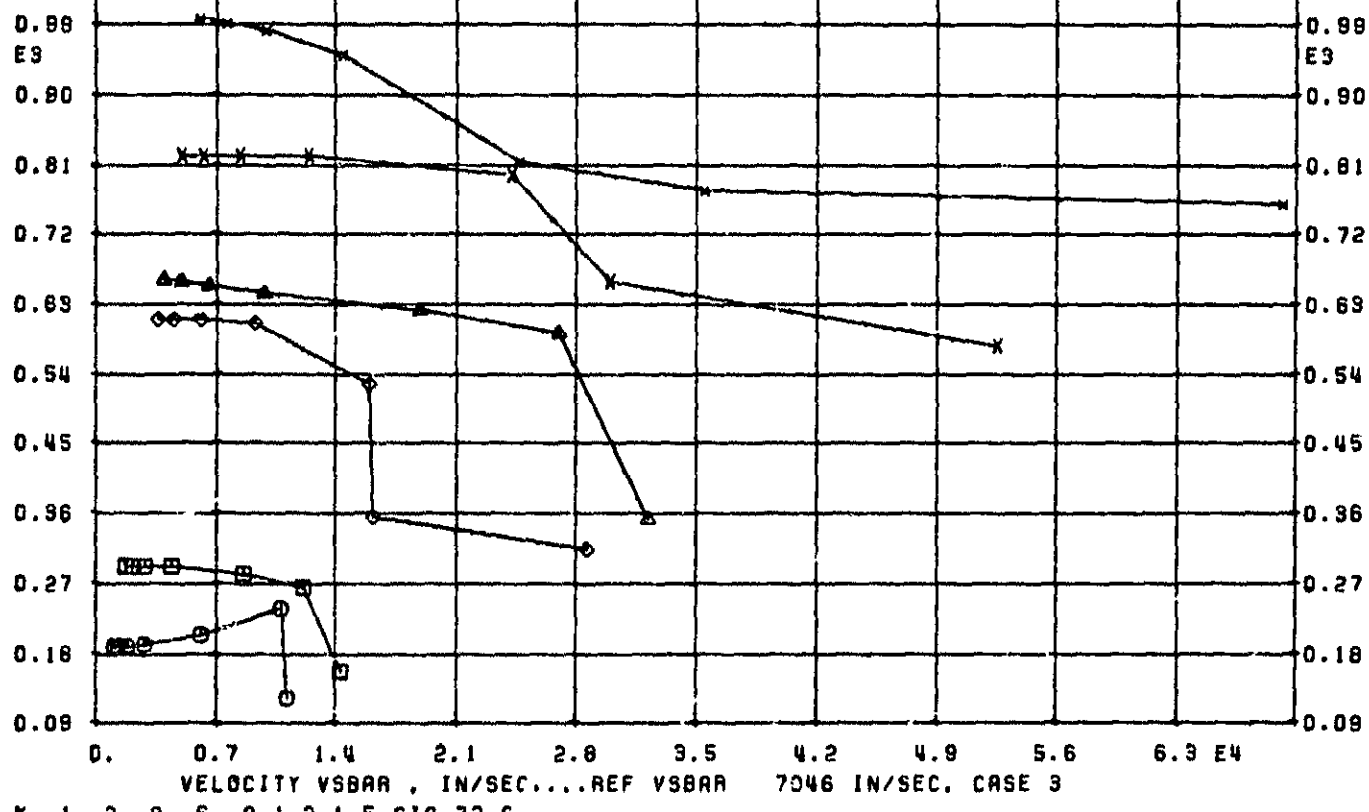
DAMPING



VELOCITY VSBAR , IN/SEC....REF VSBAR 7046 IN/SEC. CASE 3

0. 0.7 1.4 2.1 2.8 3.5 4.2 4.9 5.6 6.3 E4

FREQUENCY



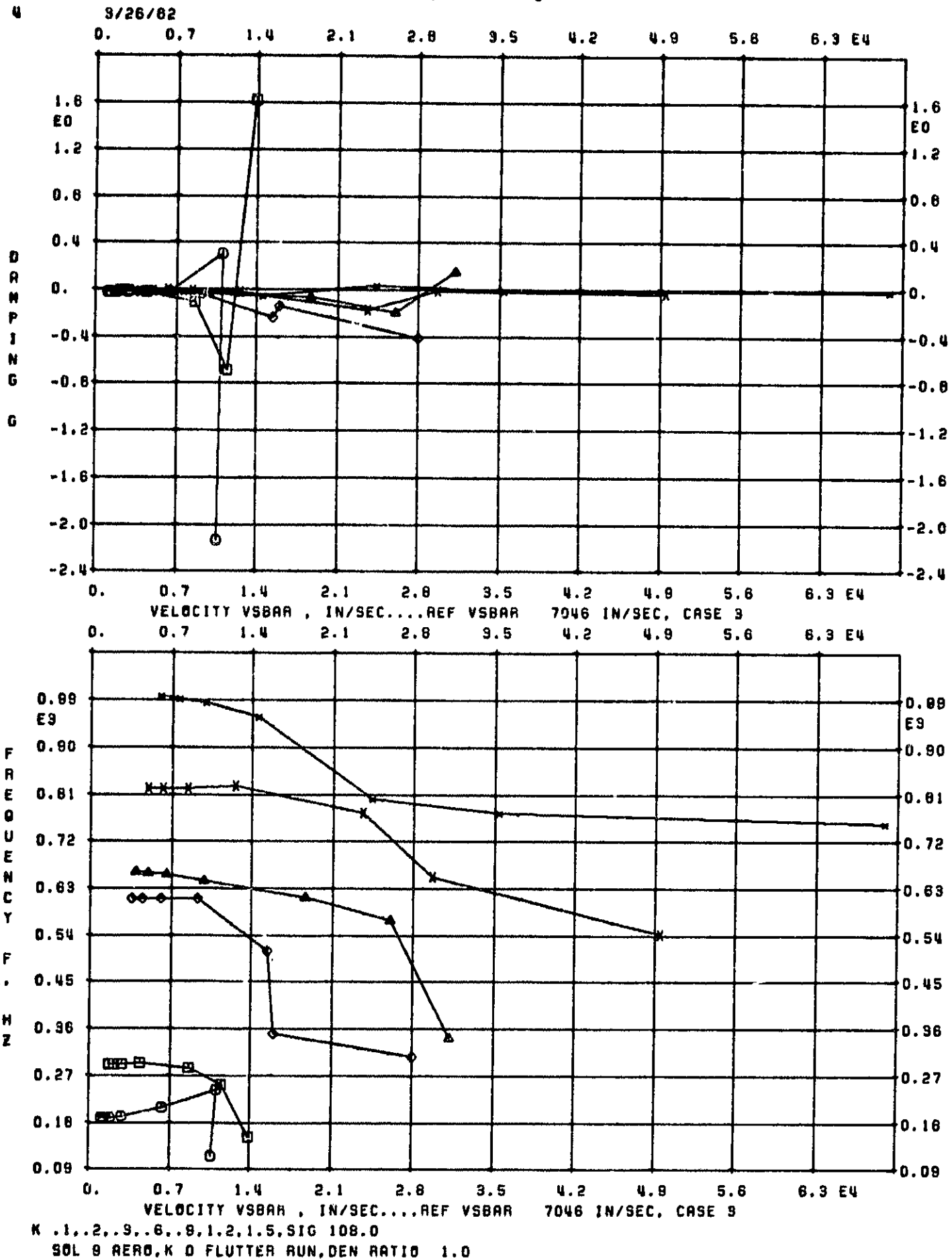
VELOCITY VSBAR , IN/SEC....REF VSBAR 7046 IN/SEC. CASE 3

K .1..2..3..6..9.1.2.1.5,SIG 72.0

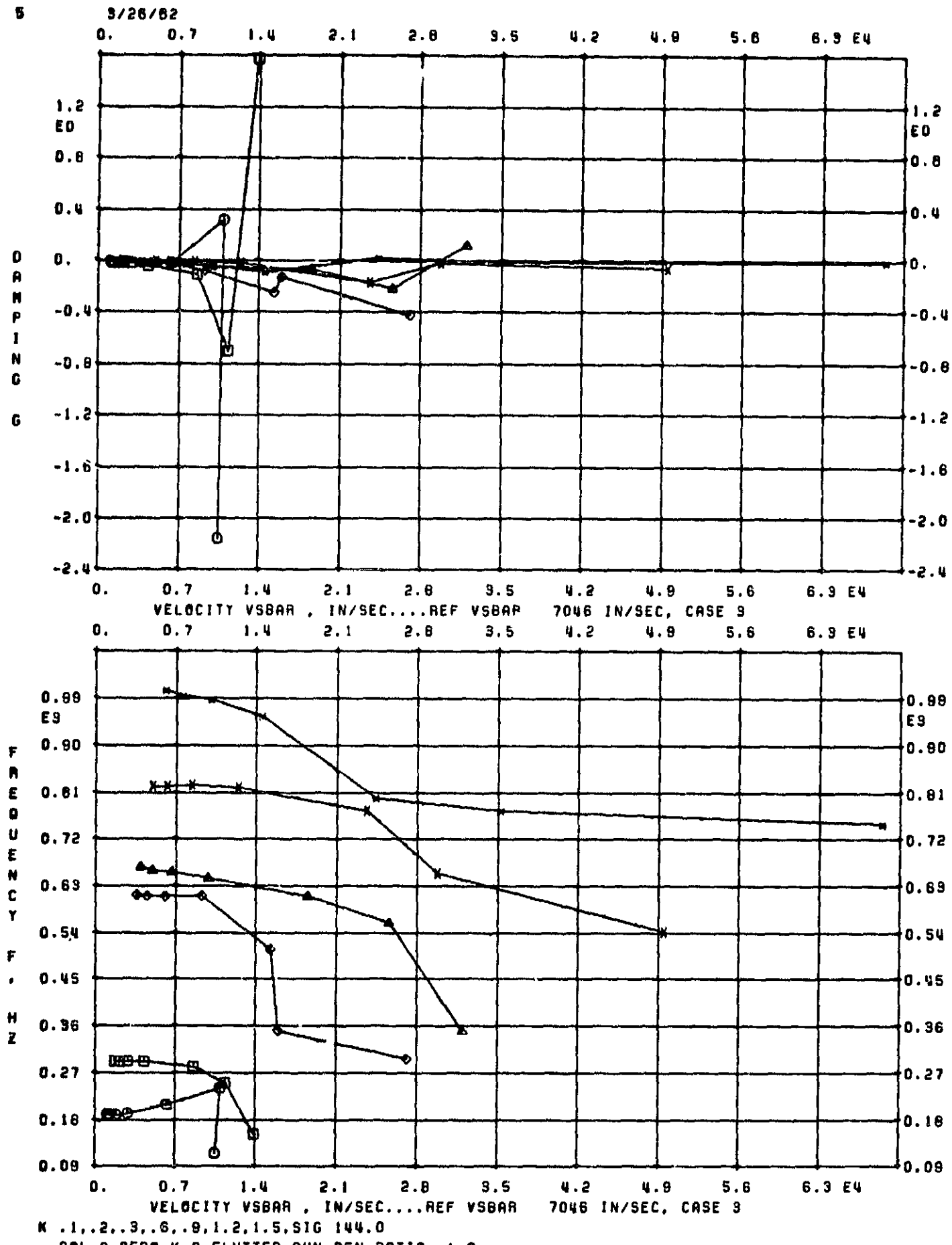
SOL 9 AERO,K 0 FLUTTER RUN,DEN RATIO 1.0

Figure 39 . V-g, V-f Curves, Case 3

ORIGINAL PAGE IS
OF POOR QUALITY



ORIGINAL PAGE IS
OF POOR QUALITY



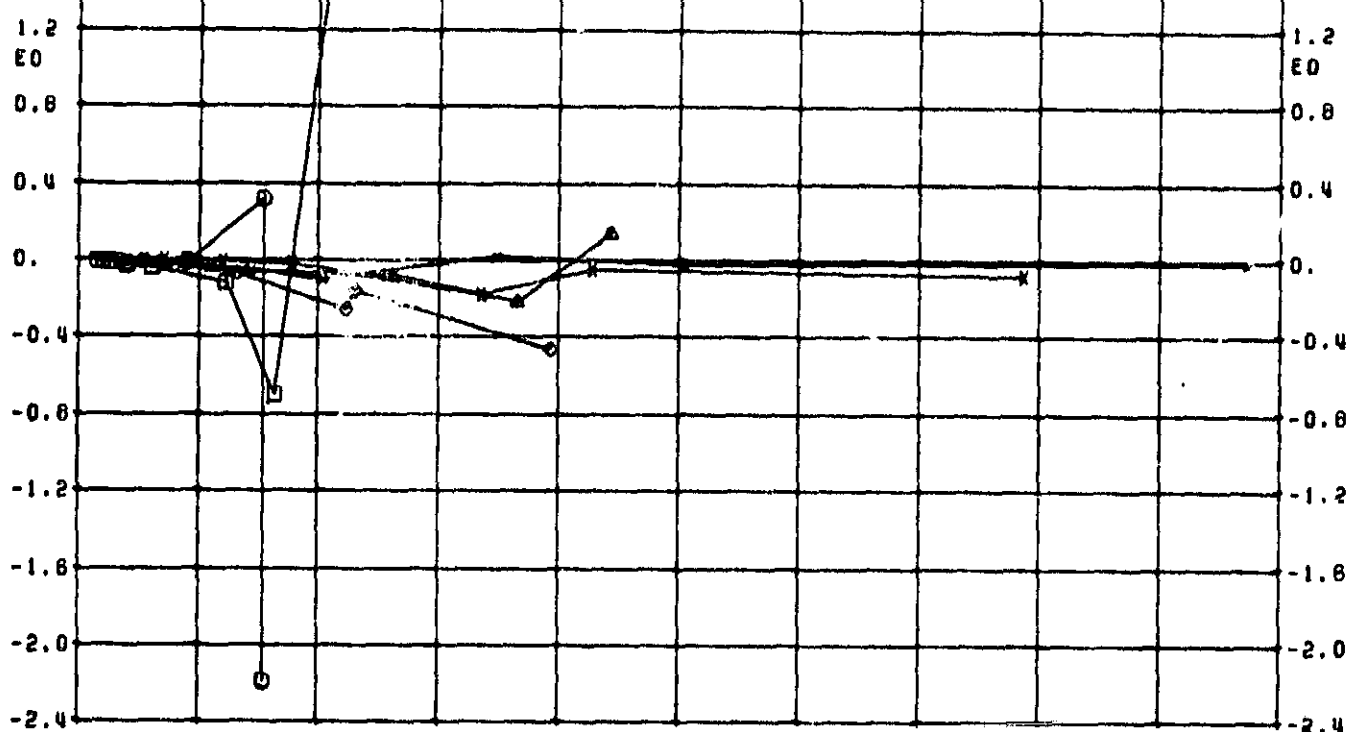
ORIGINAL PAGE IS
OF POOR QUALITY

9/26/02

6

0. 0.7 1.4 2.1 2.8 3.5 4.2 4.9 5.6 6.3 E4

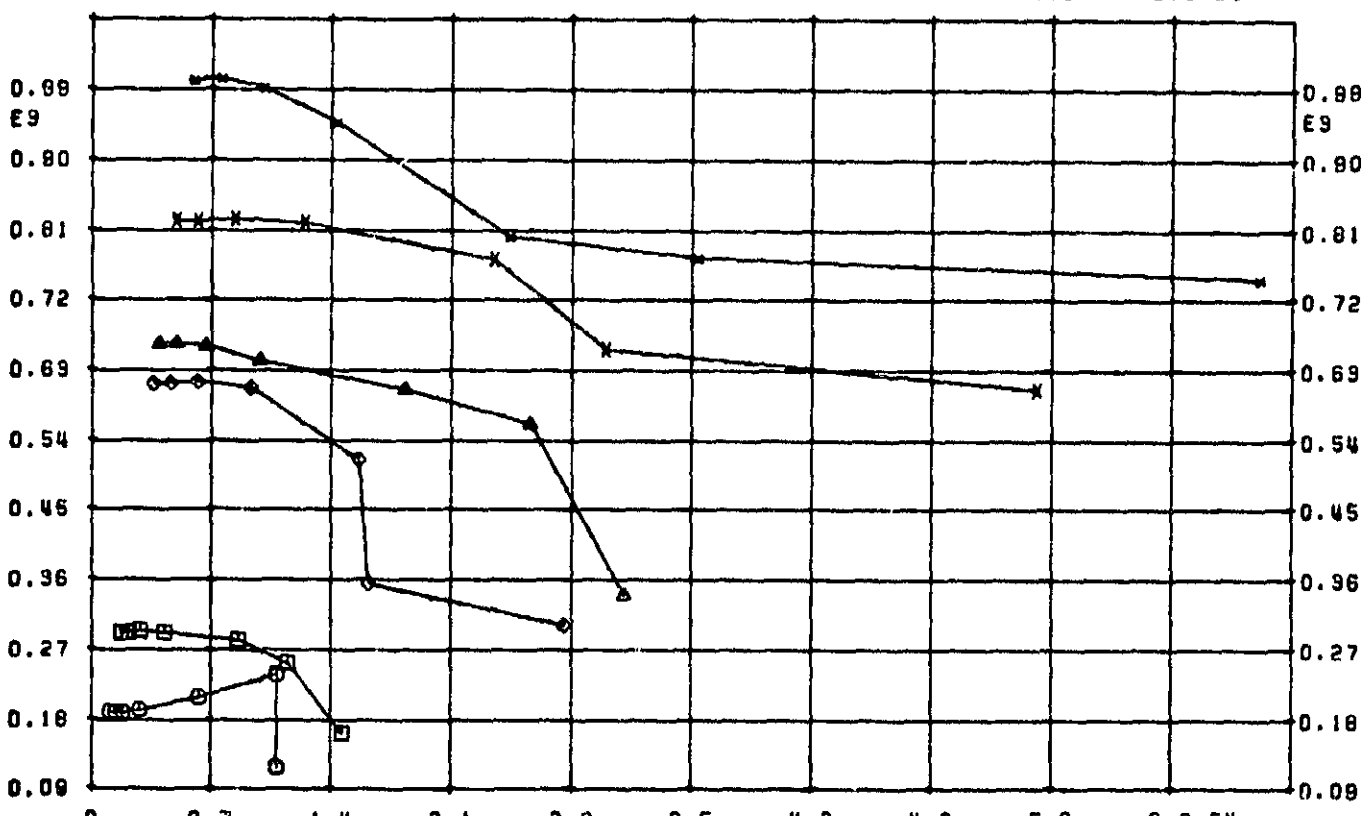
DAMPING



VELOCITY VSBAR , IN/SEC....REF VSBAR 7046 IN/SEC, CASE 3

0. 0.7 1.4 2.1 2.8 3.5 4.2 4.9 5.6 6.3 E4

FREQUENCY



VELOCITY VSBAR , IN/SEC....REF VSBAR 7046 IN/SEC, CASE 3

K .1..2..9..6..8..1..2..1..5..SIG 180.0
SOL 8 AERO,K 0 FLUTTER RUN,DEN RATIO 1.0

Figure 42. V-g, V-f Curves, Case 3

ORIGINAL PAGE IS
OF POOR QUALITY

3/26/62

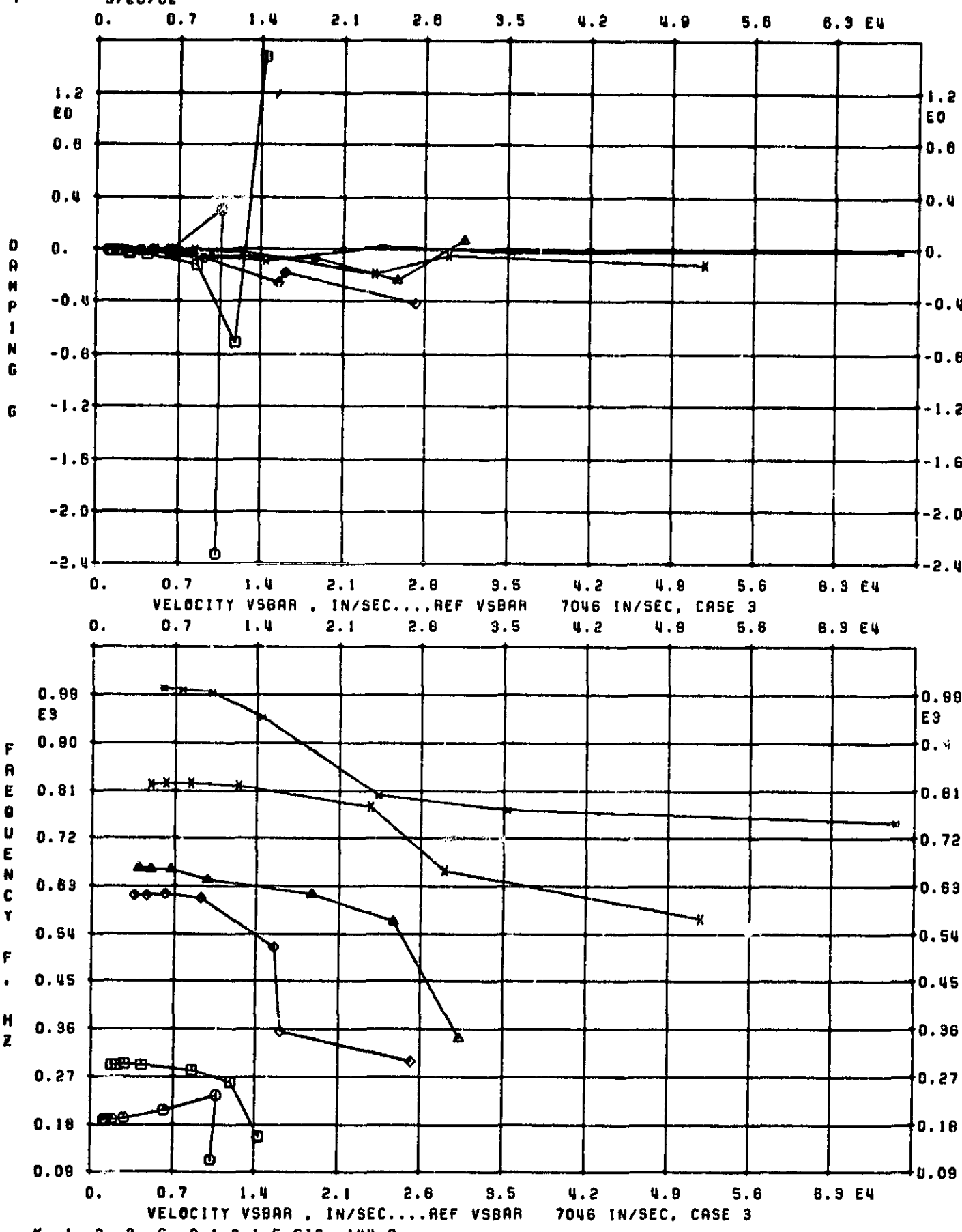


Figure 43. V-g, V-f Curves, Case 3

ORIGINAL PAGE IS
OF POOR QUALITY

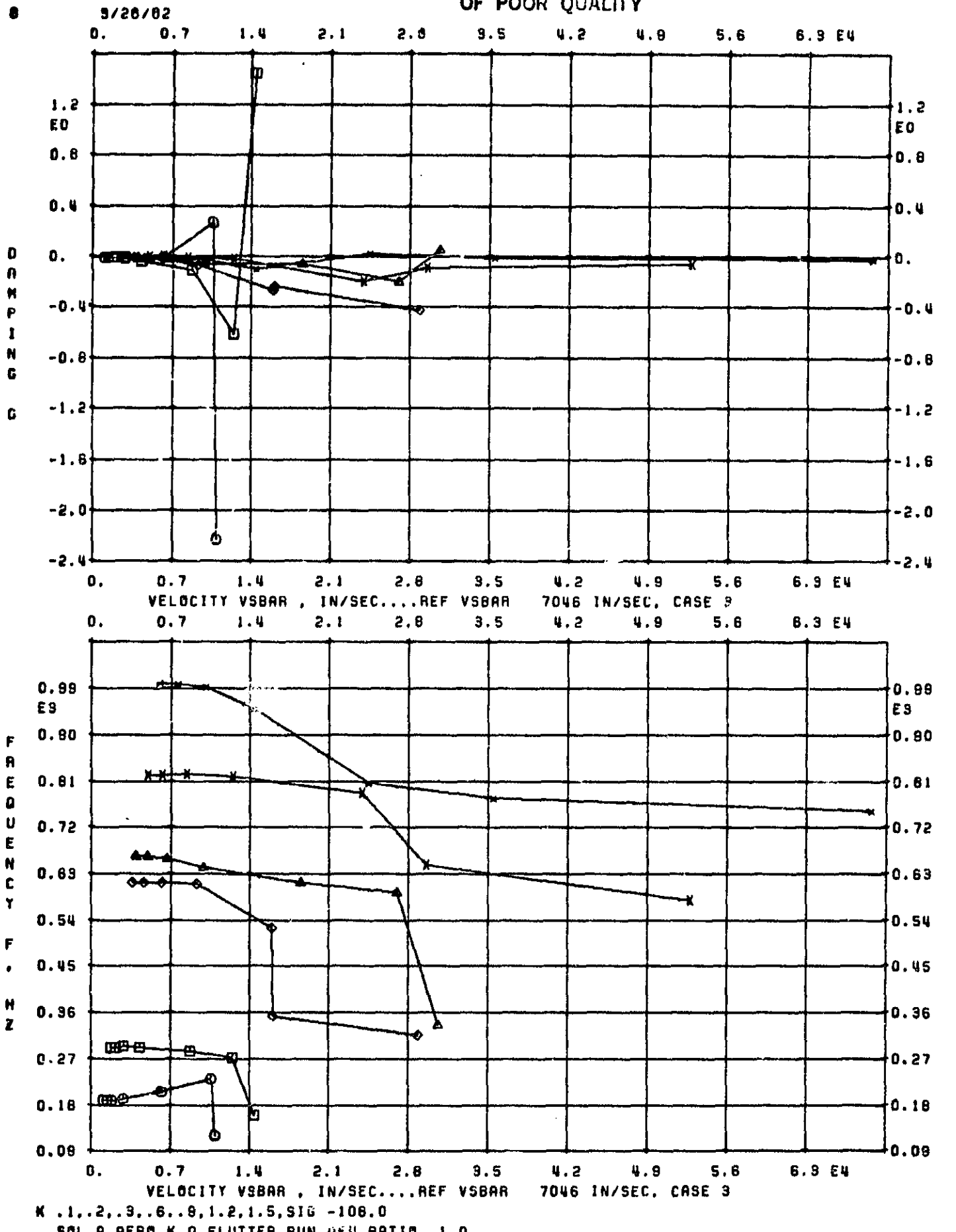
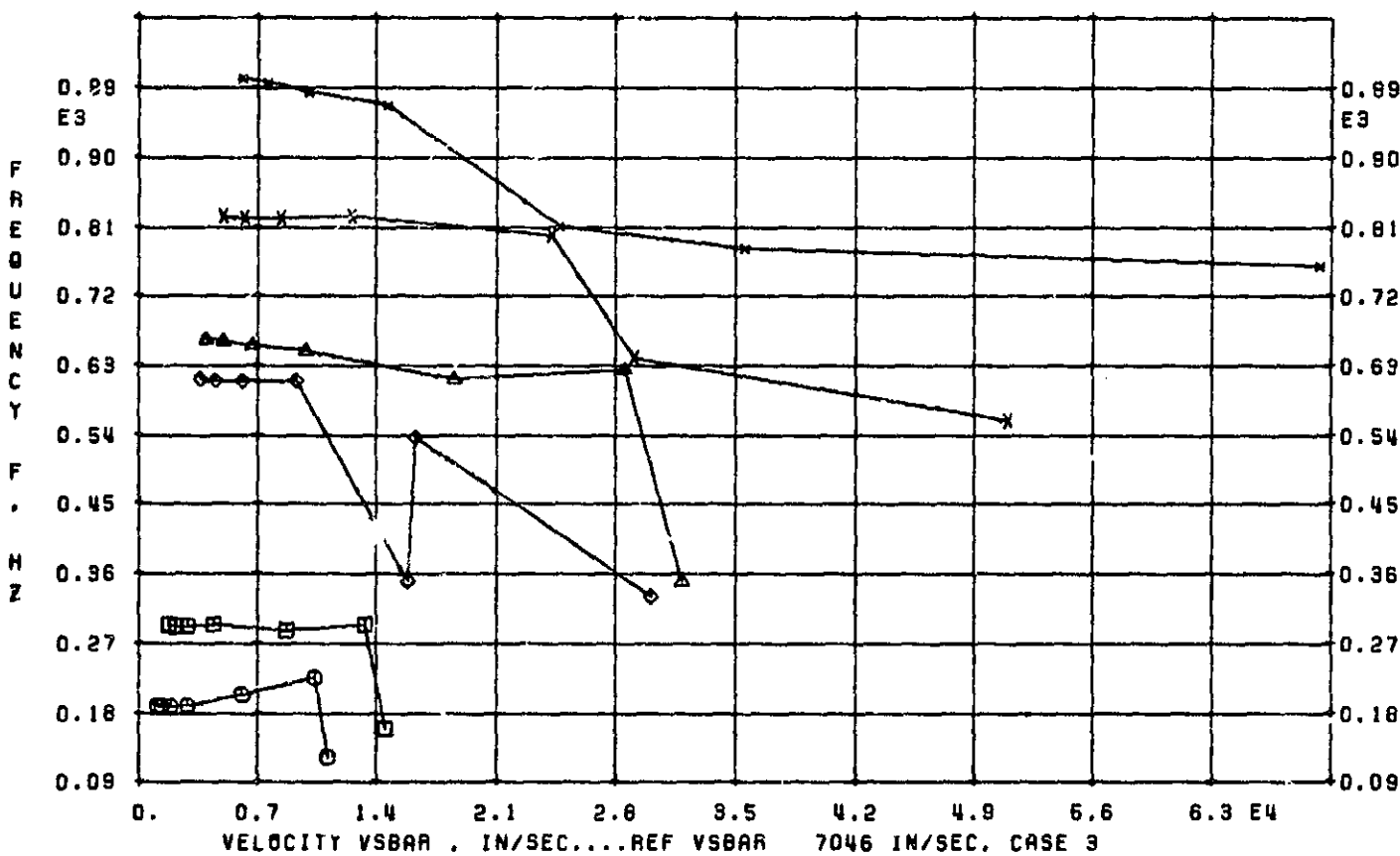
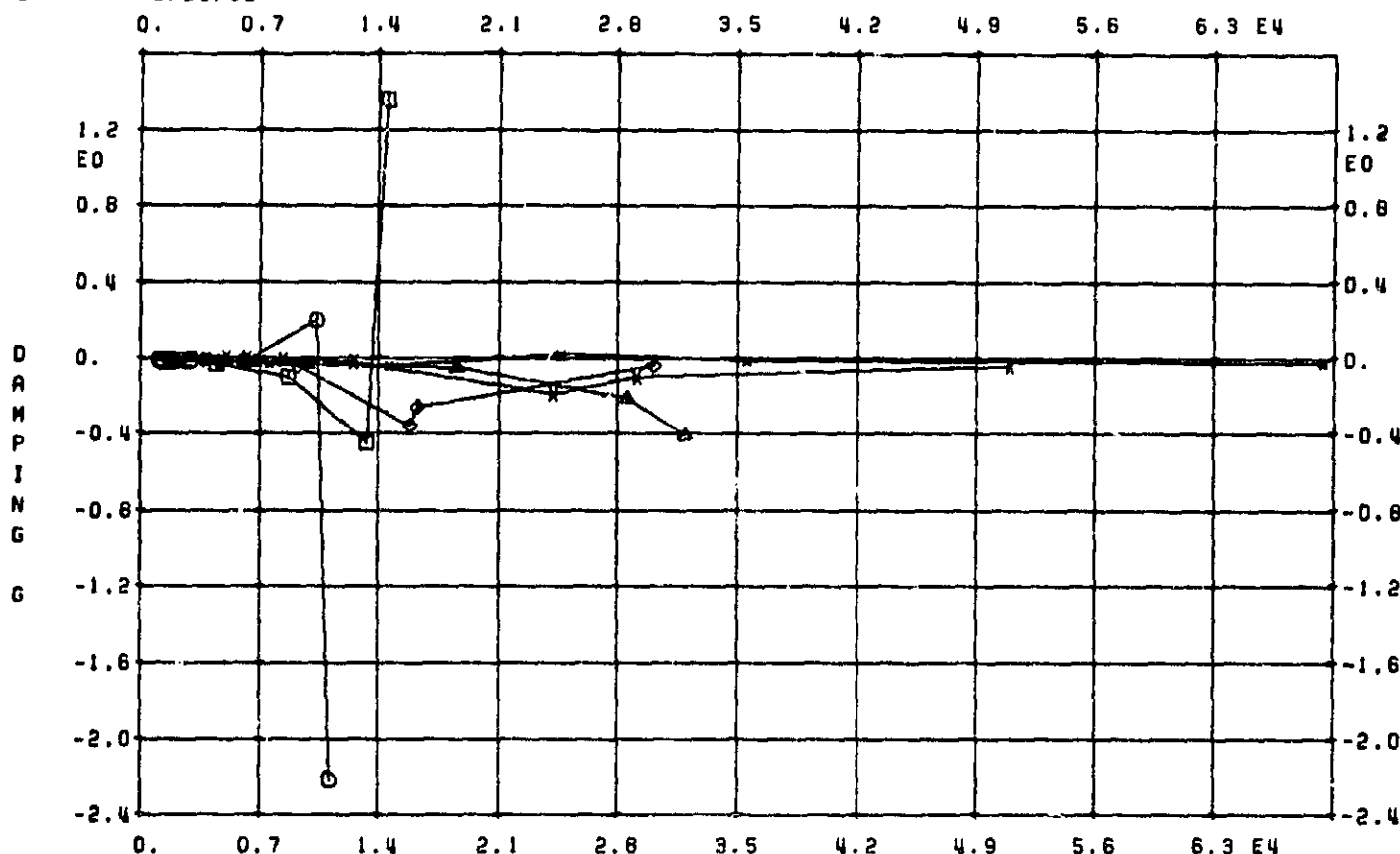


Figure 44. V-g, V-f Curves, Case 3

ORIGINAL PAGE IS
OF POOR QUALITY

3/26/82

9



K .1.,.2.,.3.,.6.,.9.1.2,1.5.SIG -72.0

SOL 9 AERO,K 0 FLUTTER RUN,DEN RATIO 1.0

Figure 45. V-g, V-f Curves Case 3

ORIGINAL PAGE IS
OF POOR QUALITY

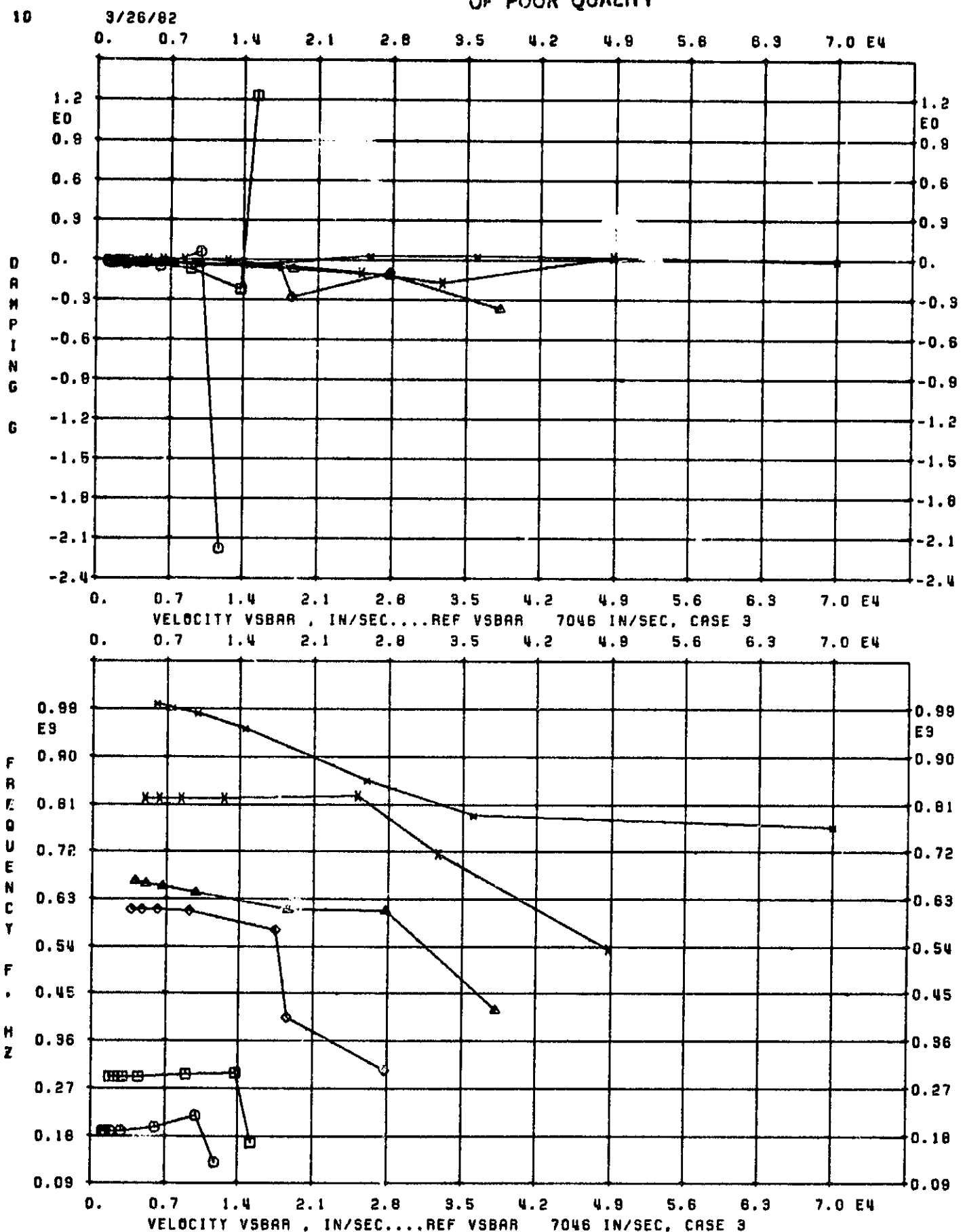
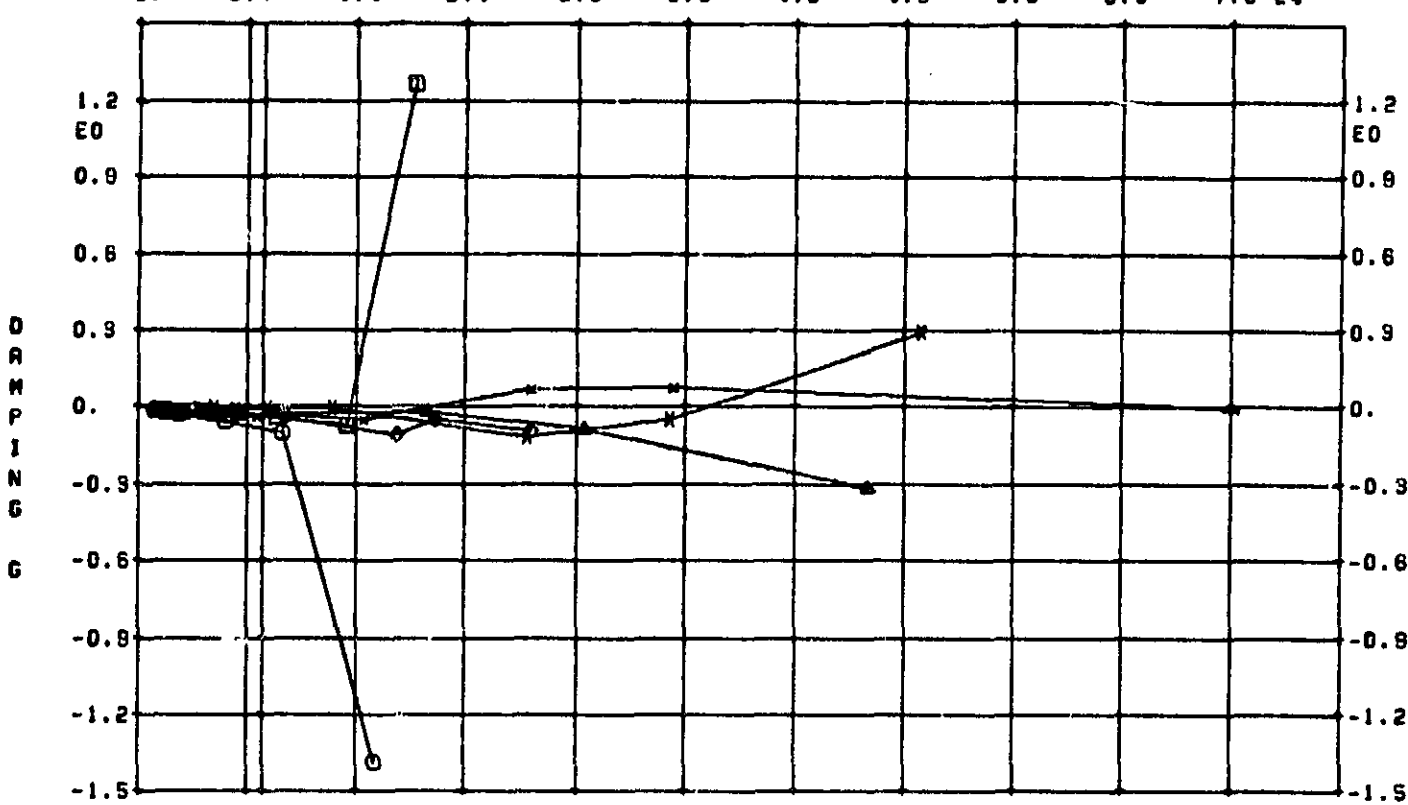


Figure 46. V-g, V-f Curves, Case 3

ORIGINAL PAGE IS
OF POOR QUALITY

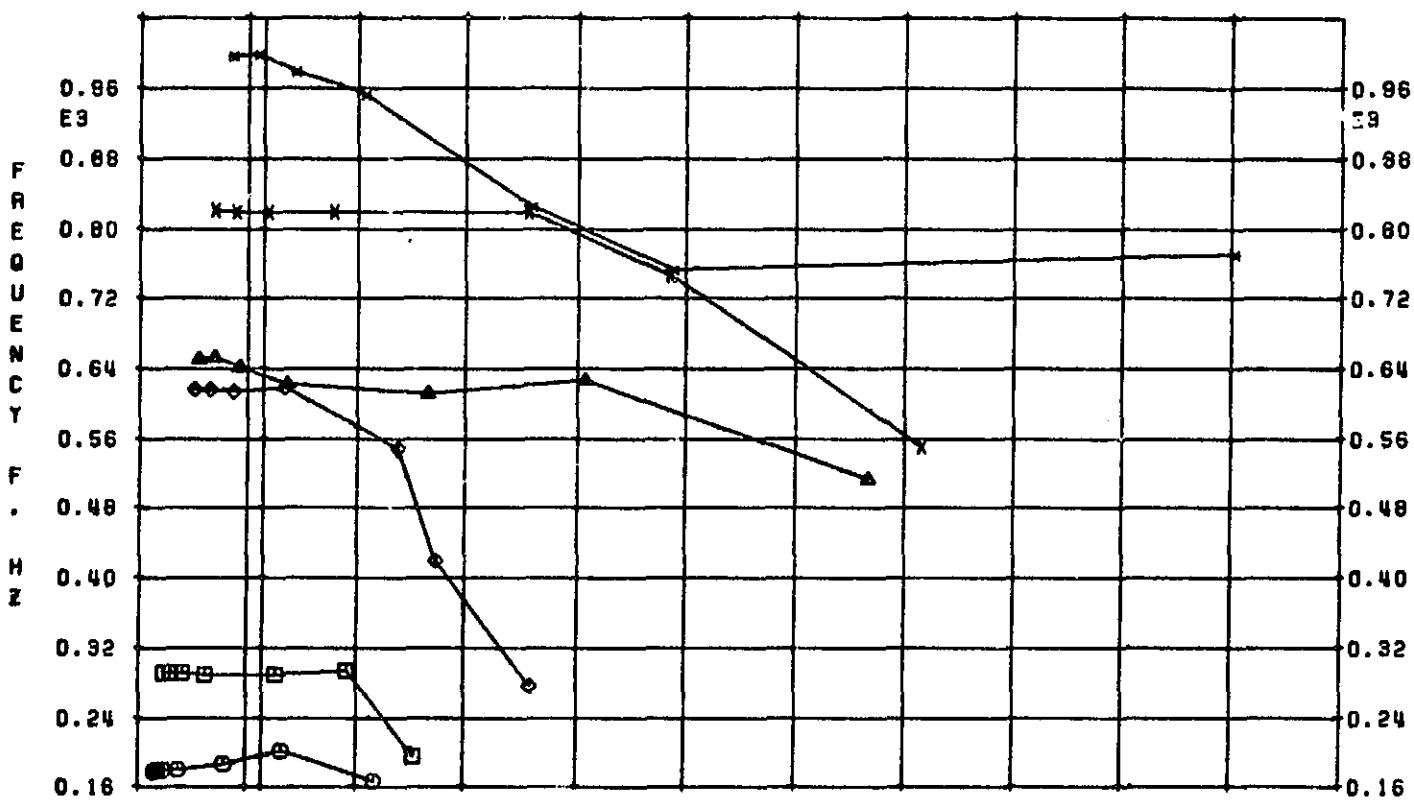
9/26/82

0. 0.7 1.4 2.1 2.8 3.5 4.2 4.9 5.6 6.3 7.0 E4



VELOCITY VSBAR , IN/SEC....REF VSBAR 7857 IN/SEC, CASE 4

0. 0.7 1.4 2.1 2.8 3.5 4.2 4.9 5.6 6.3 7.0 E4



VELOCITY VSBAR , IN/SEC....REF VSBAR 7857 IN/SEC, CASE 4

K .1..2..3..6..9.1.2.1.5.SIG 0.0

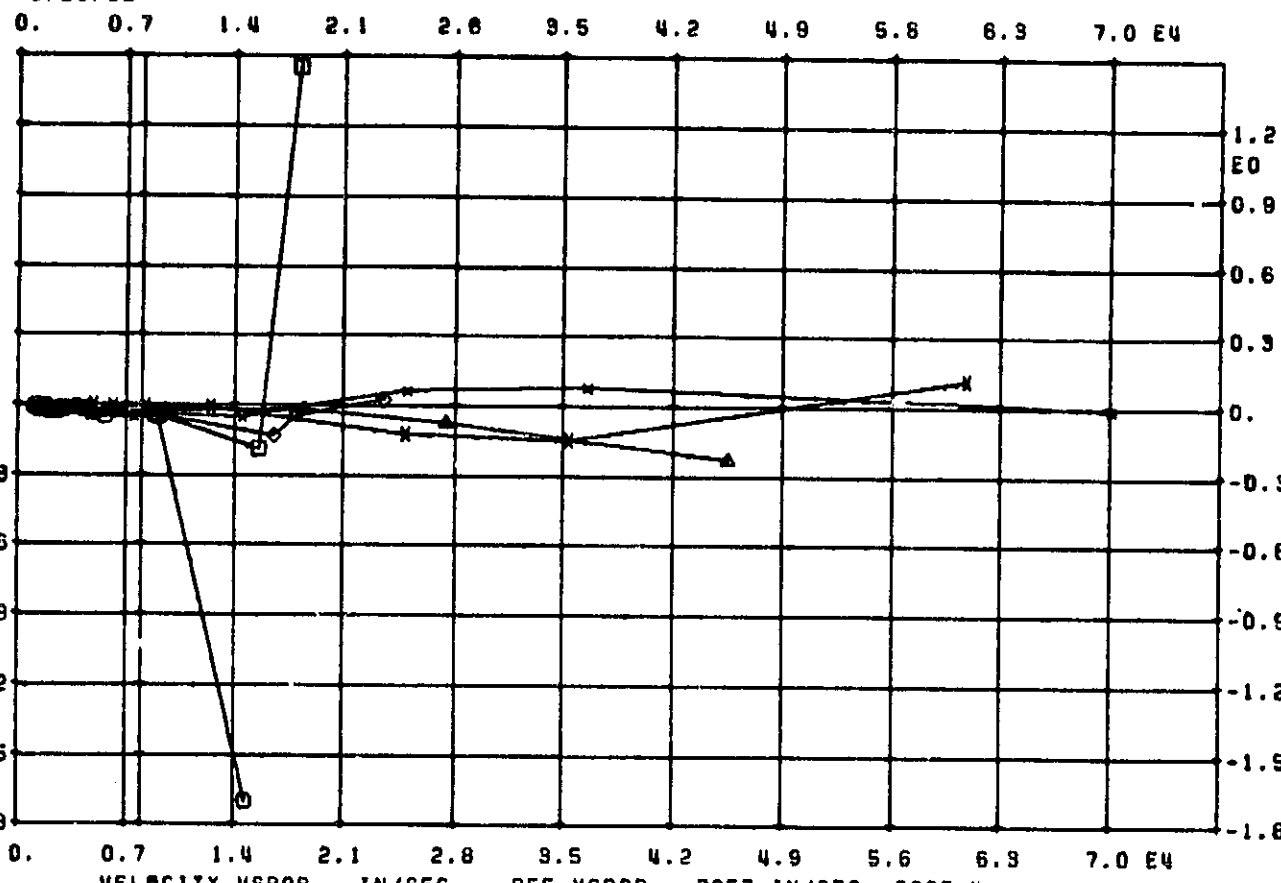
SOL 9 READ,K 0 MODES AND FLUTTER

Figure 47. V-g, V-f Curves, Case 4

2

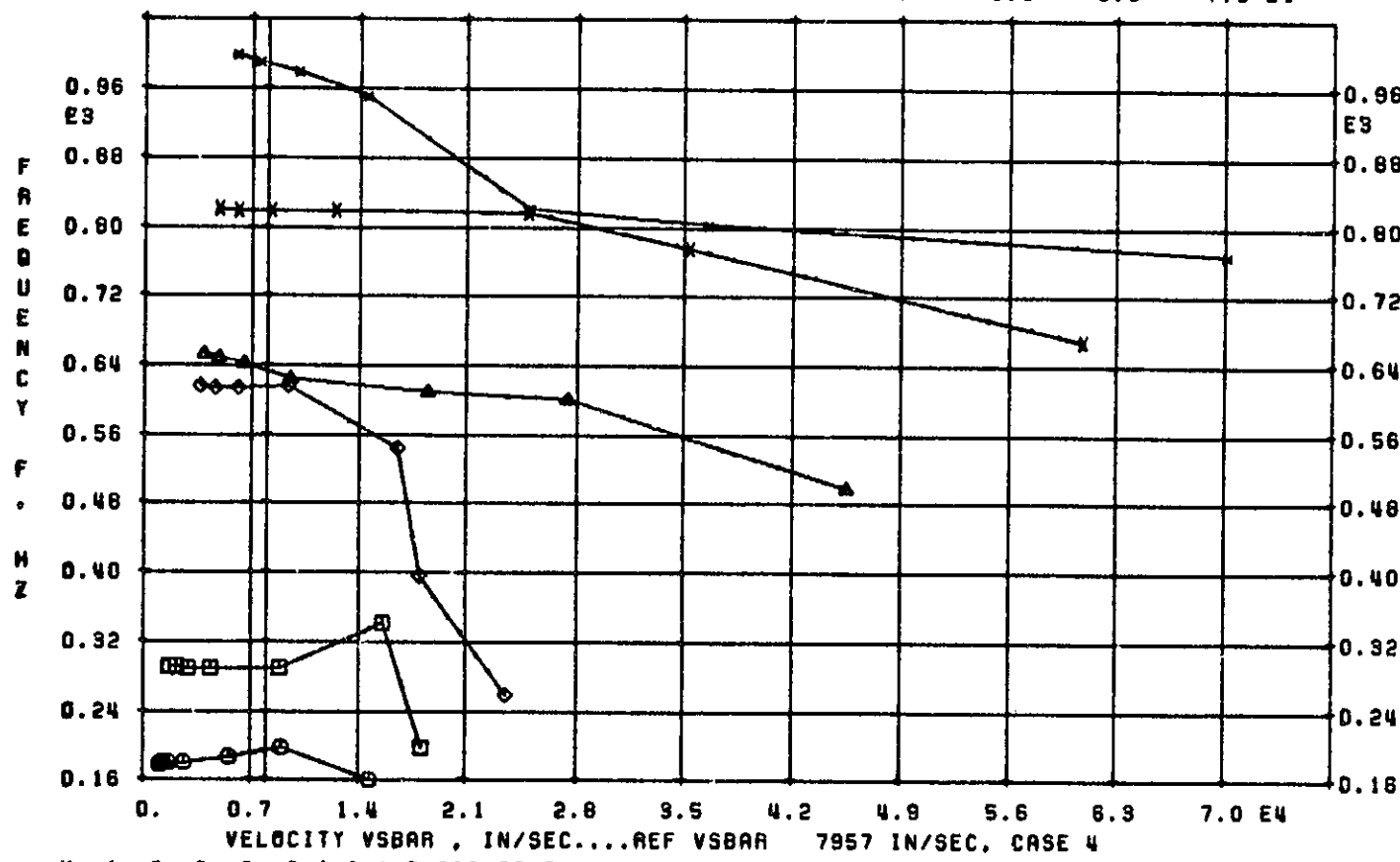
9/26/82

2



0. 0.7 1.4 2.1 2.8 3.5 4.2 4.9 5.6 6.3 7.0 E4

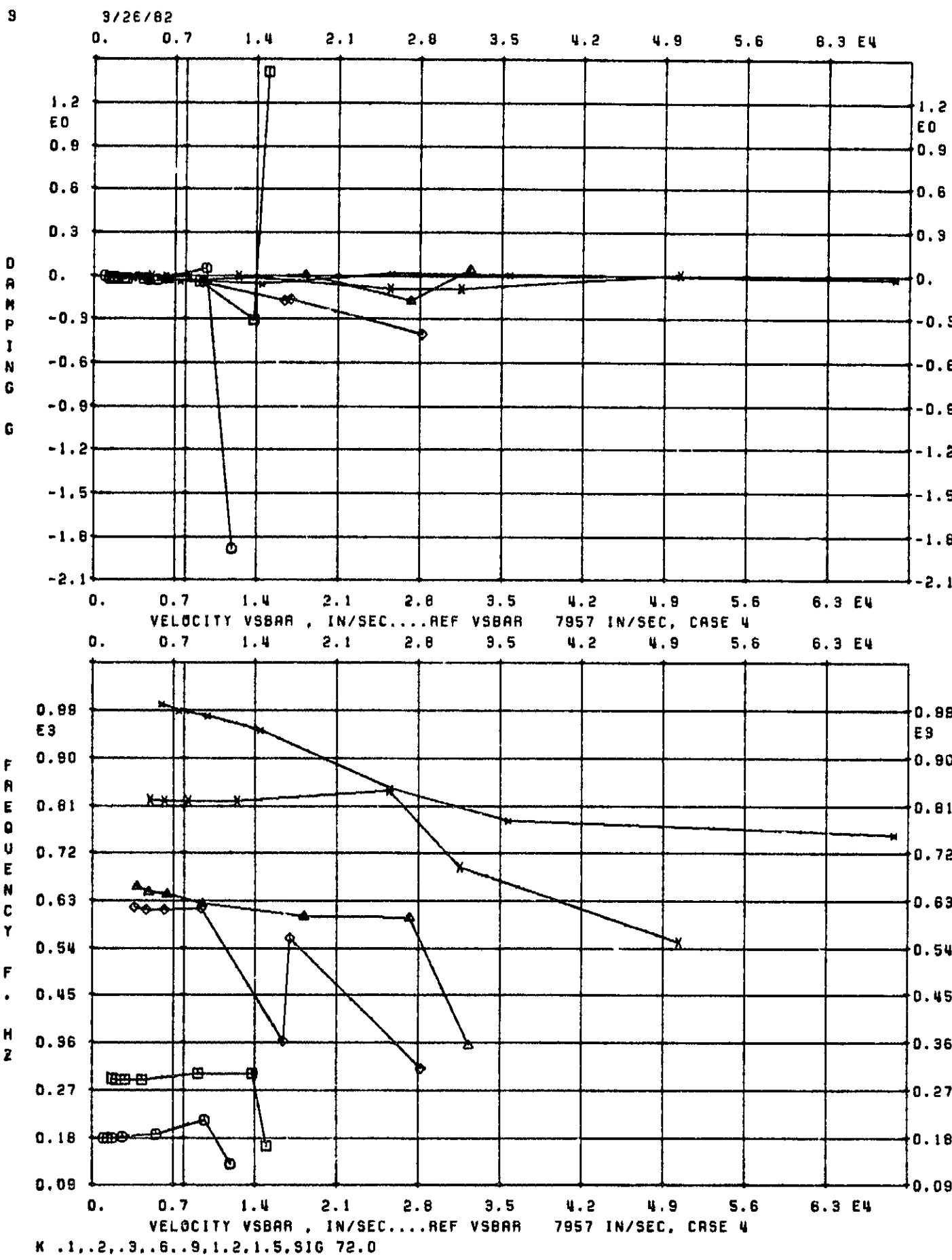
VELOCITY V_{BAR}, IN/SEC...REF V_{BAR} 7957 IN/SEC, CASE 4



K .1..2..9..6..9.1.2.1.5.SIG 36.0

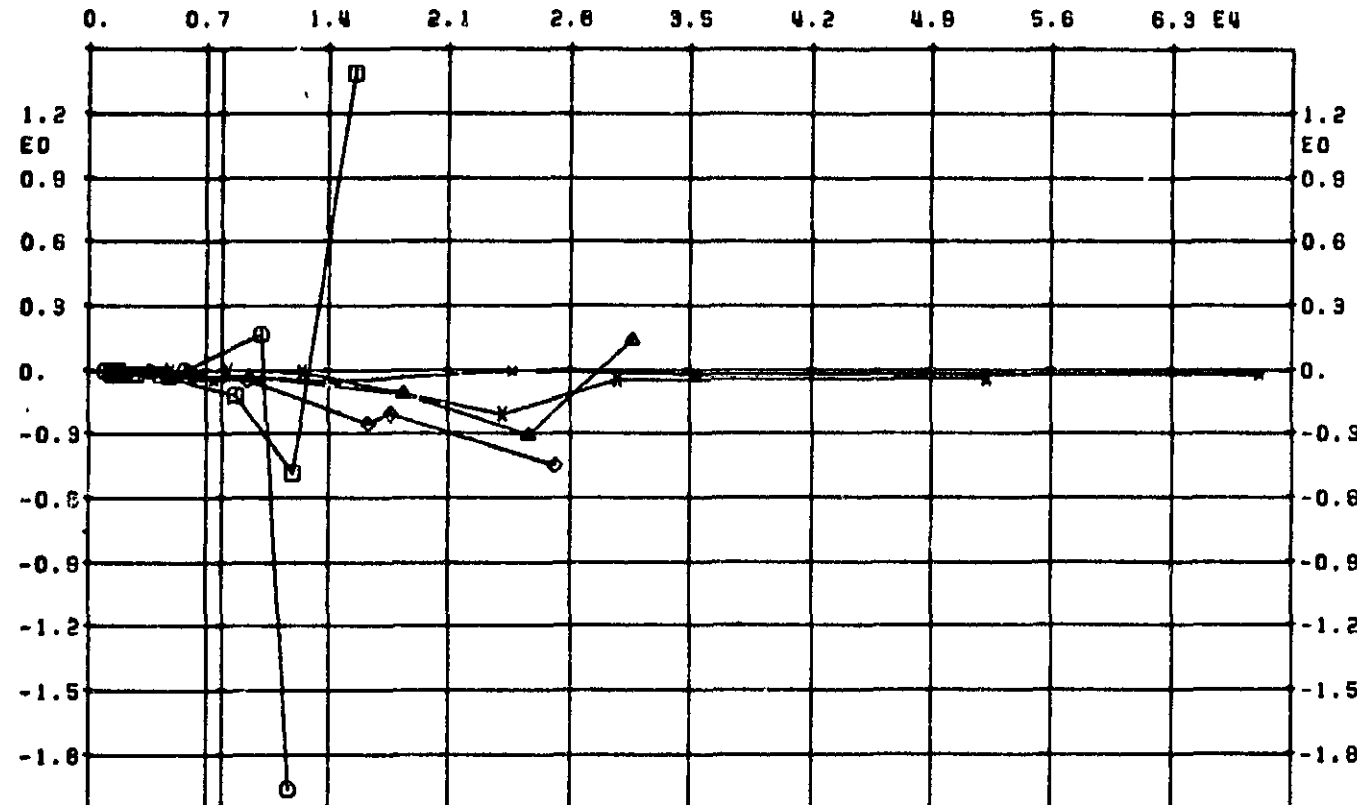
SOL 9 AERO,K 0 MODES AND FLUTTER

Figure 48. V-g, V-f Curves, Case 4

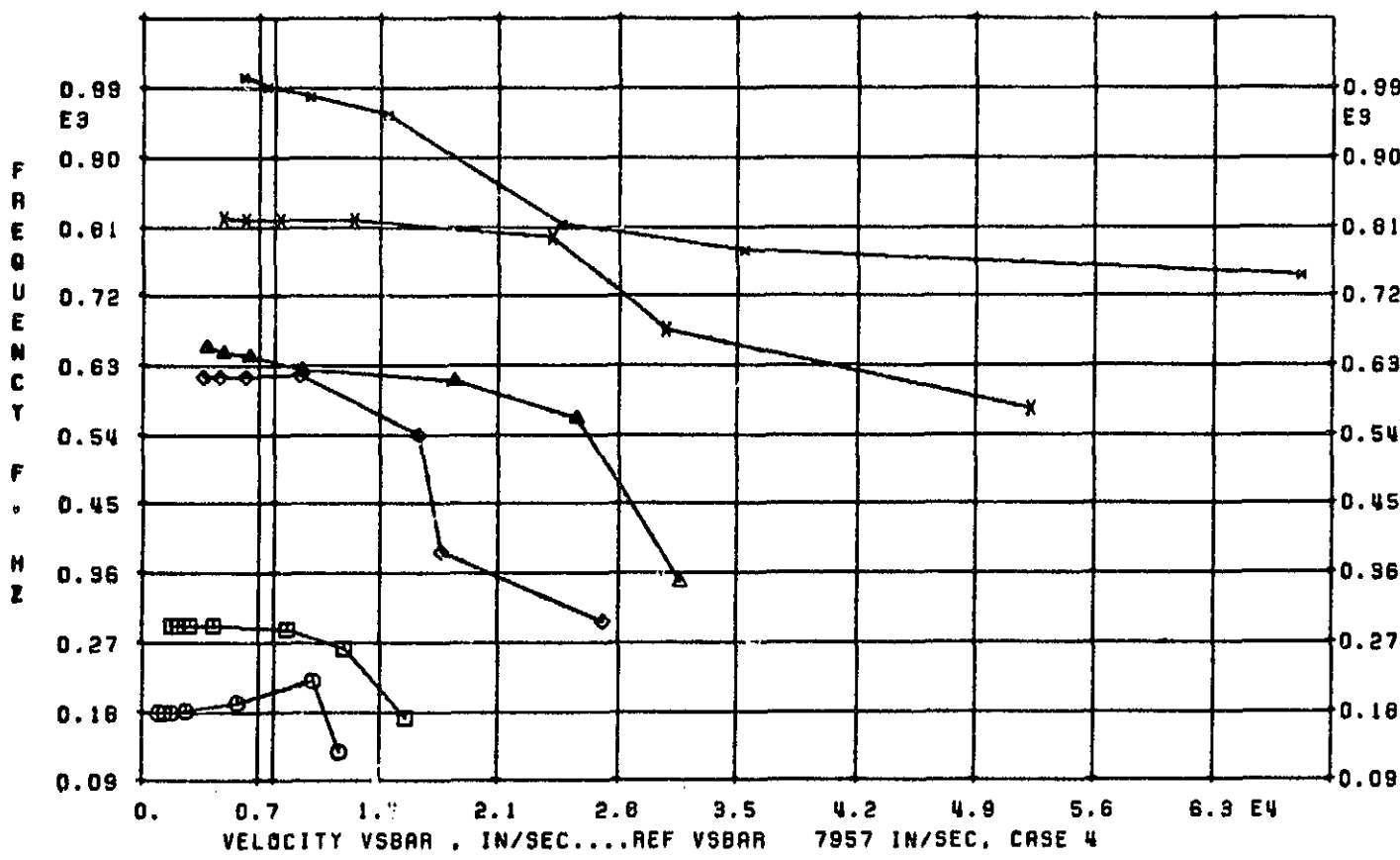


ORIGINAL PAGE IS
OF POOR QUALITY

9/26/82



VELOCITY VSBAR , IN/SEC....REF VSBAR 7957 IN/SEC. CASE 4



K .1..2..9..6..9.1.2.1.5.SIG 108.0
SQL 8 AERO,K 0 MODES AND FLUTTER

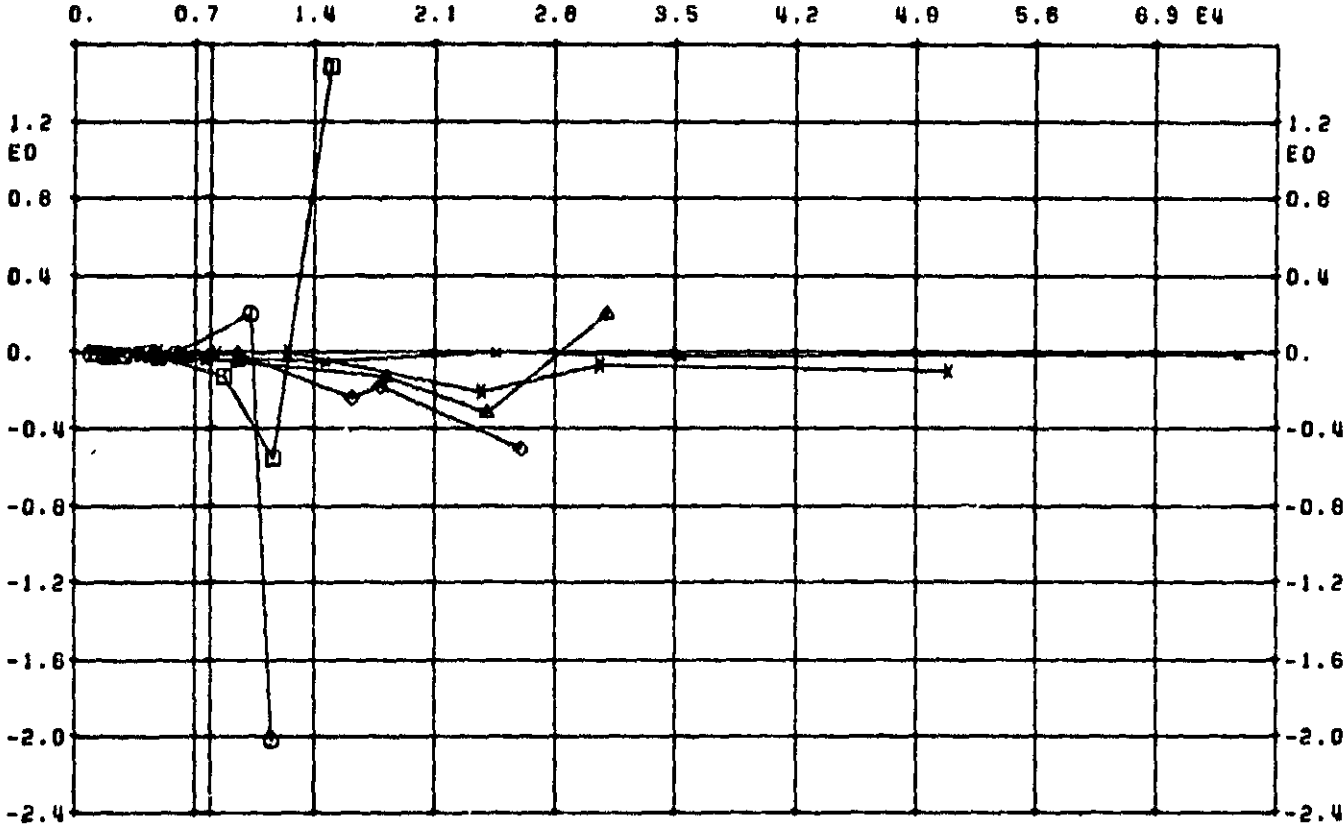
Figure 50. V-g, V-f Curves, Case 4

ORIGINAL PAGE IS
OF POOR QUALITY

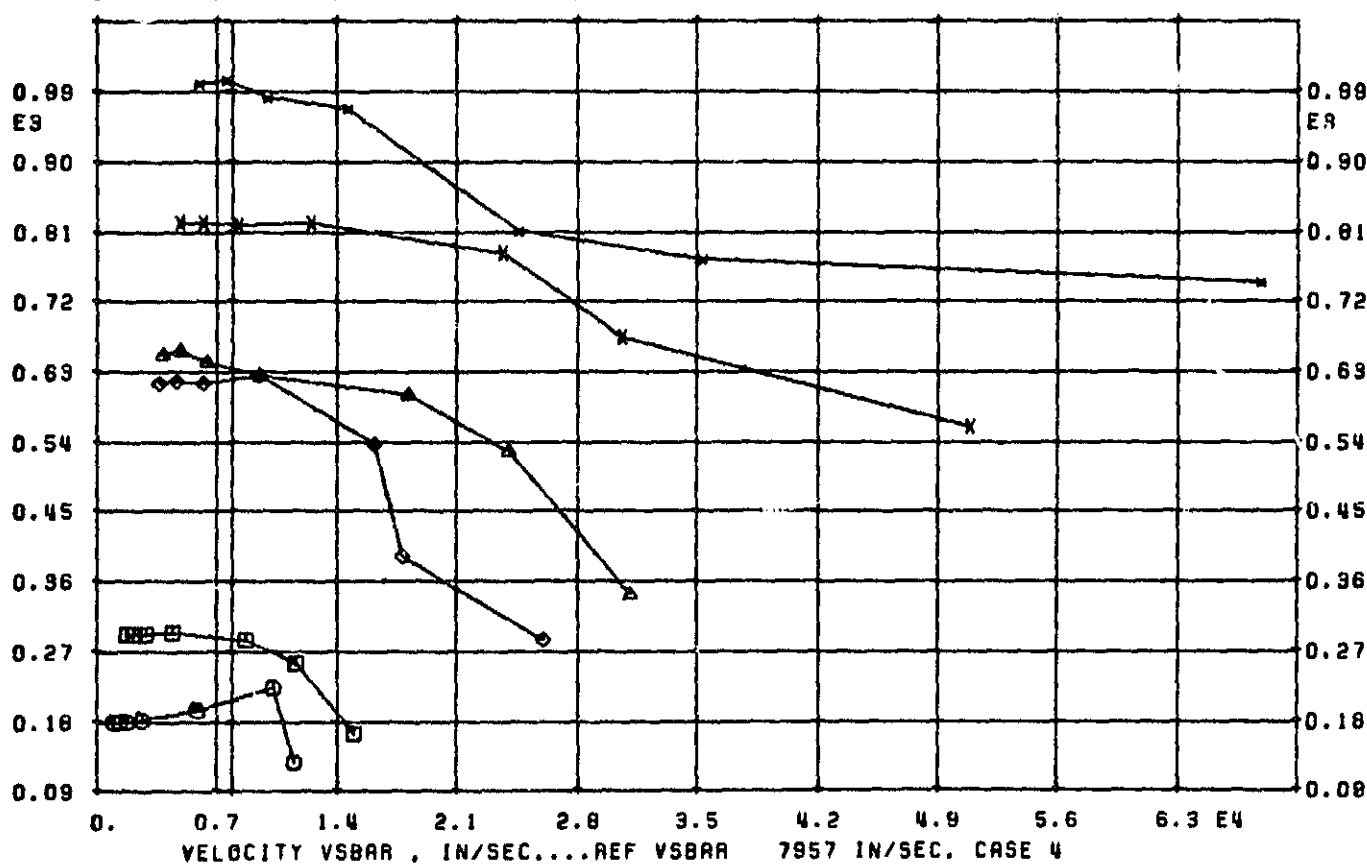
5

5

9/26/82



0. 0.7 1.4 2.1 2.8 3.5 4.2 4.9 5.6 6.3 E4



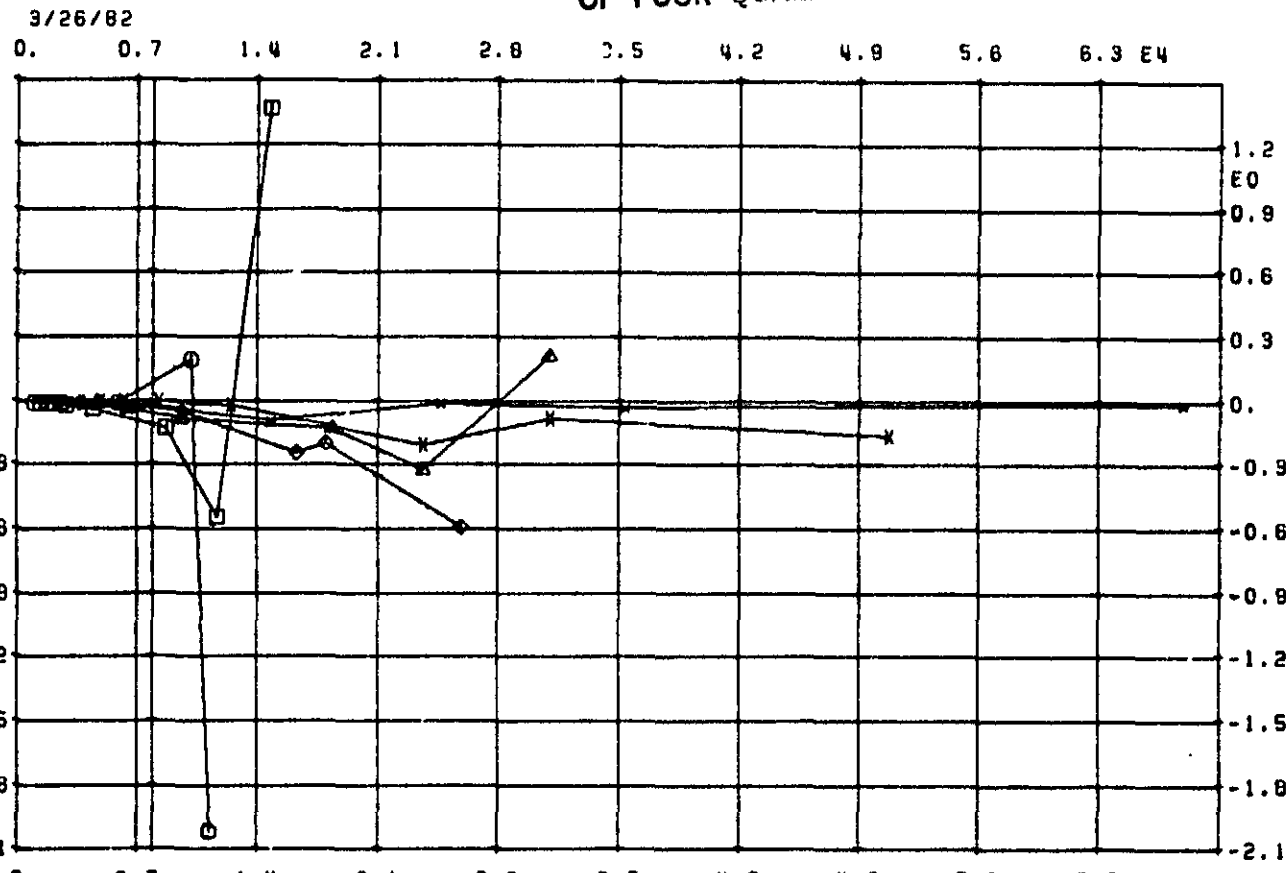
K .1..2..3..6..9.1.2.1.5.SIG 144.0
SOL 9 AERO,K 0 MODES AND FLUTTER

Figure 51. V- ζ , V-f Curves, Case 4

ORIGINAL PAGE IS
OF POOR QUALITY

6

2



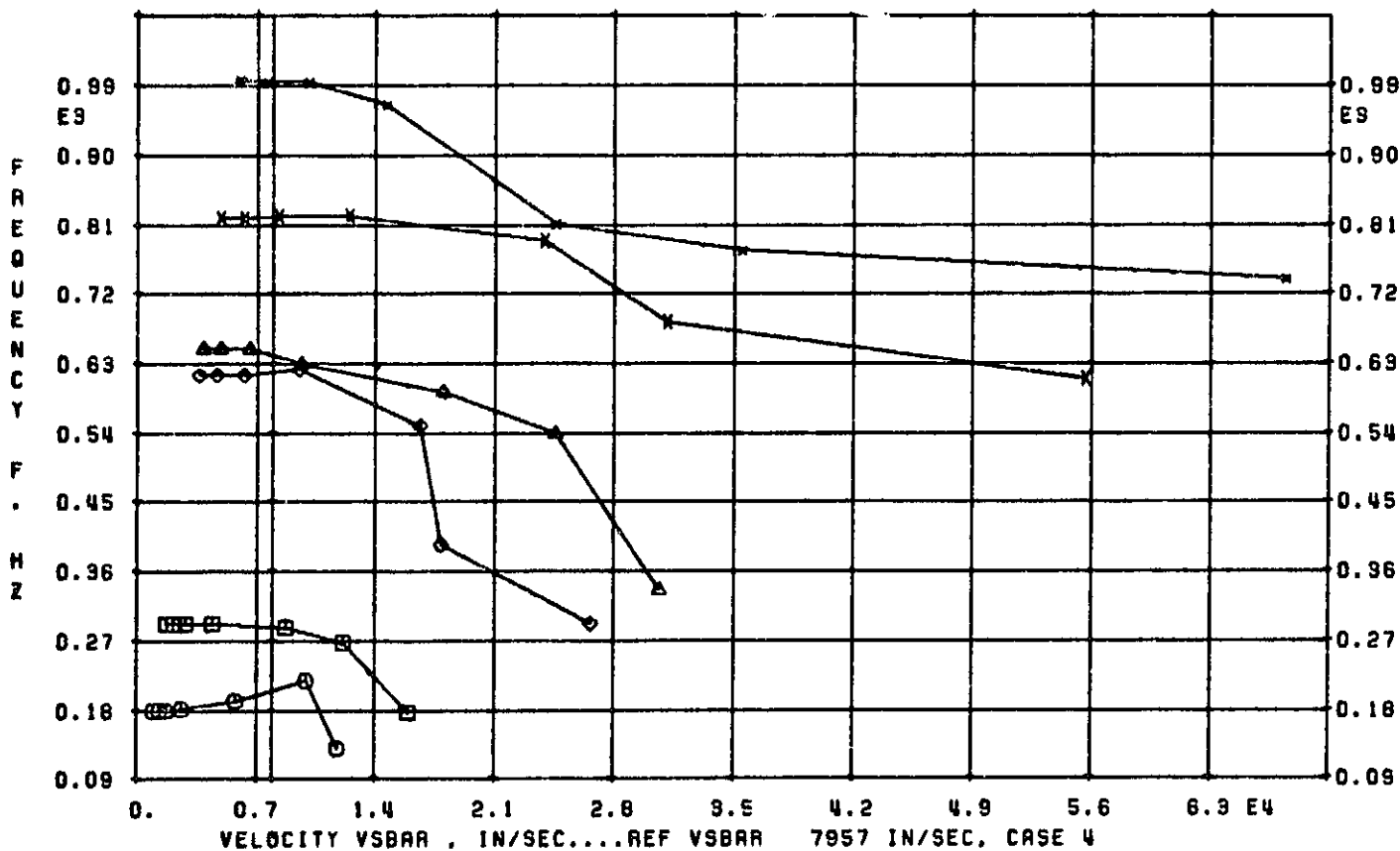
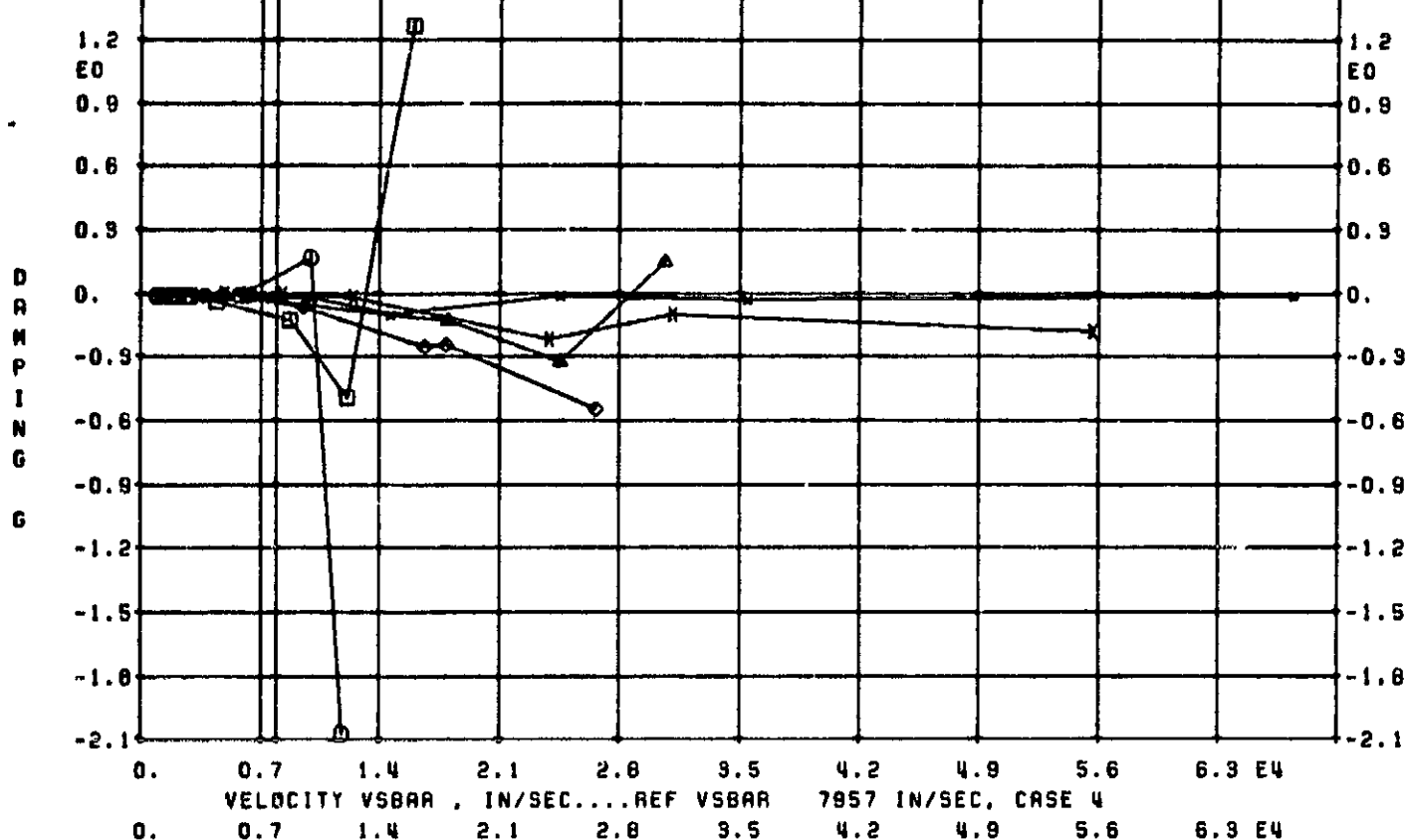
0.7 1.4 2.1 2.8 3.5 4.2 4.9 5.
VELOCITY VSBAR , IN/SEC....REF VSBAR 7957 IN/SEC. CASE 4

K .1.,.2.,.3.,.6.,.9,1.2,1.5,SIG 180.0
SOL 8 AERO,K 0 MODES AND FLUTTER

Figure 52. V-g, V-f Curves, Case 4

ORIGINAL PAGE IS
OF POOR QUALITY

7 9/28/82
0. 0.7 1.4 2.1 2.8 3.5 4.2 4.9 5.6 6.3 E4



K .1,.2,.3,.6,.9,1.2,1.5,SIG -144.0

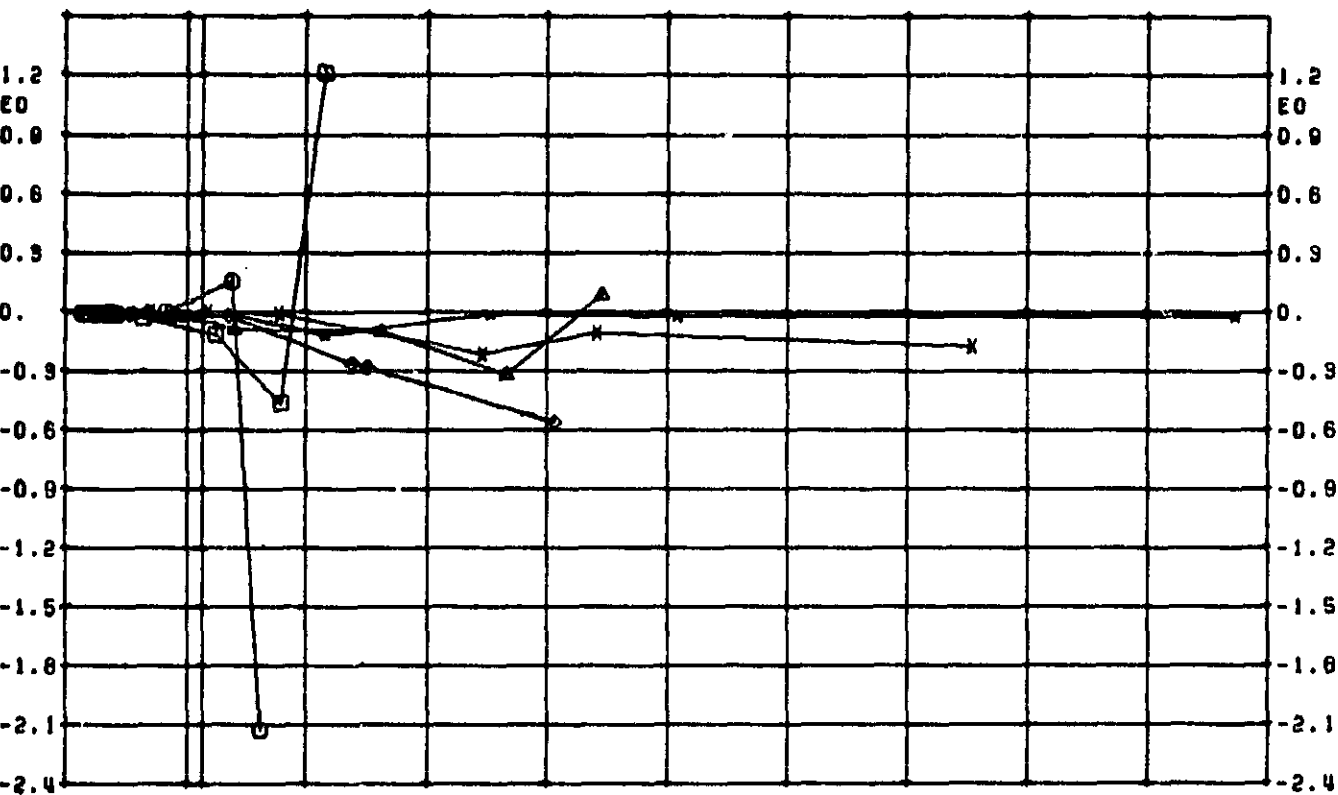
SOL 9 AERO,K 0 MODES AND FLUTTER

Figure 53. V-g, V-f Curves, Case 4

ORIGINAL PAGE IN
OF POOR QUALITY

8/26/62

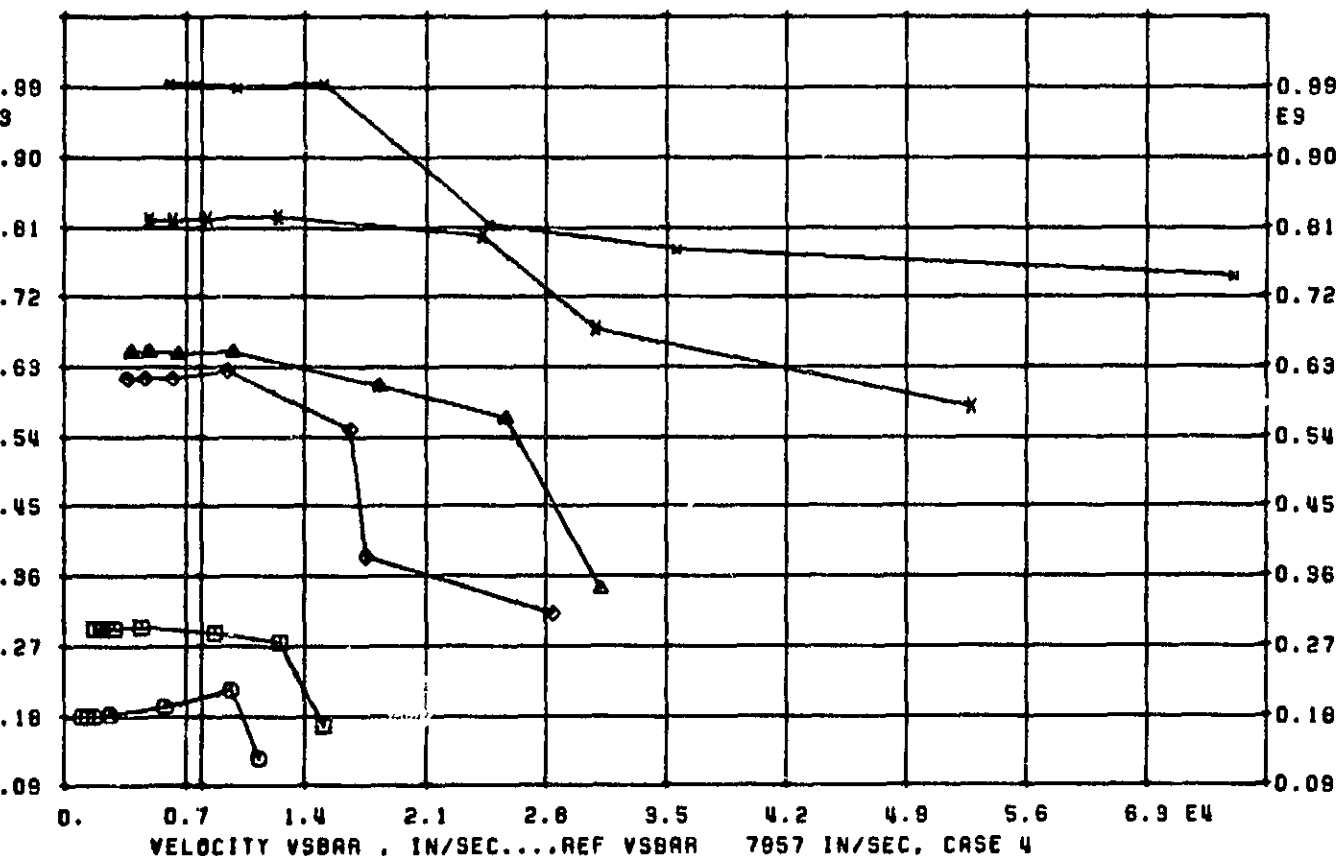
0. 0.7 1.4 2.1 2.8 9.5 4.2 4.9 5.6 6.9 E4



0. 0.7 1.4 2.1 2.8 9.5 4.2 4.9 5.6 6.9 E4

VELOCITY VSBAR , IN/SEC....REF VSBAR 7857 IN/SEC, CASE 4

0. 0.7 1.4 2.1 2.8 9.5 4.2 4.9 5.6 6.9 E4



K .1..2..3..6..8.1.2.1.5.SIG -108.0

SOL 9 AERO,K 0 MODES AND FLUTTER

Figure 54. V-g, V-f Curves, Case 4

ORIGINAL PAGE IS
OF POOR QUALITY

9

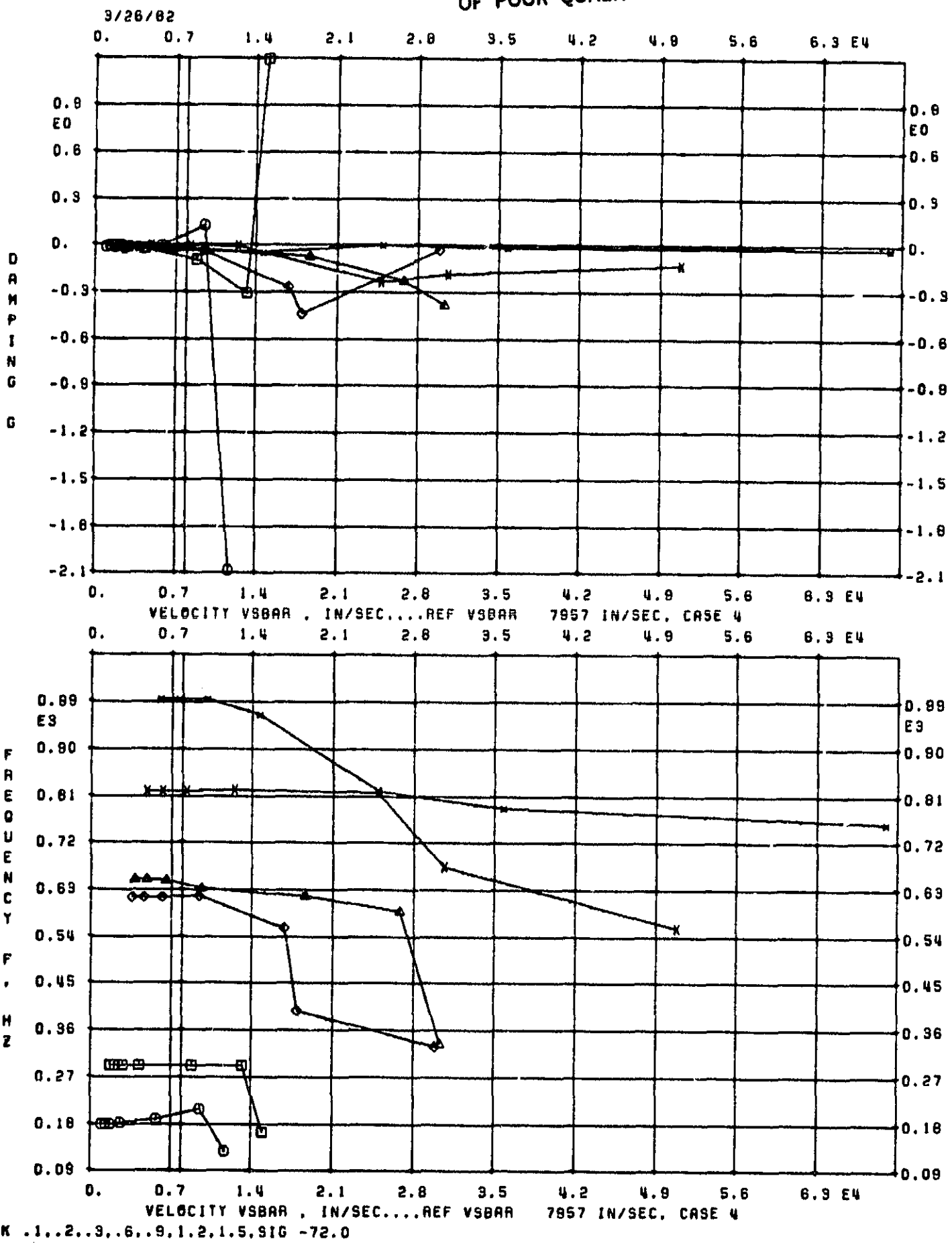


Figure 55. V-g, V-f Curves, Case 4

ORIGINAL PAGE IS
OF POOR QUALITY

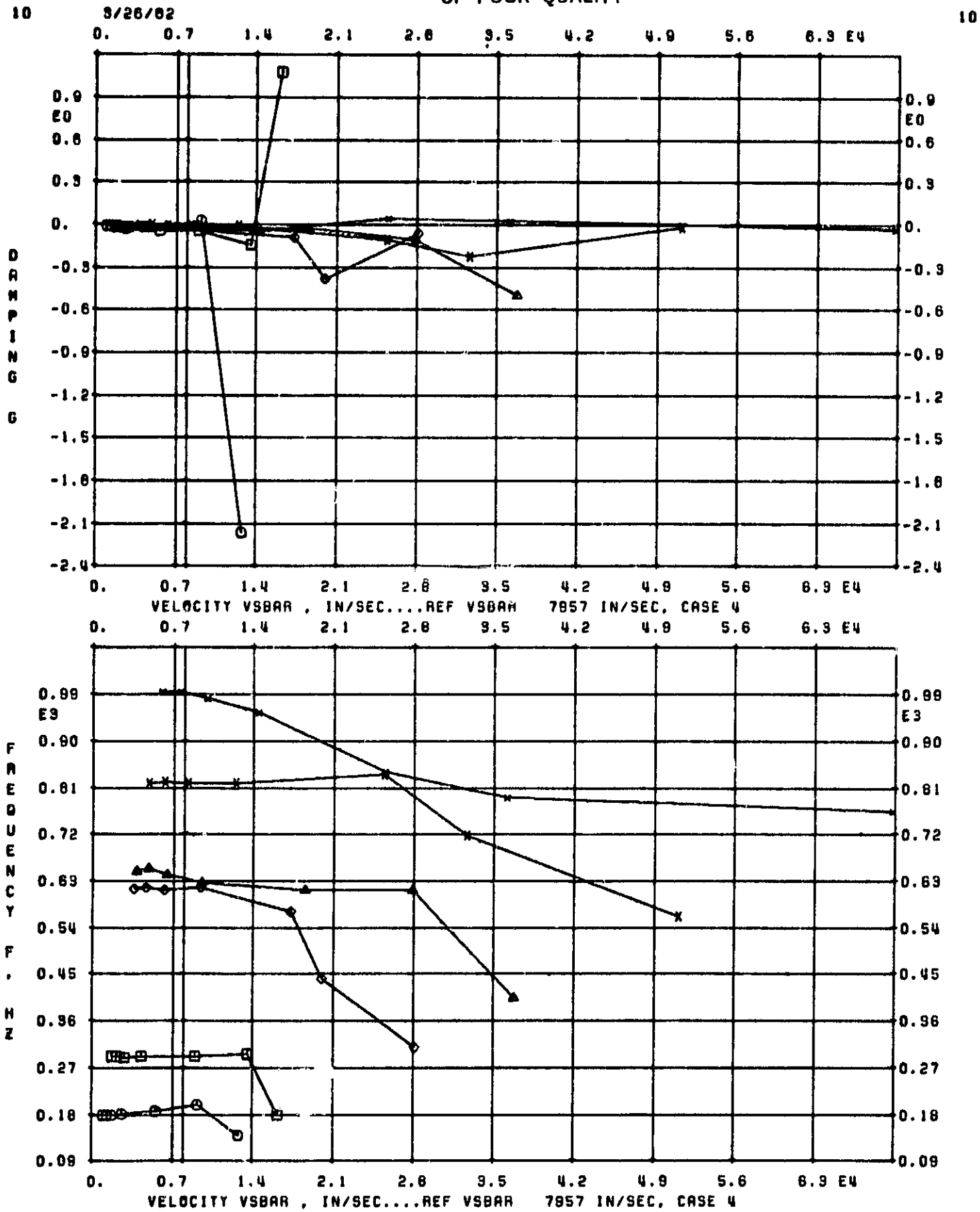


Figure 56. V-g, V-f Curves, Case 4

2. At the given operating conditions, only mode 1 (first bending mode represented by the symbol \odot) shows instability for a limited number of inter-blade phase angles. The degree of instability, $+g$, varies with the inter-blade phase angle.

3. The critical reduced frequency lies between 0.2 and 0.3.

For each of the four cases at their respective operating conditions, Tables 7 through 10 summarize the root locus of the first bending mode with inter-blade phase angle as the parameter. A non-dimensional frequency,

$$\nu = f/f_{\text{vacuum}}, \text{ and}$$

a non-dimensional damping,

$$\mu = (g/2) \cdot \nu$$

have been defined to plot the root locus shown in Figures 57 through 60 (represented by the symbol \odot).

In these figures, though the results are valid only at the discrete inter-blade phase angles identified by symbols, 'smooth' curves have been drawn for clarity of presentation. The curve-fitting routine used for plotting these curves was supplied with the zero inter-blade phase angle as the starting and end points to define the closed loops, and explains the sudden change in curvature about that point.

With regards to Figures 57 through 60, it is observed that:

1. The number of inter-blade phase angles for which the first bending mode is unstable, varies from case to case.
2. Since the $\mu=0$ line represents neutral equilibrium, the degree of instability indicated by the positive values of μ can be used to estimate the location of the flutter boundary. Of the 10-bladed propeller cases (2, 3 and 4), cases 3 and 4 seem to be closest to and farthest from the flutter boundary.
3. For the 10-bladed propeller, the root behavior at $\sigma=72^\circ$ is more sensitive to changes in operating conditions than at other inter-blade phase angles.

TABLE 7. ROOT LOCUS RESULTS FOR FIRST BENDING MODE, CASE 1

 $V_{s,ref} = 8061 \text{ in/sec.}$ $f_{vac.} = 189.4 \text{ Hz}$

Inter-blade Phase Angle, σ deg.	Reduced Frequency, $k_{s,ref}$	Frequency, f Hz.	Damping, g	Non-dim. Frequency, $v = f/f_{vac.}$	Non-dim. Damping, $\mu = (g/2) \cdot v$
0	.248	218.1	-5.143E-2	1.152	-2.961E-2
72	.248	218.5	-3.202E-2	1.154	-1.847E-2
144	.244	215.0	5.393E-2	1.135	3.061E-2
-144	.246	216.4	6.440E-2	1.143	3.679E-2
-72	.237	209.1	-2.781E-2	1.104	-1.535E-2

TABLE 8. ROOT LOCUS RESULTS FOR FIRST BENDING MODE, CASE 2

 $V_{s,\text{ref}} = 7495 \text{ in/sec}$ $f_{\text{vac.}} = 175.9 \text{ Hz.}$

Inter-blade Phase Angle, α deg.	Reduced Frequency, $k_{s,\text{ref}}$	Frequency, f Hz.	Damping, η	Non-dim. Frequency, $v = f/f_{\text{vac.}}$	Non-dim. Damping, $\mu = (g/2) \cdot v$
0	.234	192.3	-8.839E-2	1.093	-4.832E-2
36	.235	192.6	-8.007E-2	1.095	-4.384E-2
72	.242	198.4	1.698E-2	1.128	9.576E-3
108	.246	201.8	-6.165E-3	1.147	-3.536E-3
144	.248	203.2	1.980E-3	1.155	1.144E-3
180	.247	202.6	1.208E-2	1.152	6.957E-3
-144	.245	201.0	1.823E-2	1.143	1.042E-2
-108	.242	198.6	1.862E-2	1.129	1.051E-2
-72	.238	195.8	1.269E-2	1.113	7.063E-3
-36	.226	185.0	4.207E-3	1.052	2.212E-3

TABLE 9. ROOT LOCUS RESULTS FOR FIRST BENDING MODE, CASE 3

$$V_{\bar{s},\text{ref}} = 7046 \text{ in/sec}$$

$$f_{\text{vac}} = 187.9 \text{ Hz}$$

Inter-blade Phase Angle, σ deg.	Reduced Frequency, $k_{\bar{s},\text{ref}}$	Frequency, f Hz.	Damping, g	Non-dim. Frequency, $v = f/f_{\text{vac}}$	Non-dim. Damping, $\mu = (g/2) \cdot v$
0	.265	204.3	-8.380E-2	1.087	-4.556E-2
36	.267	205.8	-7.275E-2	1.095	-3.984E-2
72	.274	210.8	7.761E-3	1.122	1.353E-3
108	.277	213.5	-1.253E-2	1.136	-7.119E-3
144	.277	213.9	-5.829E-3	1.138	-3.318E-3
180	.278	214.3	4.364E-3	1.141	2.489E-3
-144	.277	213.5	8.805E-3	1.136	5.002E-3
-108	.273	210.6	1.001E-2	1.121	5.610E-3
-72	.270	207.8	5.903E-4	1.106	3.264E-4
-36	.258	198.9	-1.715E-2	1.059	-9.077E-3

TABLE 10. ROOT LOCUS RESULTS FOR FIRST BENDING MODE, CASE 4

$$v_{s,\text{ref}} = 7957 \text{ in/sec}$$

$$f_{\text{vac.}} = 179.0 \text{ Hz}$$

Inter-blade Phase Angle, σ deg.	Reduced Frequency, $k_{s,\text{ref}}$	Frequency, f Hz.	Damping, g	Non-dim. Frequency, $v = f/f_{\text{vac.}}$	Non-dim. Damping, $\mu = (g/2) \cdot v$
0	.226	196.8	-8.708E-2	1.099	-4.787E-2
36	.227	197.9	-7.649E-2	1.106	-4.228E-2
72	.231	200.6	5.865E-2	1.121	3.286E-2
108	.238	207.0	3.336E-2	1.156	1.929E-2
144	.238	207.7	4.046E-2	1.160	2.347E-2
180	.239	208.0	4.301E-2	1.162	2.499E-2
-144	.236	205.4	5.309E-2	1.147	3.046E-2
-108	.233	203.2	4.962E-2	1.135	2.816E-2
-72	.230	200.1	3.800E-2	1.118	2.124E-2
-36	.217	189.3	-1.532E-2	1.058	-8.101E-3

SR-5 FLUTTER ANALYSIS AT 6900 RPM (5 BLADES)
 Figure 57. ROOT LOCUS OF FIRST BENDING MODE (FREQ IN VACUUM = 189.4 Hz.)

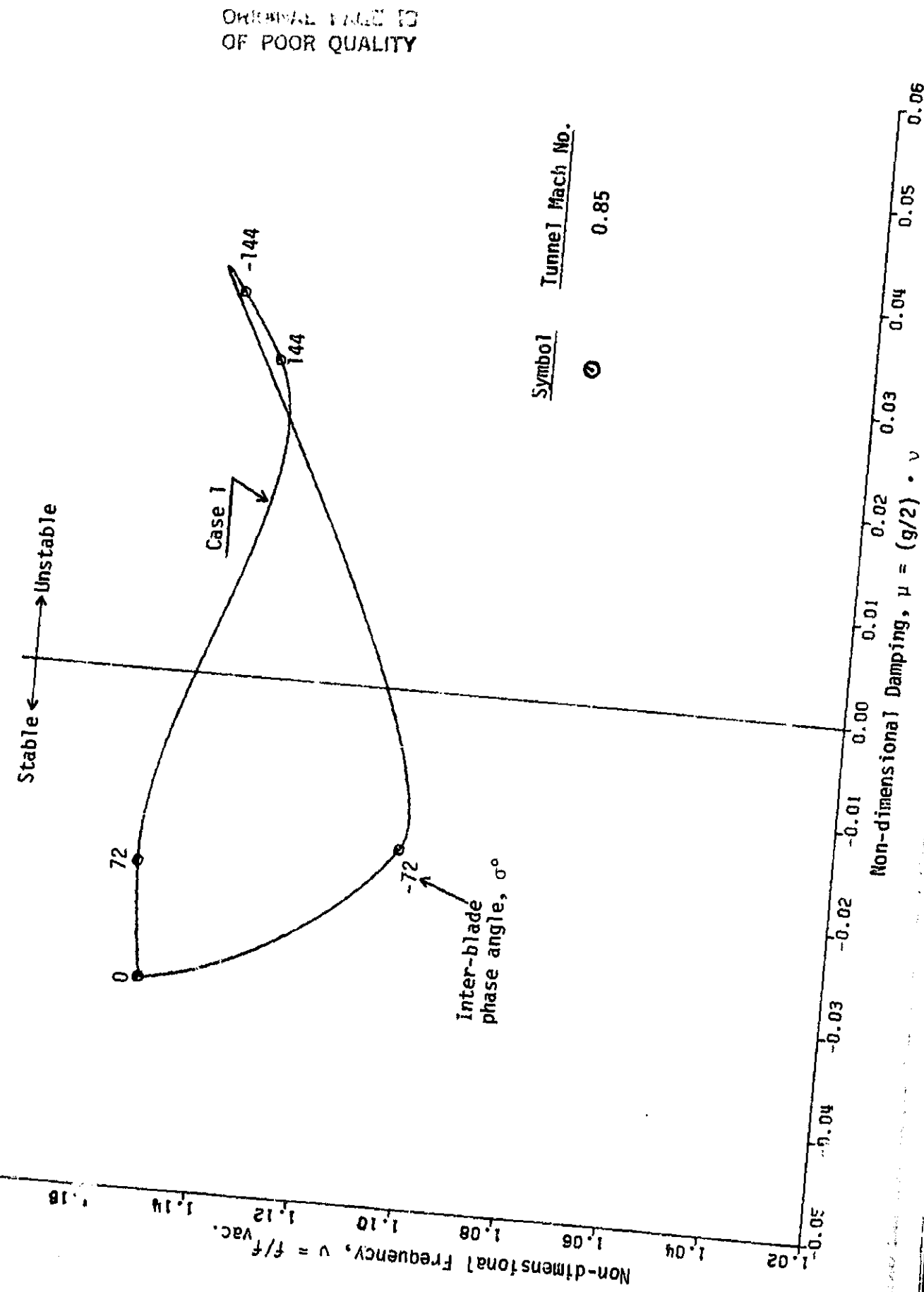
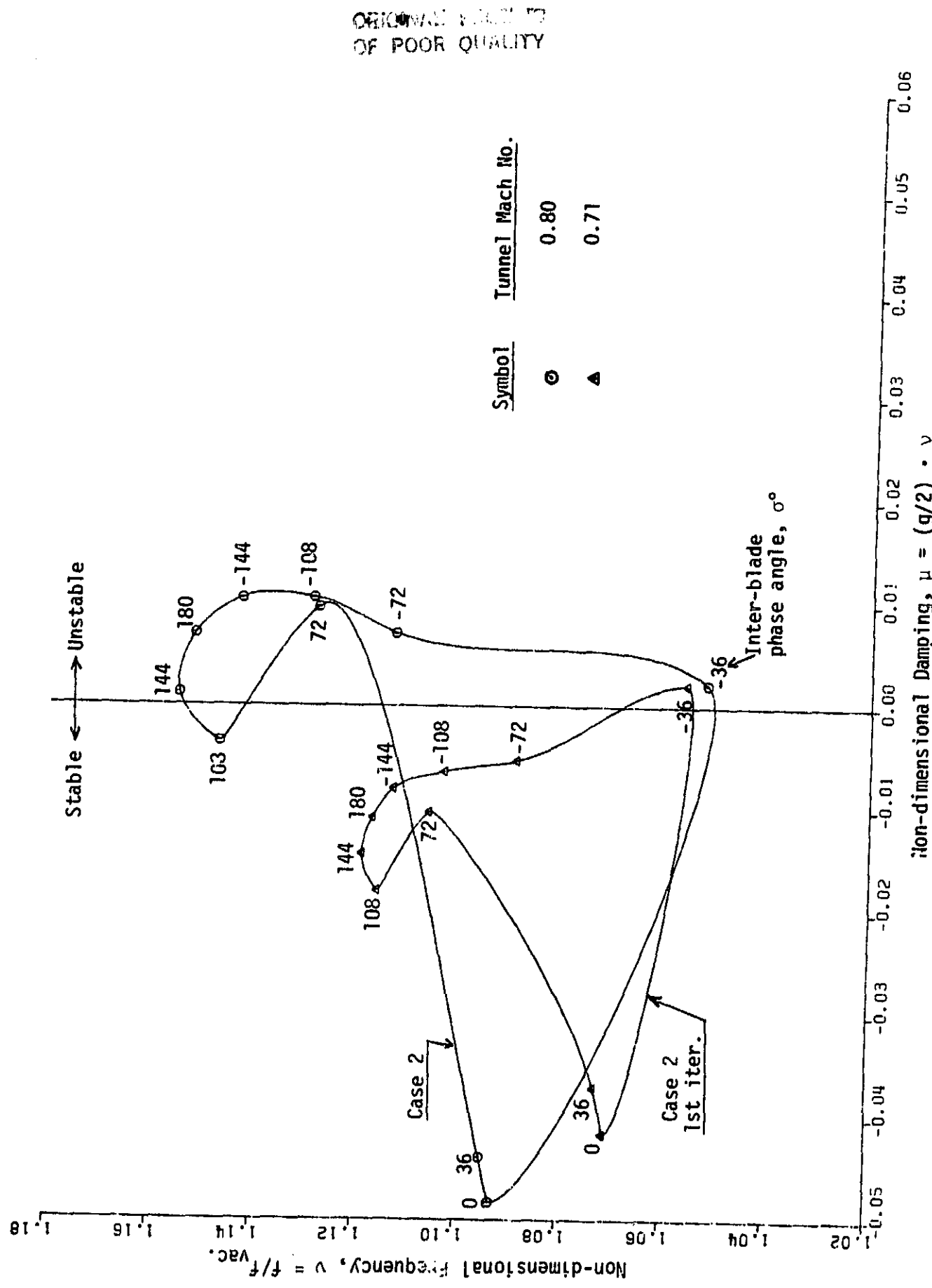
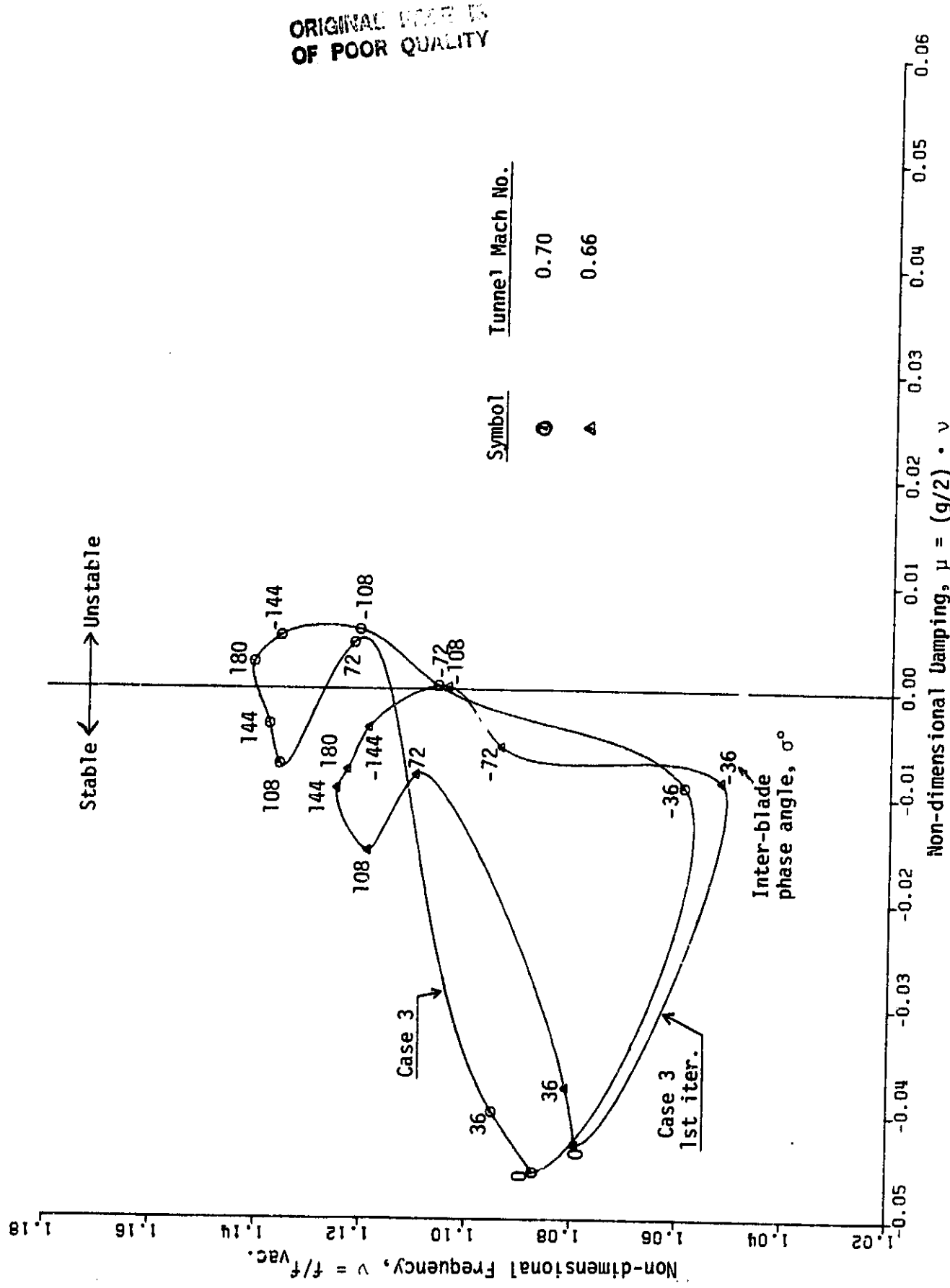


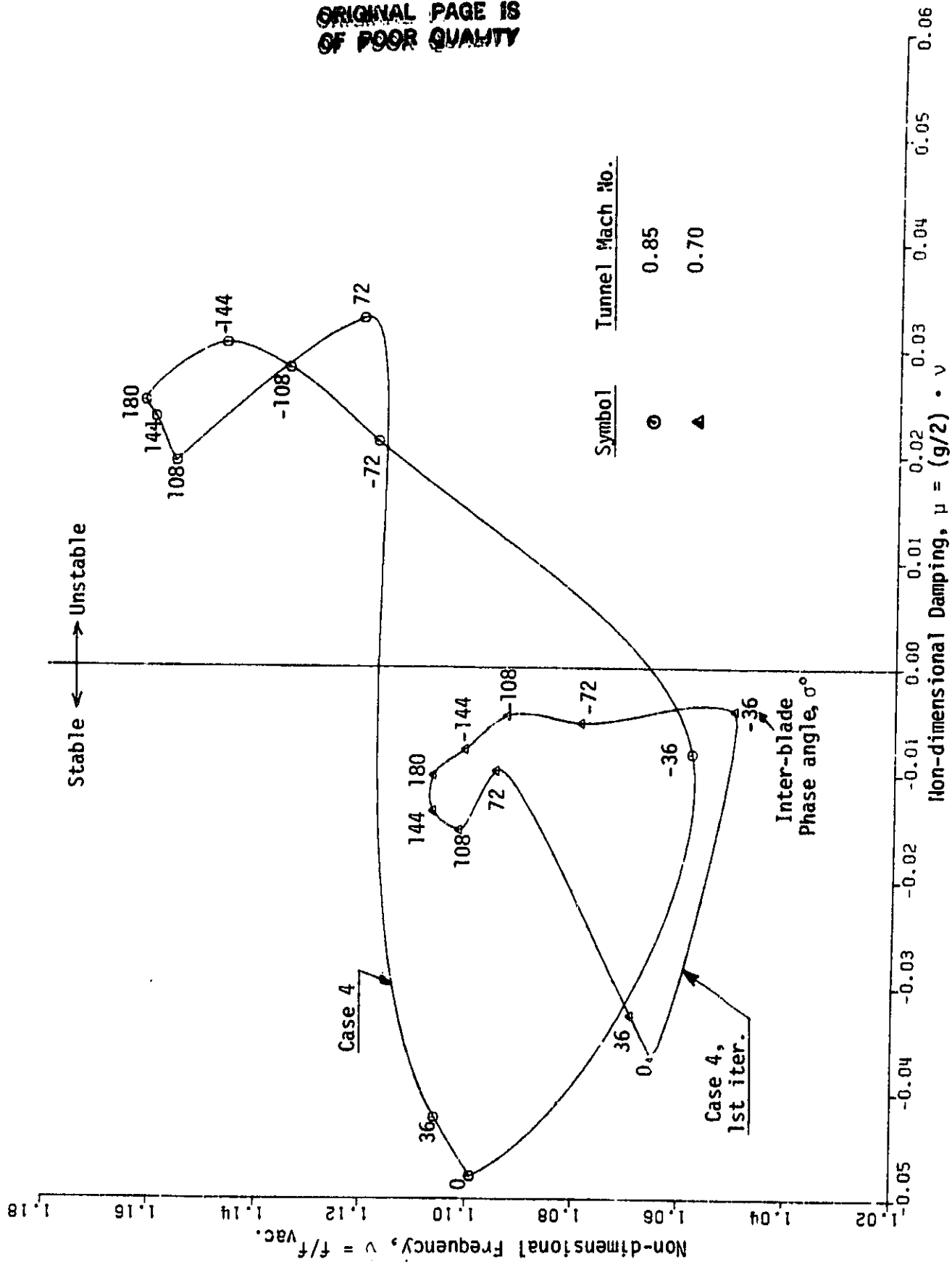
Figure 58. ROOT LOCUS OF FINES SENDING MODE (FREQ IN VACUUM = 175.9 Hz.)



SR-S FLUTTER ANALYSIS AT 6800 RPM (10 BLADES)
 Figure 59. ROOT LOCUS OF FIRST BENDING MODE (FREQ IN VACUUM = 187.9 Hz.)



SR-5 FLUTTER ANALYSIS AT 6200 RPM (10 BLADES)
 Figure 6Q ROOT LOCUS OF FIRST BENDING MODE (FREQ IN VACUUM = 179.0 Hz.)



To illustrate the remark 2 above, Table 11 has been prepared to estimate the operating conditions when g (and hence μ) is zero by considering similar inlet velocity triangles at the reference chord as shown in Figure 61.

For the 10-bladed propeller, based on the given operating conditions and those implied at $g=0$ from Table 11, three new operating conditions were selected (Table 12). In order to use the structural modes computed earlier for cases 2, 3 and 4, the propeller rpm's were unchanged while changing the tunnel Mach numbers.

Analysis of the results of these three 1st iteration cases, conducted similar to that discussed earlier in this section for cases 2, 3 and 4, also shows only mode 1 to be closest to neutral equilibrium. Results of these three 1st iteration cases are presented in Tables 13 through 15, Figures 58 through 60 (represented by the symbol Δ), and Table 11.

Figure 62 presents a summary of all the cases considered for the SR-5 five- and ten-bladed propeller flutter analysis. The subsonic classical flutter boundary predicted for the ten-bladed propeller using the analysis discussed in this report is also shown in this figure.

Figure 63 is presented to illustrate the excellent agreement between the analytical predictions of the present work and the experimental observations of NASA LeRC. The analytical predictions of Kaza and Kielb (Ref. 7), approximating the structural behavior of the SR-5 blades by simplified, constant-chord, constant-sweep equivalent beam model with cascade effects are also shown in this figure.

TABLE 11. IMPLIED OPERATING CONDITIONS AT $g=0$

Case	Free Stream Mach No., M_∞	RPM	Free Stream Velocity, (MA) in/sec	Relative Inflow Velocity $V_{s,ref}$ in/sec	Implied Inflow Velocity at $g=0$ $V_{s,ref} _{g=0}$ in/sec	Inter-blade phase Angle σ deg.	$x = \frac{V_{s,ref} _{g=0}}{V_{s,ref}}$	$x \cdot M_\infty$	$x \cdot RPM$
1	0.85	6900	10,940	8061	6123	-144	0.760	0.646	5241
2	0.80	6000	10,388	7495	6606	72	0.881	0.705	5288
3	0.70	6800	9,336	7046	6470	-108	0.918	0.643	6244
4	0.85	6200	11,059	7957	5755	180	0.723	0.615	4484
2, 1st iter.	0.71	6000	9,220	6770	6732	-36	0.994	0.706	5966
3, 1st iter.	0.66	6800	8,803	6718	6704	-108	0.998	0.659	6786
4, 1st iter.	0.70	6200	9,108	6750	6839	-36	1.013	0.709	6282

Note: The implied operating conditions are obtained as follows:

1. $V_{s,ref}|_{g=0}$ is interpolated from the $V_{s,ref}-g$ curves (Figures)
2. Similar inlet velocity triangles at the reference chord are then used to determine the implied rpm and free stream Mach number (Figure).

ORIGINAL PAGE IS
OF POOR QUALITY

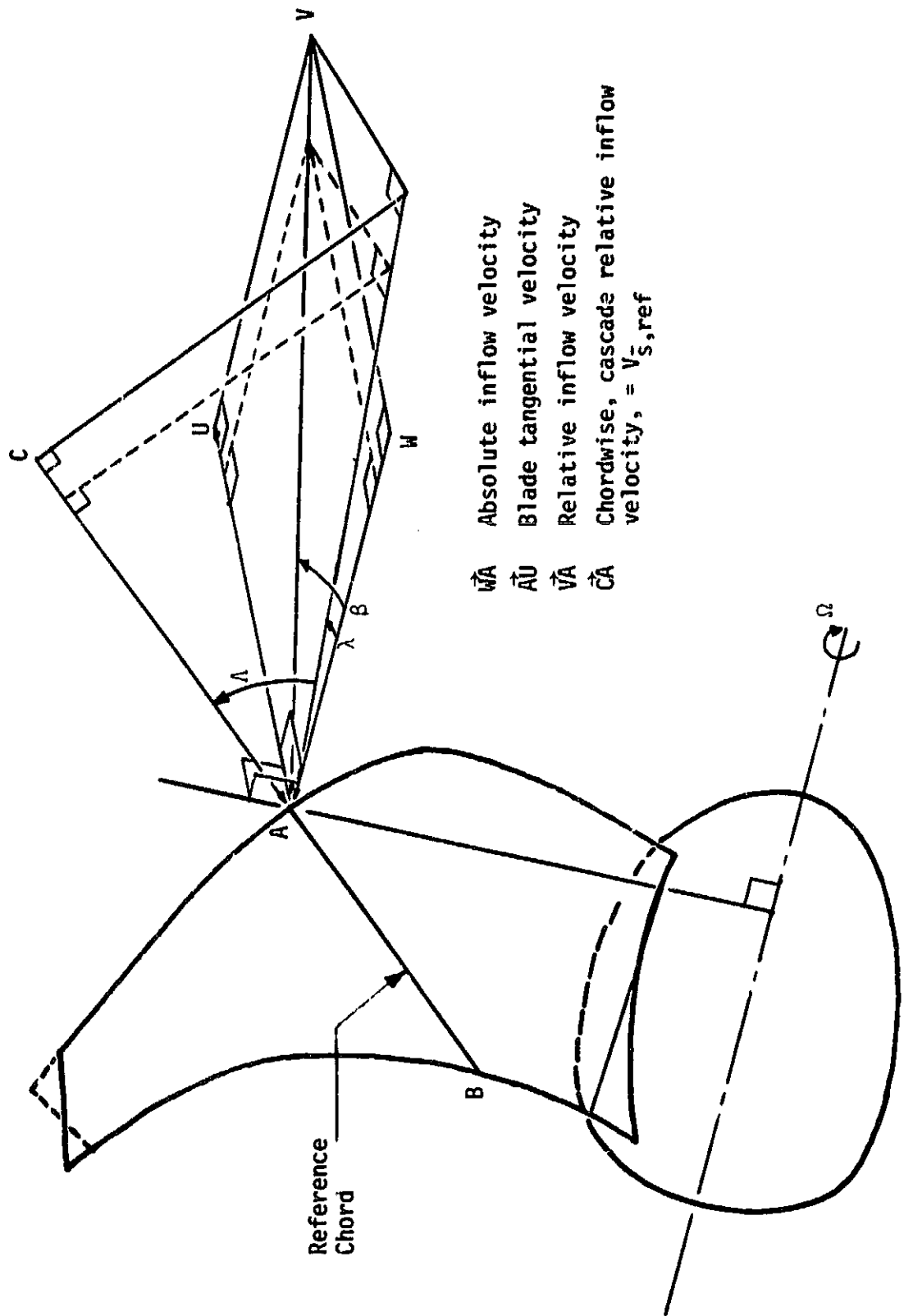


FIGURE 61. SIMILAR INLET VELOCITY TRIANGLES

TABLE 12. SR-5 OPERATING CONDITIONS FOR 1st ITERATION (10-BLADED PROPELLER)

Case No.	rpm	Blade Setting Angle	Free Stream Conditions		
			Velocity, ft/sec	Density, Slug/ft ³	Mach No., M_{∞}
2, 1st iter.	6000	69°	768.3	1.9534E-3	0.71
3, 1st iter.	6800	69°	733.6	2.0244E-3	0.66
4, 1st iter.	6200	69°	759.0	1.7756E-3	0.70

TABLE 13. ROOT LOCUS RESULTS FOR FIRST BENDING MODE, CASE 2, 1st ITERATION

$$V_{\bar{s}, \text{ref}} = 6770 \text{ in/sec.}$$

$$f_{\text{vac.}} = 175.9 \text{ Hz.}$$

Inter-blade Phase Angle, σ deg.	Reduced Frequency, $k_{\bar{s}, \text{ref}}$	Frequency, f Hz.	Damping, g	Non-dim. Frequency, $v = f/f_{\text{vac.}}$	Non-dim. Damping, $\mu = (g/2) \cdot v$
0	.254	188.4	-7.769E-2	1.071	-4.161E-2
36	.255	188.8	-6.895E-2	1.073	-3.700E-2
72	.262	194.6	-1.860E-2	1.106	-1.029E-2
108	.265	196.3	-3.214E-2	1.116	-1.793E-2
144	.266	196.9	-2.568E-2	1.119	-1.437E-2
180	.265	196.5	-1.951E-2	1.117	-1.090E-2
-144	.264	195.8	-1.441E-2	1.113	-8.020E-3
-108	.262	194.1	-1.158E-2	1.103	-6.389E-3
-72	.258	191.6	-9.723E-3	1.089	-5.295E-3
-36	.251	185.7	4.066E-3	1.056	2.146E-3

TABLE 14. ROOT LOCUS RESULTS FOR FIRST BENDING MODE, CASE 3, 1st ITERATION

$$V_{s,\text{ref}} = 6718 \text{ in/sec}$$

$$f_{\text{vac.}} = 187.9 \text{ Hz}$$

Inter-blade Phase angle, α deg.	Reduced Frequency, $k_{s,\text{ref}}$	Frequency, f Hz.	Damping, η	Non-dim. Frequency, $\nu = f/f_{\text{vac.}}$	Non-dim. damping, $\mu = (g/2) \cdot \nu$
0	.276	202.7	-7.971E-2	1.079	-4.299E-2
36	.276	203.1	-6.950E-2	1.081	-3.756E-2
72	.284	208.5	-1.454E-2	1.110	-8.067E-3
108	.286	210.2	-2.718E-2	1.119	-1.520E-2
144	.288	211.4	-1.666E-2	1.125	-9.372E-3
180	.287	211.0	-1.339E-2	1.123	-7.518E-3
-144	.286	210.3	-6.401E-3	1.119	-3.582E-3
-108	.282	207.4	4.289E-4	1.104	2.367E-4
-72	.279	205.6	-9.847E-3	1.094	-5.387E-3
-36	.269	197.6	-1.625E-2	1.052	-8.544E-3

TABLE 15. ROOT LOCUS RESULTS FOR FIRST BENDING MODE, CASE 4, 1st ITERATION

$$V_{s,\text{ref}} = 6750 \text{ in/sec}$$

$$f_{\text{vac.}} = 179.0 \text{ Hz}$$

Inter-blade Phase angle, σ deg.	Reduced Frequency, $k_{s,\text{ref}}$	Frequency, f Hz.	Damping, ζ	Non-dim. Frequency, $v = f/f_{\text{vac.}}$	Non-dim. damping, $\mu = (g/2) \cdot v$
0	.258	190.7	-6.859E-2	1.065	-3.654E-2
36	.259	191.4	-6.096E-2	1.069	-3.259E-2
72	.265	196.0	-1.769E-2	1.095	-9.685E-3
108	.267	197.3	-2.765E-2	1.102	-1.524E-2
144	.268	198.1	-2.444E-2	1.107	-1.352E-2
180	.268	198.1	-1.836E-2	1.107	-1.016E-2
-144	.267	197.1	-1.402E-2	1.101	-7.719E-3
-108	.265	195.6	-8.329E-3	1.093	-4.551E-3
-72	.261	193.1	-9.617E-3	1.079	-5.187E-3
-36	.254	187.9	-7.579E-3	1.050	-3.978E-3

C - 2

**Figure f2. SR-5 FLUTTER ANALYSIS SUMMARY
(5- AND 10-BLADED PROPELLERS)**

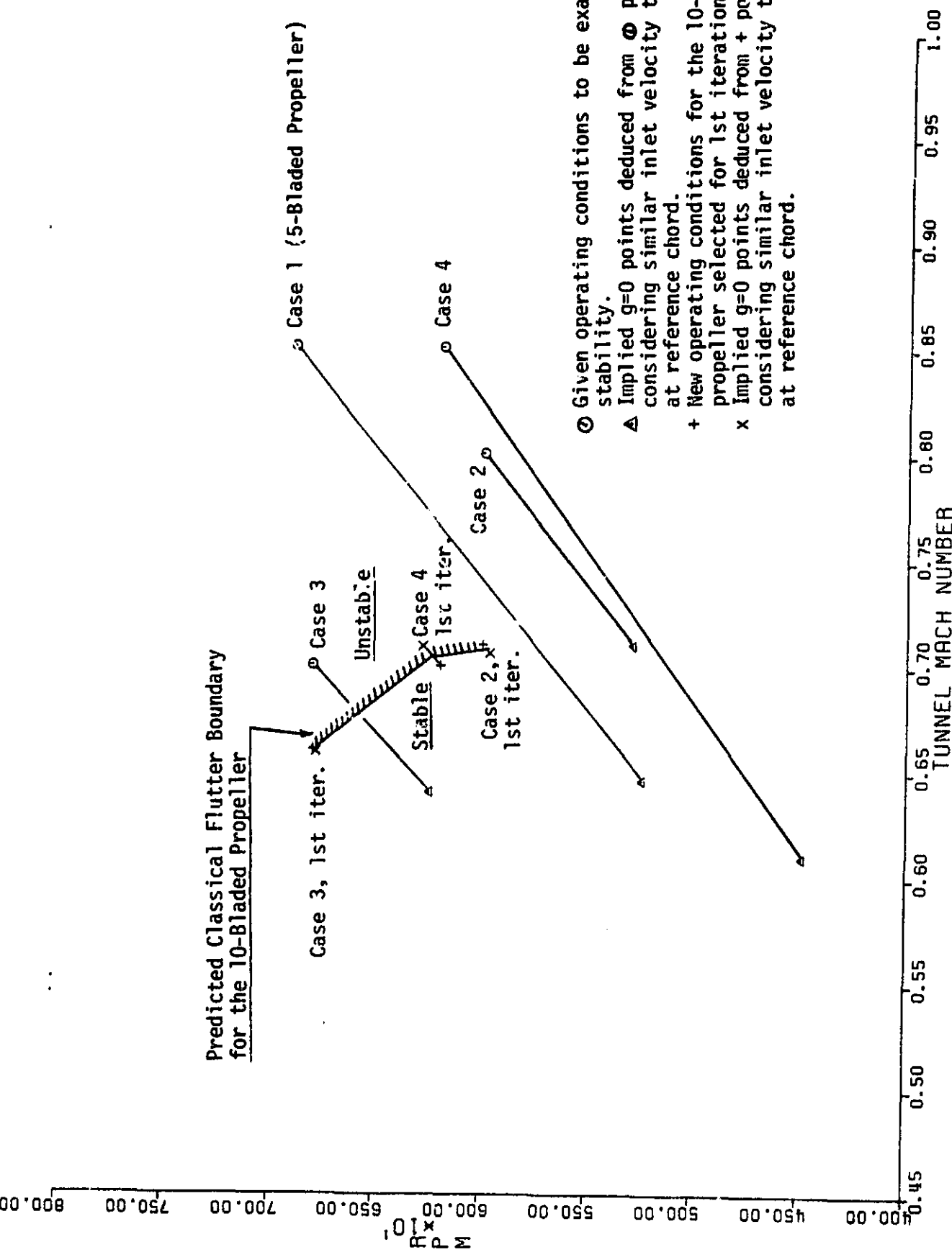
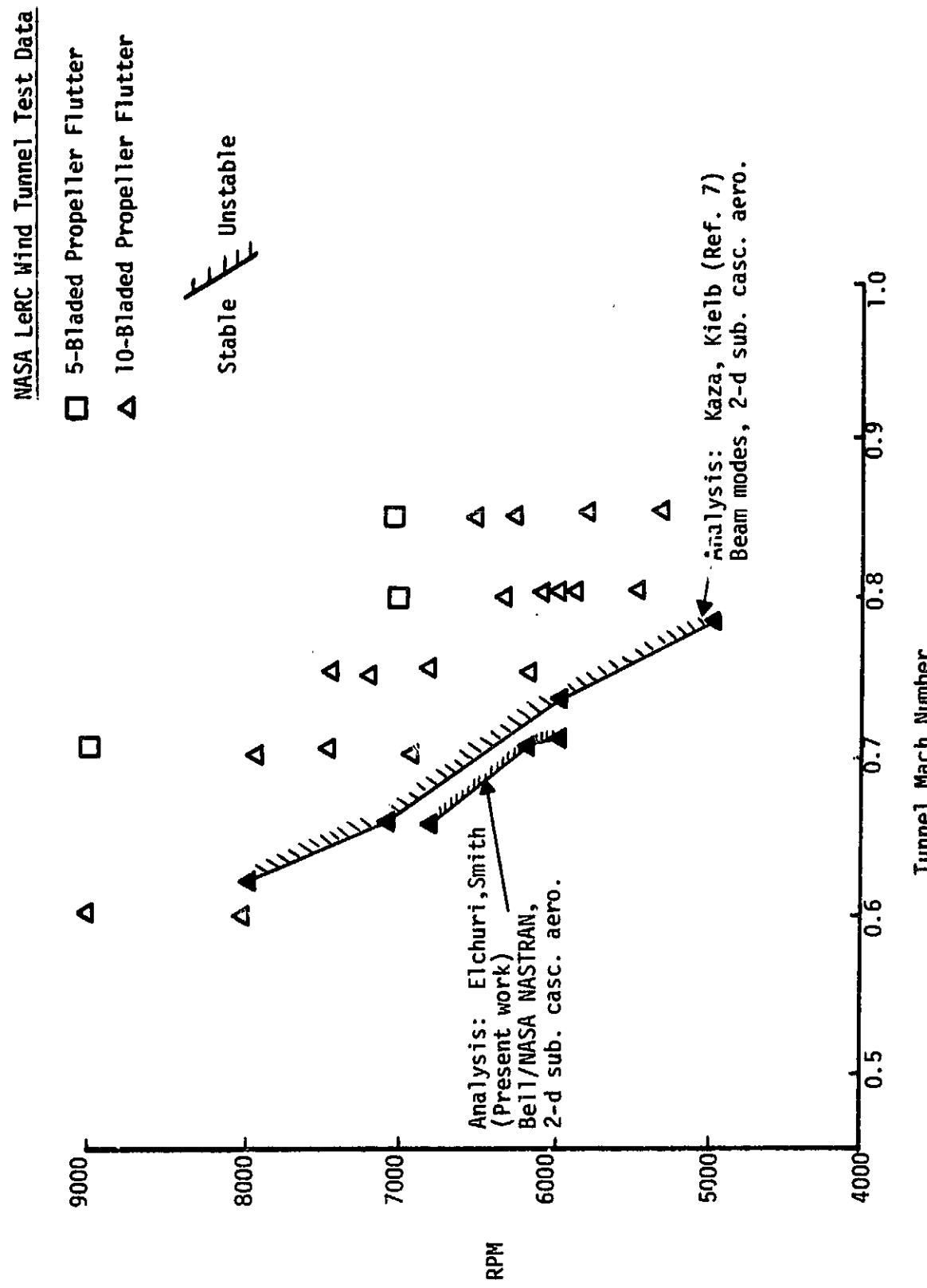


Figure 63. SR-5 CLASSICAL FLUTTER SUMMARY

ORIGINAL PAGE IS
OF POOR QUALITY



5.0 CONCLUSIONS

1. The two-dimensional subsonic cascade unsteady aerodynamics theory of Ref. 1 has been
 - a) modified to account for the variable sweep angles of the blades of the advanced turbopropellers, and
 - b) implemented in NASTRAN Level 17.7 for use in a strip theory manner on blade chords selected normal to a "spanwise" reference curve.
2. The blade has been structurally and aerodynamically modelled using existing and modified NASTRAN finite elements capability.
3. The in-vacuo natural frequencies and mode shapes of the blade, including the differential stiffness effects due to centrifugal loads, have been computed.
4. The two-dimensional strip aerodynamics and the structural modal properties have been formally integrated to determine the generalized aerodynamic coefficients matrix for the blade modes.
5. Modal flutter analyses conducted on two SR-5 five- and ten-bladed propellers have shown good correlation with NASA wind tunnel tests.

6.0 RECOMMENDATIONS

1. This is a new capability in NASTRAN to conduct modal flutter analysis of advanced turbopropellers with variable sweep blades and, although its validity has been clearly demonstrated by the limited number of examples presented, it should be exercised extensively to determine its potential and limits.
2. Development and application of a three-dimensional unsteady compressible aerodynamics theory for multi-bladed propellers, in a manner similar to that of Ref. 8 , is a desirable extension of the present work. This should ameliorate the unknown effects of "acoustic resonances" present in the two-dimensional approach.

APPENDIX A

GENERALIZED OSCILLATORY AERODYNAMIC COEFFICIENTS MATRIX Q FOR THE SWEPT BLADES OF ADVANCED TURBOPROPPELLERS

A.1 GENERAL

The generalized modal aerodynamic force matrix $[Q_{ij}]$ for flutter analysis of the advanced turbopropeller with swept blades is derived. The two-dimensional subsonic cascade unsteady aerodynamics program of Rao and Jones (Ref. 1) has been modified to include the effects of blade sweep. The blade is spanned by a number of non-intersecting chords selected normal to any spanwise reference curve such as the blade leading edge (Figure 64). The modified two-dimensional cascade theory is applied on each of these chords to determine the generalized aerodynamic forces acting on the associated strip. The strip results are added to obtain the blade aerodynamic matrix.

In order to conform to the existing computational scheme, and thus reduce extensive recoding, the chordwise generalized aerodynamic matrices are first computed for predefined, simple, chordwise aerodynamic modes (Figure 65). The chordwise structural modes are then introduced via Fourier expansions to finally obtain the blade generalized airforce matrix.

A.2 DEFINITIONS

Figure 64 illustrates some of the definitions pertinent to incorporating sweep effects in the 2-d cascade program. A_B_-, AB and A_B_+ represent three successive chords with points A's on the leading edge. For the chord AB, at any operating condition \vec{WA} represents the absolute inflow velocity while \vec{AU} ($= \vec{\Omega} \times \vec{RA}$) is the blade (tangential) velocity. WA and AU uniquely define a plane in which the inflow properties are defined.

In the plane WAU, $\vec{VA} = \vec{WA} - \vec{AU}$ represents the relative inflow velocity.

AI is the line of intersection between the axial plane through point A and the plane WAU. Angle IAV defines the relative inflow angle β (shown positive).

ORIGINAL PAGE IS
OF POOR QUALITY

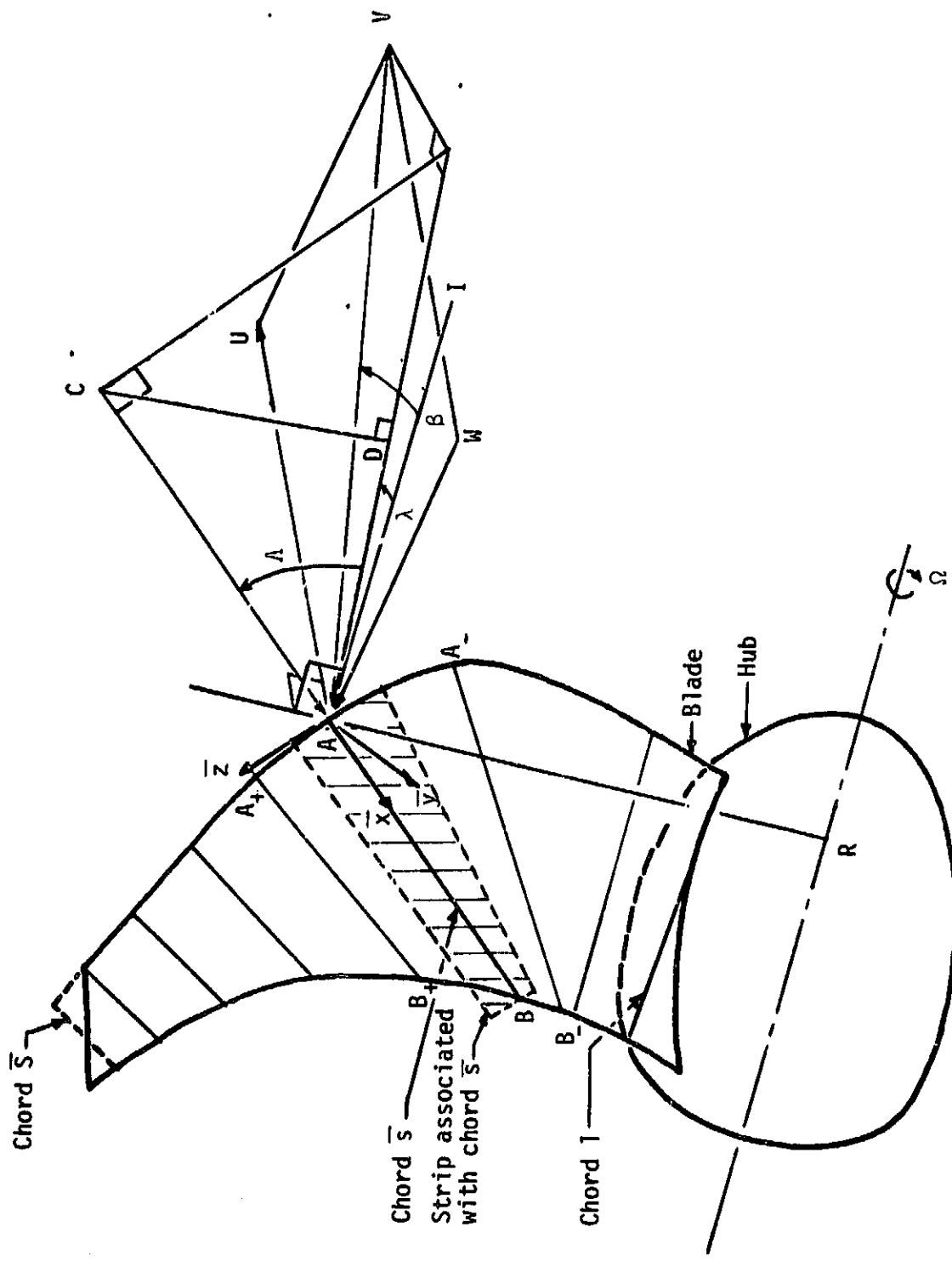


Figure 64. Some Definitions for Swept Blade Aerodynamics

ORIGINAL PAGE IS
OF POOR QUALITY

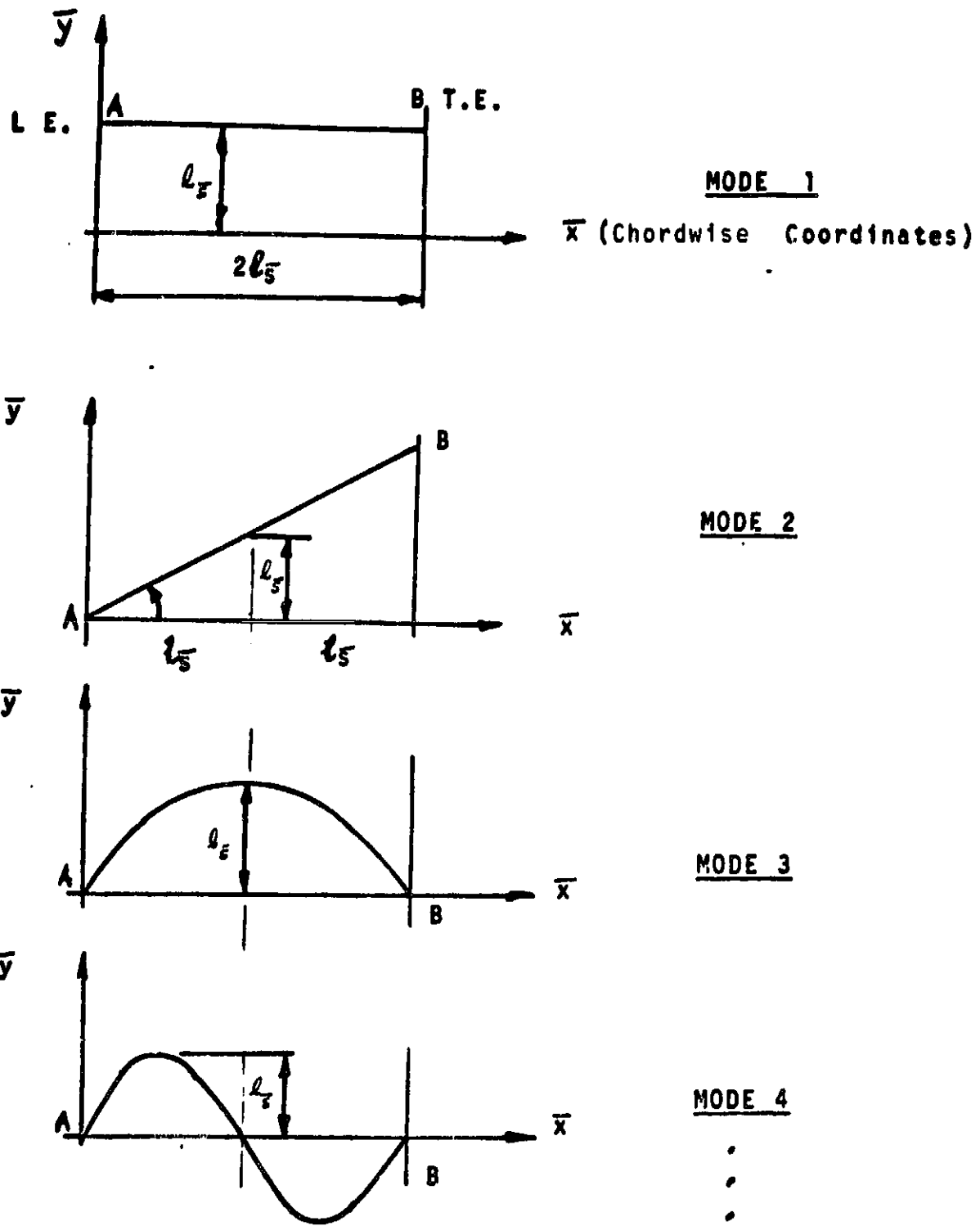


Figure 65. Chordwise Aerodynamic Modes

The angle of sweep Λ is defined as the angle of inclination of the chord BA with the plane WAU. Λ shown in Figure 64 is positive.

AD is the projection of AC (BA extended to C) in the plane WAU. Angle IAD represents the stagger angle λ , and is shown positive.

A local coordinate system $\bar{x}\bar{y}\bar{z}$ is defined at the leading edge point A of the chord AB such that \bar{x} is directed along AB. \bar{y} is defined normal to the 'mean' surface containing the points A_{-} , A, A_{+} , B_{+} , B and B_{-} . The unit vector along \bar{y} , for the sense of Ω shown in Figure 64, is given by

$$\hat{\mathbf{J}} = \frac{1}{2} \left[\frac{(\vec{A}_+ \vec{B}_+) \times (\vec{AB})}{|(\vec{A}_+ \vec{B}_+) \times (\vec{AB})|} + \frac{(\vec{AB}) \times (\vec{A}_+ \vec{B}_-)}{|(\vec{AB}) \times (\vec{A}_+ \vec{B}_-)|} \right] . \quad (A1)$$

Modal translations along \bar{y} and rotations about \bar{x} are used in deriving the generalized airforce matrix (Section A.6). For the opposite sense of rotation, $\bar{x}\bar{y}\bar{z}$ is defined to be left handed with \bar{y} reversing direction.

The shaded area about the chord AB represents the strip of integration associated with AB. The length of the strip is given by AB, the widths at the leading and trailing edges are respectively given by

$$\left. \begin{aligned} w_{l.e.} &= \frac{1}{2} (\vec{A}_- \vec{A}_+) \cdot \hat{\vec{k}} \quad , \text{ and} \\ w_{t.e.} &= \frac{1}{2} (\vec{B}_- \vec{B}_+) \cdot \hat{\vec{k}} \quad , \end{aligned} \right\} \quad (A2)$$

where \hat{k} is the unit vector along \bar{z} .

A.3 BLADE DEGREES OF FREEDOM

For aerodynamic computations, consider the propeller blade to be spanned by S chords with G structural grid points on each chord. The blade degrees of freedom $\{u\}$ can then be partitioned as

$$\{u\} = \begin{Bmatrix} u_1 \\ u_2 \\ \vdots \\ u_s \\ \vdots \\ u_n \end{Bmatrix}, \quad (A3)$$

where

$$\{\bar{u}_{\bar{s}}\} = \begin{Bmatrix} u_{\bar{s}1} \\ u_{\bar{s}2} \\ \vdots \\ u_{\bar{s}g} \\ \vdots \\ u_{\bar{s}G} \end{Bmatrix} . \quad (A4)$$

$u_{\bar{s}g}$ represents the 3 translational and 3 rotational degrees of freedom at grid point g on chord \bar{s} .

A.4 NORMAL DISPLACEMENT, DOWNWASH AND PRESSURE DISTRIBUTION IN TERMS OF CHORDWISE AERODYNAMIC MODES

The normal displacement (along + \bar{y}) at any point \bar{x} on the chord \bar{s} can be expressed in the local (chord) coordinate system as a linear combination of the chordwise aerodynamic modes:

$$u^{\bar{s}n}(\bar{x}, \bar{z}, t) = l_{\bar{s}}(\bar{z}) [\phi^{\bar{s}}(\bar{x})] \{n^{\bar{s}1}(\bar{z})\} e^{i\omega t} , \quad (A5)$$

where $l_{\bar{s}}$ is the semi-chord,

$$[\phi^{\bar{s}}] = [1 \ \frac{\bar{x}}{l_{\bar{s}}} \ \sin(\frac{3-2\pi\bar{x}}{2l_{\bar{s}}}) \dots \sin(\frac{g-2\pi\bar{x}}{2l_{\bar{s}}}) \dots \sin(\frac{G-2\pi\bar{x}}{2l_{\bar{s}}})] \quad (A6)$$

represents the chordwise aerodynamic mode shapes, and

$$\{n^{\bar{s}1}\} = \begin{Bmatrix} a_1 \\ a_2 \\ \vdots \\ a_g \\ \vdots \\ a_G \end{Bmatrix} \quad (A7)$$

is the aerodynamic modal participation vector.

The downwash at \bar{x} can be written as

$$w^{\bar{s}n}(\bar{x}, \bar{z}, t) \approx [\frac{\partial}{\partial t} + V_{\bar{s}} (\frac{\partial}{\partial \bar{x}} + \tan \Lambda \frac{\partial}{\partial \bar{z}})] u^{\bar{s}n}(\bar{x}, \bar{z}, t) , \quad (A8)$$

where the chordwise cascade relative inflow velocity from Figure 64 is

$$V_{\bar{s}} = [(VA) \cos (\beta - \lambda)] \cos \Lambda = V \cos \Lambda . \quad (A9)$$

The quantity within the brackets represents the streamwise cascade relative inflow velocity.

Substituting for $u^{\bar{s}n}$ from equation (A5), the downwash can be written as

$$\begin{aligned} w^{\bar{s}n}(\bar{x}, \bar{z}, t) = & V_{\bar{s}} \left[L \left(ik + \left(\frac{\partial \bar{e}_{\bar{s}}}{\partial \bar{z}} \right) \tan \Lambda \right) L \phi^{\bar{s}} \right] \oplus L \frac{\partial \phi^{\bar{s}}}{\partial \left(\frac{\bar{x}}{\bar{e}_{\bar{s}}} \right)} \left[\{n^{\bar{s}1}\} \right. \\ & \left. \oplus \tan \Lambda L \phi^{\bar{s}} \left[\{n^{\bar{s}2}\} \right] e^{iwt} \right] , \end{aligned} \quad (A10)$$

where

$$\{n^{\bar{s}2}\} = \left\{ \frac{\partial \{n^{\bar{s}1}\}}{\partial \left(\frac{\bar{z}}{\bar{e}_{\bar{s}}} \right)} \right\} , \quad (A11)$$

and the reduced frequency

$$k = \omega \bar{e}_{\bar{s}} / V_{\bar{s}} = \omega l \cos \Lambda / (V \cos \Lambda) = \omega l / V . \quad (12)$$

Corresponding to the downwash boundary conditions associated with each of the elements of the modal participation vector $\{n^{\bar{s}1}\}$ and its derivative $\{n^{\bar{s}2}\}$, the modified 2-d subsonic cascade unsteady aerodynamics program computes the differential pressure at P discrete points distributed along the chord \bar{s} . (The contribution due to the variation of the perturbation velocity potential in the \bar{z} direction is neglected.) The physical differential pressure at these P points can then be found from

$$\{p^{\bar{s}}\} = \{p^{\bar{s}}(\bar{y}_-)\} - \{p^{\bar{s}}(\bar{y}_+)\} = \frac{1}{2} \rho_{\bar{s}} V_{\bar{s}}^{-2} \left([\psi_{pg}^{\bar{s}1}] \{n^{\bar{s}1}\} + [\psi_{pg}^{\bar{s}2}] \{n^{\bar{s}2}\} \right) e^{iwt} . \quad (A13)$$

In order to properly account for the leading edge singularity in subsonic flow while integrating the pressures along the chord, the modal differential pressures are rewritten as

$$\begin{aligned} [\psi_{pg}^{\bar{s}1}] &= [\pi_{pp}] [c_{gp}^1]^T, \text{ and} \\ [\psi_{pg}^{\bar{s}2}] &= [\pi_{pp}] [c_{gp}^2]^T, \end{aligned} \quad \left. \right\} \quad (A14)$$

where

$$[\pi_{pp}] = \begin{bmatrix} \sqrt{\frac{2\ell_{\bar{s}} - \bar{x}_1}{\bar{x}_1}} & \sin(\frac{2-1 \cdot \pi \cdot \bar{x}_1}{2\ell_{\bar{s}}}) \dots \sin(\frac{P-1 \cdot \pi \cdot \bar{x}_1}{2\ell_{\bar{s}}}) \\ \sqrt{\frac{2\ell_{\bar{s}} - \bar{x}_2}{\bar{x}_2}} & \sin(\frac{2-1 \cdot \pi \cdot \bar{x}_2}{2\ell_{\bar{s}}}) \dots \sin(\frac{P-1 \cdot \pi \cdot \bar{x}_2}{2\ell_{\bar{s}}}) \\ \vdots & \vdots \\ \vdots & \vdots \\ \sqrt{\frac{2\ell_{\bar{s}} - \bar{x}_P}{\bar{x}_P}} & \sin(\frac{2-1 \cdot \pi \cdot \bar{x}_P}{2\ell_{\bar{s}}}) \dots \sin(\frac{P-1 \cdot \pi \cdot \bar{x}_P}{2\ell_{\bar{s}}}) \end{bmatrix} \quad (A15)$$

A.5 GENERALIZED AIRFORCE MATRICES FOR CHORDWISE AERODYNAMIC MODES

The differential pressures are estimated at P points along the chord (equation A13). The physical displacement at these P points can be written using equation A5 as

$$\{u^{\bar{s}n}\} = \ell_{\bar{s}} [\phi_{pg}^{\bar{s}}] \{\eta^{\bar{s}1}\} \quad (A16)$$

The virtual work done by the aerodynamic forces, acting on the blade strip associated with the chord \bar{s} , through a virtual displacement $\delta\{u^{\bar{s}n}\}$ becomes

$$\delta W^{\bar{s}} = \int_{\bar{x}=0}^{2\ell_{\bar{s}}} \delta u^{\bar{s}n} \cdot p^{\bar{s}} \cdot (C^{\bar{s}1} \bar{x} + C^{\bar{s}2}) \cdot d\bar{x} \quad (A17)$$

$$\text{i.e. } \delta W^3 = \frac{1}{2} \rho_{\bar{s}} V_{\bar{s}}^2 l_{\bar{s}}^{-3} \delta L \eta^{\bar{s}1} J [\phi_{pg}^{\bar{s}1}]^T [W] [\pi_{pp}] ([C_{gp}^1]^T \{\eta^{\bar{s}1}\} + [C_{gp}^2]^T \{\eta^{\bar{s}2}\}) , \quad (\text{A18})$$

where

$$[W] = \begin{bmatrix} [C^{\bar{s}1}(\frac{\bar{x}_1}{l_{\bar{s}}}) + \frac{C^{\bar{s}2}}{l_{\bar{s}}}][\Delta(\frac{\bar{x}_1}{l_{\bar{s}}})] \\ [C^{\bar{s}1}(\frac{\bar{x}_2}{l_{\bar{s}}}) + \frac{C^{\bar{s}2}}{l_{\bar{s}}}][\Delta(\frac{\bar{x}_2}{l_{\bar{s}}})] \\ \vdots \\ [C^{\bar{s}1}(\frac{\bar{x}_p}{l_{\bar{s}}}) + \frac{C^{\bar{s}2}}{l_{\bar{s}}}][\Delta(\frac{\bar{x}_p}{l_{\bar{s}}})] \end{bmatrix} \quad (\text{A19})$$

$$= C^{\bar{s}1} [W^2] + \frac{C^{\bar{s}2}}{l_{\bar{s}}} [W^1] . \quad (\text{A20})$$

Substituting for $[W]$ in equation (A18),

$$\delta W^{\bar{s}} = \frac{1}{2} \rho_{\bar{s}} V_{\bar{s}}^2 l_{\bar{s}}^{-3} \delta L \eta^{\bar{s}1} J ([A_{gg}^{\bar{s}1}] \{\eta^{\bar{s}1}\} + [A_{gg}^{\bar{s}2}] \{\eta^{\bar{s}2}\}) , \quad (\text{A21})$$

whereby the generalized chordwise aerodynamic force matrices are

$$\left. \begin{aligned} [A_{gg}^{\bar{s}1}] &= [I_{gp}^{\bar{s}}] [C_{gp}^1]^T, \text{ and} \\ [A_{gg}^{\bar{s}2}] &= [I_{gp}^{\bar{s}}] [C_{gp}^2]^T, \end{aligned} \right\} \quad (\text{A22})$$

$$\left. \begin{aligned} [I_{gp}^{\bar{s}}] &= C^{\bar{s}1} [I_{gp}^2] + \frac{C^{\bar{s}2}}{l_{\bar{s}}} [I_{gp}^1], \\ [I_{gp}^2] &= [\phi_{pg}^{\bar{s}}]^T [W^2] [\pi_{pp}], \text{ and} \\ [I_{gp}^1] &= [\phi_{pg}^{\bar{s}}]^T [W^1] [\pi_{pp}]. \end{aligned} \right\} \quad (\text{A23})$$

Elements of matrices I_{gp}^2 and I_{gp}^1 have been evaluated as chordwise integrals, and are presented in Appendix B.

A.6 TRANSFORMATION BETWEEN AERODYNAMIC AND STRUCTURAL MODAL COORDINATES

Equation (A5) can be used to express the normal displacement at the G structural grid points on chord \bar{s} as

$$\{u^{\bar{s}n}\} = \frac{1}{\bar{s}} [\phi_{gg}^{\bar{s}}] \{\eta^{\bar{s}1}\} . \quad (A24)$$

In terms of structural modal coordinates, $u^{\bar{s}n}$ can also be written as

$$\{u^{\bar{s}n}\} = [\phi_{gi}^{\bar{s}n, \text{local}}] \{\xi_i\} . \quad (A25)$$

Comparison of equation (A24) with equation (A25) yields

$$\{\eta^{\bar{s}1}\} = \frac{1}{\bar{s}} [\phi_{gg}^{\bar{s}}]^{-1} [\phi_{gi}^{\bar{s}n, \text{local}}] \{\xi_i\} . \quad (A26)$$

$$= \frac{1}{\bar{s}} [G_{gi}^{\bar{s}1}] \{\xi_i\} . \quad (A27)$$

Differentiation with respect to \bar{z}/\bar{s} results in

$$\left\{ \frac{\partial \eta^{\bar{s}1}}{\partial (\bar{z}/\bar{s})} \right\} = \{\eta^{\bar{s}2}\} = \left[-\frac{1}{\bar{s}} \cdot \frac{\partial \bar{s}}{\partial \bar{z}} [G_{gi}^{\bar{s}1}] + [G_{gi}^{\bar{s}2}] \right] \{\xi_i\} , \quad (A28)$$

where

$$[G_{gi}^{\bar{s}2}] = [\phi_{gg}^{\bar{s}}]^{-1} \left[\frac{\partial}{\partial \bar{z}} \phi_{gi}^{\bar{s}n, \text{local}} \right] . \quad (A29)$$

The modal displacement matrix $\phi^{\bar{s}n, \text{local}}$ and its derivative $\frac{\partial}{\partial \bar{z}} \phi^{\bar{s}n, \text{local}}$ are derived from the global modal matrix ϕ as follows:

$$[\phi_{gi}^{\bar{s}n, \text{local}}] = [G_{gg}^{\bar{s}n}] [\phi_{g'i}^{\bar{s}1, \text{global}}] , \quad (A30)$$

where each of the i modal columns of $\phi^{\bar{s}1, \text{global}}$ consists of the three modal translations at each of the G computing station grid points on the chord \bar{s} .

The transformation $G^{\bar{s}n1}$ is given by

ORIGINAL PAGE IS
OF POOR QUALITY

$$[G_{gg}^{\bar{s}n}] = \begin{bmatrix} 0 & 1 & 0 \\ 0 & 1 & 0 \\ \vdots & & \\ 0 & 1 & 0 \end{bmatrix} \left[[T_{\bar{s}}^{bl}] \mid [T_{\bar{s}}^{bl}] \mid \dots \mid [T_{\bar{s}}^{bl}] \right] \left[\begin{array}{c} [T_{\bar{s}1}^{bg}]^T \\ [T_{\bar{s}2}^{bg}]^T \\ \vdots \\ [T_{\bar{s}G}^{bg}]^T \\ \vdots \\ [T_{\bar{s}G}^{bg}]^T \end{array} \right], \quad (A31)$$

where T^{bl} and T^{bg} represent the coordinate transformations from the NASTRAN basic system to the local (chord) $\bar{x}\bar{y}\bar{z}$ system and the global (displacement) system, respectively.

Similarly,

$$\left[\frac{\partial}{\partial \bar{z}} \phi_{gi}^{\bar{s}n, \text{local}} \right] = [G_{gg}^{\bar{s}n}] [\phi_{gi}^{\bar{s}2, \text{global}}], \quad (A32)$$

where each of the i modal columns of $\phi^{\bar{s}2, \text{global}}$ consists of the three modal rotations at each of the G computing station grid points on the chord \bar{s} .

The transformation $G_{gg}^{\bar{s}n2}$ is given by

$$[G_{gg}^{\bar{s}n2}] = -m_1 \begin{bmatrix} 1 & 0 & 0 \\ 1 & 0 & 0 \\ \vdots & & \\ 1 & 0 & 0 \end{bmatrix} \left[[T_{\bar{s}}^{bl}] \mid [T_{\bar{s}}^{bl}] \mid \dots \mid [T_{\bar{s}}^{bl}] \right] \left[\begin{array}{c} [T_{\bar{s}1}^{bg}]^T \\ [T_{\bar{s}2}^{bg}]^T \\ \vdots \\ [T_{\bar{s}G}^{bg}]^T \\ \vdots \\ [T_{\bar{s}G}^{bg}]^T \end{array} \right], \quad (A33)$$

where $m_1 = 1$ for right handed $\bar{x}\bar{y}\bar{z}$, and
 $= -1$ for left handed $\bar{x}\bar{y}\bar{z}$.

A.7 GENERALIZED AIRFORCE MATRICES FOR CHORDWISE STRUCTURAL MODES

Introducing relations (A27) and (A28) in equation (A21), the virtual work expression for chord \bar{s} becomes

$$\delta W^{\bar{s}} = \frac{1}{2} \rho_{\bar{s}} V_{\bar{s}}^{-2} l_{\bar{s}}^{-2} \delta L \xi_i \left[[G_{gi}^{\bar{s}1}]^T \left(\frac{1}{l_{\bar{s}}} [A_{gg}^{\bar{s}1}] [G_{gi}^{\bar{s}1}] \right. \right. \\ \left. \left. + [A_{gg}^{\bar{s}2}] \left(-\frac{1}{l_{\bar{s}}} \cdot \frac{\partial l_{\bar{s}}}{\partial z} [G_{gi}^{\bar{s}1}] + [G_{gi}^{\bar{s}2}] \right) \right) \right] \{ \xi_i \}, \quad (A35)$$

whereby the generalized airforce matrices for chordwise structural modes can be obtained as

$$\begin{aligned} [Q_{ii}^{\bar{s}1}] &= \frac{1}{2} \rho_{\bar{s}} V_{\bar{s}}^2 \ell_{\bar{s}}^2 \frac{1}{\ell_{\bar{s}}} [G_{g1}^{\bar{s}1}]^T [A_{gg}^{\bar{s}1}] [G_{g1}^{\bar{s}1}] = \frac{1}{2} \rho_{\bar{s}} V_{\bar{s}}^2 \ell_{\bar{s}}^2 [Q_{ii}^{\bar{s}1}], \text{ and} \\ [Q_{ii}^{\bar{s}2}] &= \frac{1}{2} \rho_{\bar{s}} V_{\bar{s}}^2 \ell_{\bar{s}}^2 [G_{g1}^{\bar{s}1}]^T [A_{gg}^{\bar{s}2}] \left(-\frac{1}{\ell_{\bar{s}}} \cdot \frac{\partial \ell_{\bar{s}}}{\partial \bar{z}} \cdot [G_{g1}^{\bar{s}1}] + [G_{g1}^{\bar{s}2}] \right) \\ &= \frac{1}{2} \rho_{\bar{s}} V_{\bar{s}}^2 \ell_{\bar{s}}^2 [\bar{Q}_{ii}^{\bar{s}2}] \end{aligned} \quad (A36)$$

Combining $Q_{ii}^{\bar{s}1}$ and $Q_{ii}^{\bar{s}2}$, the generalized airforce matrix for chord \bar{s} is defined as

$$\begin{aligned} [Q_{ii}^{\bar{s}}] &= \frac{1}{2} \rho_{\bar{s}, \text{ref}} V_{\bar{s}, \text{ref}}^2 \left(\frac{1}{2} \frac{\rho_{\bar{s}} V_{\bar{s}}^2 \ell_{\bar{s}}^2}{\frac{1}{2} \rho_{\bar{s}, \text{ref}} V_{\bar{s}, \text{ref}}^2} \right) ([Q_{ii}^{\bar{s}1}] + [\bar{Q}_{ii}^{\bar{s}2}]) , \\ &= \frac{1}{2} \rho_{\bar{s}, \text{ref}} V_{\bar{s}, \text{ref}}^2 [\bar{Q}_{ii}^{\bar{s}}] \end{aligned} \quad \left. \right\} \quad (A37)$$

A.8 BLADE GENERALIZED AIRFORCE MATRIX

The virtual work done by the aerodynamic forces on the blade is the sum total of the virtual work done by all the chordwise aerodynamic forces on their respective strips. Thus

$$\begin{aligned} \delta W^{\text{blade}} &= \sum_{\bar{s}=1}^{\bar{S}} \delta W^{\bar{s}} \\ &= \frac{1}{2} \rho_{\bar{s}, \text{ref}} V_{\bar{s}, \text{ref}}^2 \sum_{\bar{s}} \delta L \xi_{ij} [\bar{Q}_{ij}^{\bar{s}}] \{ \xi_j \} , \end{aligned} \quad (A38)$$

whereby the generalized airforce matrix for the swept blade of the advanced turbo-propeller can be written as

$$[Q_{ii}^{\text{blade}}] = \frac{1}{2} \rho_{\bar{s}, \text{ref}} V_{\bar{s}, \text{ref}}^2 \sum_{\bar{s}=1}^{\bar{S}} [\bar{Q}_{ii}^{\bar{s}}] = \frac{1}{2} \rho_{\bar{s}, \text{ref}} V_{\bar{s}, \text{ref}}^2 [\bar{Q}_{ii}^{\bar{s}}] . \quad (A39)$$

APPENDIX B

CHORDWISE WEIGHTING MATRICES

The chordwise weighting matrices \hat{I}_{gp} and I_{gp}^1 appearing in equations (A23) of Appendix A are evaluated.

$$1. [I_{gp}^2] = [\phi_{pg}^s]^T [W^2] [\pi_{pp}]$$

$$= \begin{bmatrix} I_{x\sqrt{-}} & I_{x,1} & I_{x,2} & \dots & I_{x,(P-1)} \\ I_{x^2\sqrt{-}} & I_{x^2,1} & I_{x^2,2} & \dots & I_{x^2,(P-1)} \\ I_{x,1,\sqrt{-}} & I_{x,1,1} & I_{x,1,2} & \dots & I_{x,1,(P-1)} \\ I_{x,2,\sqrt{-}} & I_{x,2,1} & I_{x,2,2} & \dots & I_{x,2,(P-1)} \\ \vdots & \vdots & \vdots & \ddots & \vdots \\ \vdots & \vdots & \vdots & \ddots & \vdots \\ I_{x,(G-2),\sqrt{-}} & I_{x,(G-2),1} & I_{x,(G-2),2} & \dots & I_{x,(G-2),(P-1)} \end{bmatrix} .$$

The six typical elements of I_{gp}^2 are as follows:

$$a) I_{x\sqrt{-}} = \int_0^2 \left(\frac{\bar{x}}{\bar{l}_s} \right) \sqrt{\frac{2-(\bar{x}/\bar{l}_s)}{(\bar{x}/\bar{l}_s)}} d\left(\frac{\bar{x}}{\bar{l}_s} \right)$$

$$= \pi/2 .$$

$$b) I_{x,r} = \int_0^2 \left(\frac{\bar{x}}{\bar{l}_s} \right) \sin \left(\frac{r\pi\bar{x}}{2\bar{l}_s} \right) d\left(\frac{\bar{x}}{\bar{l}_s} \right), \quad r = 1, 2, \dots, (P-1) .$$

$$= \frac{4}{r\pi} (-1)^{r+1} .$$

$$c) I_{x^2\sqrt{-}} = \int_0^2 \left(\frac{\bar{x}}{\bar{l}_s} \right)^2 \sqrt{\frac{2-(\bar{x}/\bar{l}_s)}{(\bar{x}/\bar{l}_s)}} d\left(\frac{\bar{x}}{\bar{l}_s} \right)$$

$$= \pi/2 .$$

$$\begin{aligned}
 d) \quad I_{x^2,r} &= \int_0^2 \left(\frac{\dot{x}}{\dot{l}_s}\right)^2 \sin\left(\frac{r\pi\dot{x}}{2\dot{l}_s}\right) d\left(\frac{\dot{x}}{\dot{l}_s}\right), \quad r=1, 2, \dots, (P-1). \\
 &= -\frac{8}{r\pi}, \quad r \text{ even, and} \\
 &= \frac{8}{r\pi} - \frac{32}{(r\pi)^3}, \quad r \text{ odd}.
 \end{aligned}$$

$$e) \quad I_{x,r,\sqrt{r}} = \int_0^2 \left(\frac{\dot{x}}{\dot{l}_s}\right) \cdot \sin\left(\frac{r\pi\dot{x}}{2\dot{l}_s}\right) \cdot \sqrt{\frac{2-(\dot{x}/\dot{l}_s)}{(\dot{x}/\dot{l}_s)}} d\left(\frac{\dot{x}}{\dot{l}_s}\right), \quad r=1, 2, \dots, (G-2).$$

This integral is evaluated numerically, and the values are tabulated as follows:

r	$I_{x,r,\sqrt{r}}$
1	1.1333
2	-0.00036
3	0.18796
4	-0.00027
5	0.08469
6	-0.00022
7	0.05049
8	-0.00019

$$\begin{aligned}
 f) \quad I_{x,r,s} &= \int_0^2 \left(\frac{\dot{x}}{\dot{l}_s}\right) \cdot \sin\left(\frac{r\pi\dot{x}}{2\dot{l}_s}\right) \cdot \sin\left(\frac{s\pi\dot{x}}{2\dot{l}_s}\right) d\left(\frac{\dot{x}}{\dot{l}_s}\right), \\
 &\quad r = 1, 2, \dots, \overline{G-2}, \\
 &\quad s = 1, 2, \dots, \overline{P-1}. \\
 &= 1, \quad r=s \\
 &= 0, \quad r \neq s, \quad (r+s) \text{ even,} \\
 &= -\frac{16 r \cdot s}{\pi^2 (r-s)^2 (r+s)^2}, \quad r \neq s, \quad (r+s) \text{ odd.}
 \end{aligned}$$

$$2. [I_{gp}^1] = [\phi_{pg}^s]^T [W^1] [\pi_{pp}]$$

$$= \begin{bmatrix} I_{\sqrt{}} & I_1. & I_2. & \dots & I_{(P-1)} \\ I_{x\sqrt{}} & I_{x.1} & I_{x.2} & \dots & I_{x.(P-1)} \\ I_{1.\sqrt{}} & I_{1.1} & I_{1.2} & \dots & I_{1.(P-1)} \\ I_{2.\sqrt{}} & I_{2.1} & I_{2.2} & \dots & I_{2.(P-1)} \\ \vdots & \vdots & \vdots & & \vdots \\ \vdots & \vdots & \vdots & & \vdots \\ I_{(G-2)\sqrt{}} & I_{(G-2).1} & I_{(G-2).2} & \dots & I_{(G-2).(P-1)} \end{bmatrix}.$$

The six typical elements of I_{gp}^1 are as follows:

$$a) I_{\sqrt{}} = \int_0^2 \frac{\sqrt{2-(\bar{x}/\ell_s)}}{\sqrt{(\bar{x}/\ell_s)}} d\left(\frac{\bar{x}}{\ell_s}\right)$$

$$= \pi.$$

$$b) I_r = \int_0^2 \sin\left(\frac{r\pi\bar{x}}{2\ell_s}\right) d\left(\frac{\bar{x}}{\ell_s}\right), \quad r = 1, 2, \dots, P-1.$$

$$= \frac{2}{\pi r} [1 - (-1)^r].$$

c) $I_{x\sqrt{}}$ as given by typical element (a) of I_{gp}^2 .

d) $I_{x.r}$ as given by typical element (b) of I_{gp}^2 .

$$e) I_{r\sqrt{}} = \int_0^2 \sin\left(\frac{r\pi\bar{x}}{2\ell_s}\right) \sqrt{\frac{2-(\bar{x}/\ell_s)}{(\bar{x}/\ell_s)}} d\left(\frac{\bar{x}}{\ell_s}\right), \quad r = 1, 2, \dots, G-2.$$

This integral is evaluated numerically, and the values are tabulated as follows:

ORIGINAL PAGE IS
OF POOR QUALITY

r	$I_{r,s}$
1	1.48283
2	0.89414
3	0.83521
4	0.66721
5	0.64172
6	0.55519
7	0.54026
8	0.48547

$$f) \quad I_{r,s} = \int_0^2 \sin\left(\frac{r\pi\bar{x}}{2\ell_s}\right) \cdot \sin\left(\frac{s\pi\bar{x}}{2\ell_s}\right) d\left(\frac{\bar{x}}{\ell_s}\right)$$

$$r = 1, 2, \dots, \overline{G-2},$$

$$s = 1, 2, \dots, \overline{P-1}.$$

$$= 1, r=s$$

$$= 0, r \neq s .$$

SYMBOLS

A	Chordwise aerodynamic matrix for aerodynamic modes
B	Blade spacing
C	Matrix of modal pressure coefficients, constants
c	Chord
f	Frequency ($\omega/2\pi$)
G	Transformation matrix
g	Artificial structural damping
I	Chordwise weighting matrix
t	$\sqrt{-T}$
K	Stiffness matrix
k	Reduced frequency
l	Semic chord
M	Mass matrix, cascade relative inflow Mach number
m ₁	Constant
N	Number of blades on propeller
P	Load vector
p	Pressure, complex eigenvalue
Q	Aerodynamic coefficient matrix for structural modes
T	Transformation matrix
t	Time
u	Physical degrees of freedom
V	Cascade relative inflow velocity
W	Virtual work, weighting matrix
w	Strip width, downwash velocity
$\bar{x}, \bar{y}, \bar{z}$	Chord local coordinate system
β	Relative inflow angle

SYMBOLS (Continued)

- n Aerodynamic modal coordinates
- Λ Sweep angle
- λ Stagger angle
- μ Non-dimensional damping ($gv/2$)
- ν Non-dimensional frequency (f/f_{vacuum})
- ξ Structural modal coordinates
- ρ Mass (flow) density
- σ Interblade phase angle
- ϕ Chordwise aerodynamic modes
- ϕ Structural modes
- ψ Differential pressure distribution in aerodynamic modes
- Ω Rotational speed
- ω Circular frequency

SUBSCRIPTS

- g Grid point on chord, chordwise aerodynamic mode
- i Structural mode
- l.e. Leading edge
- p Cascade theory pressure point
- ref. Reference
- \bar{s} Chord \bar{s}
- t.e. Trailing edge

SYMBOLS (Continued)

SUPERSCRIPTS

b Basic coordinate system

cf Centrifugal

d Differential

e Elastic

g Global coordinate system
global

l Local coordinate system
local

n Normal to chord

s Chord s

REFERENCES

1. Rao, B. M., and Jones, W. P., "Unsteady Airloads for a Cascade of Staggered Blades in Subsonic Flow," 46th Propulsion Energetics Review Meeting, Monterey, California, September 1975.
2. Barmby, J. G., Cunningham, H. J., and Garrick, I. E., "Study of Effects of Sweep on the Flutter of Cantilever Wings," NACA Report No. 1014, 1951.
3. NASTRAN Level 17.6 Theoretical Manual, NASA SP 221 (05), October 1980.
4. Jones, W. P., and Moore, J. A., "Aerodynamic Theory for a Cascade of Oscillating Airfoils in Compressible Subsonic Flow," Report No. TEES-3068-75-01, Texas A&M University, February 1975.
5. Kielb, R. E., and Kaza, K. R. V., "Aeroelastic Characteristics of a Cascade of Mistuned Blades in Subsonic and Supersonic Flows," NASA TM 82631, September 1981.
6. Elchuri, V., Gallo, A. M., and Skalski, S. C., "NASTRAN Documentation for Flutter Analysis of Advanced Turbopropellers," NASA CR-167927 , April 1982.
7. Kaza, K. R. V., and Kielb, R. E. - Personal communications.
8. Elchuri, V., "Prediction of Unsteady Loads and Moments on Ship Propellers," Ph.D. Dissertation, Texas A&M University, August 1977.